THE FORCE REGULATION ON BINDING KINETICS AND CONFORMATIONS OF INTEGRIN AND SELECTINS USING A BIO-MEMBRANE FORCE PROBE

A Thesis
Presented to
The Academic Faculty

By

Wei Chen

In Partial Fulfillment
of the Requirements for the Degree
Doctor of Philosophy in Bioengineering in the
School of Mechanical Engineering

Georgia Institute of Technology
May 2009

THE FORCE REGULATION ON BINDING KINETICS AND CONFORMATIONS OF INTEGRIN AND SELECTINS USING A BIO-MEMBRANE FORCE PROBE

Approved by:

Dr. Cheng Zhu, Advisor
School of Biomedical Engineering
Georgia Institute of Technology

Dr. Levent F. Degertekin
School of Mechanical Engineering
Georgia Institute of Technology

Dr. Evan A. Evans
Departments of Physics and Pathology,
University of British Columbia

Dr. Nael McCarty
School of Biology
Georgia Institute of Technology

Dr. Andres J. Garcia
School of Mechanical Engineering
Georgia Institute of Technology

Date Approved: April 1st, 2009

I dedicate this thesis

to

My parents

I am forever indebted to my parents, 陈子辰 (Zichen Chen) and 李素华 (Suhua Li). I would not have been able to finish my Ph.D. thesis without their priceless love, endless patience and unconditional supports.

My wife

I am so grateful to my wife, 尹巍巍 (**Weiwei Yin)**, who was always there to support me unconditionally, comfort and encourage me to go through difficult times.

ACKNOWLEDGEMENTS

I would like to express my gratitude to many people who supported me in the passed 5 years. Without their helps, I could not believe I could finish my Ph.D. research smoothly.

Firstly, I would like to thank my Ph.D. thesis advisor, Dr. Cheng Zhu. He is the most important person to my Ph.D. study and research. I would like to thank him for providing me a precious chance to enter this exciting bioengineering field five years ago, and for his continuous financial support, helpful guide, and encouragement through my whole Ph.D. period. More importantly, I would thank him for teaching me how to do science, for his enthusiasm and curiosity to science which lead me to explore this mysterious scientific world, for his strictness to the scientific research which taught me to patiently carry out and repeat tedious scientific experiments, carefully examine discoveries and thoughtfully formalize our interpretation and conclusions.

Secondly, I would like to thank Dr. Evan Evans. As old saying says, “Standing on the Shoulder of Giants.” Dr.Evans is a talented giant, and I’m a dwarf standing on his shoulder. His creative invention, the BFP, is my major powerful tool for my Ph.D. research. His unconditional technical support helped me so much to quickly build up a new BFP in Dr.Zhu’s lab and smoothly finish my thesis works. His thoughts of the essence of scientific research benefit my Ph.D. study and my whole lifetime in future. His enthusiasm on science makes me realize that doing science is full of fun.

In addition to Dr.Evan Evans, I would like to thank his lab members, Andrew Leung and Dr. Koji Kinoshita. They are giant’s two arms. They gave me tremendous helps on teaching me, building up the BFP and overcoming difficulties in BFP experiments.

I would like to thank my other thesis committee members, Dr.Andres Garcia, Dr.Levent Degertegin and Dr. Nael McCarty for serving as my thesis committee and for taking time to make valuable suggestions on my thesis work. I would also like to thank

Dr. Garcia for his encouragement since my Ph.D. qualify examination and strong support on my whole Ph.D. thesis research, Dr. Degertegin for his creativity that impacted my research, and Dr. McCarty for introducing and leading me into the biological world.

I would like to thank Dr. Rodger McEver for kindly proving me many important reagents for my Ph.D. research, for guiding me on how to carry out cutting-edge scientific research and for greatly supporting my on academic career development. I also would like to thank his members as well for supporting my research.

I would like to thanks technical supporting staff in the Institute of Bioscience and Bioengineering and the Mechanical Engineering (ME) at Georgia Tech. I would like to thank Mr.John Gramham and his co-op students in ME's machine shop for taking so much effort on manufacturing my designs for the BFP system. I would also like to thank Johnafel Crowe for supporting the equipments in the IBB and Dr. Jeffrey Donnell for revising my thesis.

Special thanks to previous and current Zhu lab members. Firstly I would like to thank Dr. Kong Fang for helping me so much on solving technical problems when I was setting up the BFP, Dr. Jizhong Lou, Dr. Fang Zhang, Dr. Ning Jiang, Dr. Veronica, Wei Chen, Dr. Jun Huang and Dr. Tao Wu for their useful discussion on my research works, Larissa Doudy for supporting my BFP experiments in the last year of my Ph.D. research, and William Madison Parks for his help on revising my thesis. I also would like to thank my friends for their helps in the passed five years.

Finally, I would like to thank my family for supporting me in the passed five years. Especially, I would like to thank my wife and my mother in-law when I am writing this Ph.D. thesis. Without your caring and love, it would be much harder to finish my Ph.D. works.

TABLE OF CONTENTS

Page

ACKNOWLEDGEMENTS I

LIST OF FIGURES VI

LIST OF SYMBOLS AND ABBREVIATIONS XII

SUMMARY…… 1

CHAPTER 1 OBJECTIVES 5

1.1 Specific aim 1: to implement a bio-membrane force probe (BFP) and characterize its capacity to study specific interactions between receptors and ligands 5

1.2 Specific aim 2: to develop a thermal fluctuation assay to monitor receptor-ligand interactions between two opposing surfaces. 6

1.3 Specific aim 3: to functionally study the force and force history dependent lifetimes of selectins-ligand interactions. 7

1.4 Specific aim 4: to characterize the force-dependent dissociation of LFA-1/ICAM-1 interaction on a living cell. 8

1.5 Specific aim 5: to probe force-regulated dynamic global conformational change of LFA-1 integrin on a living cell. 9

CHAPTER 2 BACKGROUND 12

2.1 Cell adhesion and cell adhesion molecules (CAMs) 12

2.1.1 Selectins and their ligands 14

2.1.2 Integrins and their ligands 16

2.1.3 Regulation of LFA-1 activity 20

2.1.4 Conformational changes of LFA-1 integrin 22

2.2 Receptor-ligand binding kinetics 26

2.2.1 General receptor-ligand kinetics 26

2.2.2 Force-regulated off-rate 27

2.2.3 Forward association rate (2D-on-rate) of surface-anchored molecules 29

2.3 Single molecule techniques and assays 30

2.3.1 Single molecule techniques 30

2.3.2 Experimental assays to measure kinetics of receptor-ligand interactions 31

CHAPTER 3 MATERIALS AND METHODS 35

3.1 Cells, Proteins and Small Molecules 35

3.1.1 Cell isolation and culture 35

3.1.2 Proteins, antibodies and small molecule antagonists 36

3.2 Coupling biotins onto RBCs and proteins onto glass beads 37

3.2.1 Coupling biotins onto RBCs 38

3.2.2 Coupling proteins onto glass beads via PEG polymer linkage 38

3.2.3 Coupling proteins onto glass beads via biotin-streptavidin’s bond 40

3.2.4 Coupling Fc-chimera proteins onto IgG coated glasses beads 40
3.3 Measurement of molecular site density 41
3.3.1 Fluorescence staining 41
3.3.2 Data acquisition 41
3.3.3 Site density determination 42
3.4 The BFP system 42
3.4 Measurement of binding frequency 43
3.5 Measurement of bond lifetimes 43

CHAPTER 4 INSTRUMENTATION AND CHARACTERIZATION OF THE BFP……..... 45
4.1 Instruction 45
4.2 The BFP System 46
4.2.2 The hardware system of the BFP 46
4.2.3 The software system of the BFP 49
4.3 Characterization of the BFP 50
4.3.1 Characterize spatial precision of the tracking system of the BFP 50
4.3.2 Motion-blur correction on the thermal fluctuation of the BFP 51

CHAPTER 5 MONITORING RECEPTOR-LIGAND INTERACTIONS BETWEEN SURFACES BY THERMAL FLUCUTATIONS 57
5.1 Introduction 57
5.2 Results 59
5.2.1 Change in Thermal Fluctuations Identifies Bond Association or Dissociation 59
5.2.2 Measuring 2D Kinetic Rates of Receptor-ligand Interactions 66
5.2.3 Comparison between the thermal assay and the adhesion frequency assay 70
5.3 Discussion 73

CHAPTER 6 FUNCTIONAL STUDY OF FORCE REGULATION ON SELECTIN-LIGAND INTERACTIONS 78
6.1 Introduction 78
6.2 Results 81
6.2.1 L-selectin hinge mutation augmenting catch bonds in low force regimes. 81
6.2.2 Tri-phasic transition of fore-regulated off-rates of selectin-ligand interactions 84
6.2.3 Force-history dependent off-rates of L-selectin-ligand interactions 87
6.3 Discussion 89

CHAPTER 7 FORCE REGULATION ON LFA-1-LIGAND INTERACTIONS.. 94
7.1 Instruction 94
7.2 Results 96
7.2.1 Binding specificity in the BFP experiment 96

7.2.2 Observation and characterization of catch bonds in the LFA-1/ICAM-1 interaction 98
7.2.3 Binding of XVA143's to LFA-1 abolished LFA-1-ICAM-1's catch bonds 102
7.3 Discussion 104

CHAPTER 8 PROBE FORCE REGULATED DYNAMIC CONFORMATIONAL CHANGES OF LFA-1 INTEGRIN ON A LIVING CELL 108

8.1 Introduction 108
8.2 Results 112
8.2.1 Observations of the upward and downward movements of the probe beads after the PZT stopped 112
8.2.2 Statistical analysis of probe beads movements reveals integrin's global conformational changes 115
8.2.3 Mechanical analysis further confirmed the observed conformational changes of LFA-1 integrin 122
8.2.4 Characterization of dynamic properties of global conformational changes of LFA-1 127
8.3 Discussion 129

CHAPTER 9 RECOMMENDATIONS FOR FUTURE WORKS 136

REFERENCES 142

LIST OF FIGURES

Figure 2-1 Leukocyte trafficking cascade [2]. 14

Figure 2-2. Schematic molecular structures of three selectins. 16

Figure 2-3. Integrin Family. Integrin α and β subunits form 24 heterodimers that recognize distinct but overlapping ligands. Half of the α subunits contain αA domains (asterisked) [13, 14]. This figure was adapted from ref.[13] 17

Figure 2-4. Integrin architecture. A) Organization of domains within the primary structure. Some α subunits contain an A domain inserted in the position denoted by the broken lines. Cysteines and disulphide bonds are shown as lines below the stick figures. Red and blue asterisk denote Ca^{2+}- and Mn^{2+}- binding sites, respectively. B) Crystal structures of αvβ3[15] adapted from [16] C) Arrangement of domains within the three-dimensional crystal structure of αvβ3[15], with an αA domain added. Each domain is color-coded as in Figure 2-4A. β-TD, β tail domain; I-EGF, integrin-epidermal growth factor domain; PSI, plexin/S.E.M.aphoring/integrin [14]. (A) and (C) are adapted from ref.[14]..... 18

Figure 2-5. ICAM-1 Structure and binding to integrin. (A) Schematic of ICAM-1 structure. αLβ2 binding site is indicated by the green star. (B) Model of ICAM-1's binding to αL A domain[16]. 20

Figure 2-6. Ribbon diagram of the crystal structures of open and closed αA domain from integrin $\alpha_{M.}$[33]. 23

Figure 2-7. Global and local integrin conformational states [14, 15, 29, 39, 42]. A) EM image of negatively stained average projections of clasped αXβ2, showing bent conformation with closed headpiece [42]. B) EM image of negatively stained average projections of clasped αXβ2 integrin in the presence of activating antibody, showing extended conformation with closed headpiece[42]; C) EM image of negatively stained average projections of unclasped αXβ2 integrin in the presence of activating antibody, showing extended conformation with open headpiece[42]; D) Model structure of bent αLβ2 with the close headpiece[15]. E) Model structure of the αLβ2 intermediate structure with close headpiece and extended conformation. The binding site of small allosteric molecule(XVA143) is drawn as three red balls[14]. F) Model structure of the αLβ2 extended conformation with open headpiece upon ICAM-1 binding..... 25

Figure 3-1. Plots of raw BFP lifetime data. (A) Plot of force vs. time in the absence of force. (B) Plot of force vs. time in the presence of force. 44

Figure 4-1. Schematic of the BFP system. 47

Figure 4-2. Imaging tracking region and intensity profile for the BFP. (A) Image analysis region, the bright area, for tracking system, the dark area was blocked out not for analyzing. The tracking edge is indicated by the yellow arrow. (B) Intensity profile of the bed's edge in (A). The region in (B) corresponds to a smaller region in (A) which is indicated by a red marker. The orange point in (B) is the peak of Gaussian distribution fitting to the profile. 50

Figure 4-3. Characterization of the tracking precision of the BFP. (A) Comparison of the piezo displacements (green, □) and the tracked displacements (red, ○). The differences between them are shown as blue (Δ)). (B) Histogram (bars) of the differences between the piezo and tracked displacements. It is fitted by a Gaussian distribution (curve) 51

Figure 4-4. Illustrations of thermal fluctuations. Tracked displacements of the target pipette (A), the force probe (B) and the probe pipette (C) over time during which both pipettes were held stationary. (D) Comparison of the 15-point sliding standard deviations of the fluctuating displacements in A-C (color-matched). 53

Figure 4-5. Calibration of the BFP spring constant. (A and B) The background-subtracted drift-free variance var(Xm) of a BFP force probe (○) is plotted vs. reciprocal suction pressure 1/*p* under which the fluctuating displacements were measured in hypotonic (A) or isotonic (B) condition (contributed by Dr.Veronika in Dr.Zhu's lab) and fitted by motion-blur model Eq. 11 (curve). The variances of the target bead (D) and the probe pipette (□) are also plotted in A, which serve as the background. (C and D) The motion-blur corrected variance var(*X*) (○) is plotted vs. 1/*k*p calculated from Equation 4-5 using parameters from the experiments under which the fluctuating displacements were measured in hypotonic (C) or isotonic (D) condition and fitted by a straight linear that passes the origin. 56

Figure 5-1. Thermal fluctuation method. (A) Photomicrograph of a BFP. (B and C) Horizontal position *x* of the right edge of the probe is plotted vs. time *t* for a representative test cycle measuring the interaction between PSGL-1 coated on the probe and L-selectin (B) or P-selectin (C) coated on the target. Two periods of high positions in (B) are indicated by arrowheads. (D and E) Sliding standard deviations σ of 15 consecutive points of the position data in B and C, respectively. (F and G) Histograms of the σ data in D and E (bars), respectively, each fitted by Equation 5-1 (solid curves). Also superimposed on each panel are two histograms of σ values calculated from *x*(t) data of two unencumbered probes recorded for the same duration of time (dotted curves). One unencumbered probe had the same spring constant of k = 0.15 pN/nm as the probe used to acquire the data in D and E. The other unencumbered probe had spring constant of k = 1.7 (F) or 0.8 (G) pN/nm. All histograms were normalized to have a unity area. The vertical dashed line σ_U = 3.8 nm on each panel is one standard deviation (1.3 nm) to the left from the peak at 5.1 nm. The vertical solid line σ_L = 3.15 nm on each panel is 1.5 standard deviation to the left from the same peak. These thresholds are marked in D and E as horizontal lines to identify bond association and dissociation events, which are marked by the respective down and up arrows. Arrowheads indicate intervals deemed indeterminate

as to whether they corresponded to free or bound probes because data lay between the two thresholds. 60

Figure 5-2. Comparison between two methods for determining the presence of a bond. A total of 812 tests like those in Figure 5-1D for L-selectin-PSGL-1 interactions were segregated into two groups. The first group of 87 tests had σ values immediately prior to the target return that were between the upper threshold σ_U = 3.8 nm and the lower threshold σ_L = 3.15 nm, which were deemed as indeterminate and excluded. The second group of 725 tests were further segregated into four subgroups depending on whether they had σ values immediately prior to the target return above the upper threshold (no decreased fluctuation) or below the lower threshold (decreased fluctuation) and whether the returning target produced pulling or no pulling of the probe. The number of tests in each subgroup was plotted against the four conditions marked on the *x*-*y* plane (and also indicated on the top of each bar). 65

Figure 5-3. Exponential distributions of waiting times (A) and bond lifetimes (B). Pooled ensembles of 156 (L-selectin) or 190 (P-selectin) waiting times (A), defined as intervals from a dissociation event to the next association event, and 172 (L-selectin) or 240 (P-selectin) bond lifetimes (B), defined as intervals from an association event to the next dissociation event, of PSGL-1 respectively interacting with L-selectin (Δ) or P-selectin (○) were respectively sorted according to their durations. The natural log of the number of events with waiting times > t_w (A) or bond lifetimes > t_b (B) was respectively plotted against t_w or t_b, respectively, and respectively fitted by a straight line (not shown). The negative slopes of the best-fits represent cellular on-rate $m_r m_l A_c k_{on}$ and off-rate k_{off}, respectively, whose values are indicated. The variations in these values are shown by the 95% confident intervals of the best-fit (lines). The goodness-of-fit was measured by the R^2 values, which are also indicated. 68

Figure 5-4. Kinetic parameters. Cellular on-rate (A) and off-rate (B) were plotted vs. product of the site densities of the interacting molecules, L-selectin and PSGL-1. Data (points, error bar = 95% confident interval) were respectively fitted by a straight line that passed the origin (A) to estimate a molecular 2D effective on-rate $\langle A_c k_{on} \rangle$ (best-fit equation and R^2 were indicated) or by a horizontal line (B) to estimate the average off-rate $\langle k_{off} \rangle$ (indicated). (C) Comparison of kinetic rates of PSGL-1 interacting with L-selectin and P-selectin. 69

Figure 5-5. Comparison between theory and experiment. Frequencies of adhesion mediated by PSGL-1 interacting with L-selectin (Δ) or P-selectin (○) were measured at indicated contact times (points, mean ± S.E.M. of three probe-target pairs) by averaging the adhesion scores (1 for pulling and 0 for no pulling at the end of the contact time of each test cycle) from 100 test cycles per probe-target pair. Theoretical adhesion frequencies as functions of contact time were predicted (curves) by Equation 5-4 using the kinetic rates from Figure 4-4C and molecular densities measured from independent experiments ($m_r m_l$, = 0.2 and 0.15×10^5 μm^{-4} for the L- and P-selectin cases, respectively). 72

Figure 6-1. X-Ray structures of the lectin and EGF domains in P-selectin (A) [8] and

L-selectin (contributed by McEver's lab)(B). 80

Figure 6-2. Binding specificity. 83

Figure 6-3. Bond lifetimes measurement between L-selectin (or L-selectinN138G mutant) and PSGL-1 (A) or 6-Sulfo-sLe^x (B). The data in A, B represent the mean ± S.E.M. of ~500 lifetime measurements. 84

Figure 6-4. Triphasic transition of force-dependent lifetimes of P-selectin-PSGL-1(A), E-selectin-sLex(B), L-selectin-PSGL-1 (C) and L-selectin-6sulfo-sLex bonds (D). 86

Figure 6-5. Raw data of lifetimes at the loading rates of 10^3pN/s (A) and 10^4pN/s (B). . 87

Figure 6-6 Lifetimes of L-selectin-PSGL-1 bond (A) and L-selectin-6-sulfo-sLe^x bonds (B) regulated by force loading rates and clamping forces. 88

Figure 6-7. Sliding rebinding model for selectin-ligand interactions[53]. 91

Figure 7-1. The BFP experiment. (A) Photomicrograph of a BFP. (B) Functionalization of the BFP. ICAM-1-Fc or KIM127 mAb were covalently linked to a streptavidin-decorated probe bead via hetero-bifunctional polymers, maleimide-PEG3500-NHS. LFA-1 integrins with bent or extended conformations were expressed on the Jurkat cell. KIM127's binding site on a LFA-1(light blue star, pointed by the light blue arrow) exposed after LFA-1 extends is on the genu site of the β subunit of a LFA-1. The binding site of allosteric small molecule (XVA143, dark blue balls) is in the αA domain of LFA-1 (pointed by the dark blue arrow). ... 97

Figure 7-2. Binding specificity. Binding frequencies between a Jurkat cell, expressing LFA-1, and a probe bead covalently coated with streptavidin only, streptavidin and ICAM-1 or KIM127 mAb, were measured in ~50 tests of each pair of a target cell and a probe bead at 1mM Mn^{2+}, 1mM Mn^{2+}, 1mM Mn^{2+} plus 1μM XVA143, or 1mM Mn^{2+} plus 100μg/ml soluble ICAM-1 respectively. Error bars represented as mean ± S.E.M. of 3-5 pairs. 98

Figure 7-3. Force-dependent lifetimes of LFA-1/ICAM-1 and LFA-1/KIM127 bonds. (A) Plot of lifetimes (mean ± S.E.M.) vs. force of the interaction between ICAM-1 coated probe bead and the a Jurkat cell at 1mM Mn^{2+}. This plot shows the catch bonds in LFA-1-ICAM-1 bonds. (B) Plot of lifetimes (mean ± S.E.M.) vs. force of interactions between a KIM127 mAb coated probe bead and a Jurkat cell at 1mM Mn^{2+} and 100ug/ml soluble ICAM-1. This plots shows slip bonds in LFA-1-KIM127 bonds. Error bars in both (A) and (B) represent S.E.M.. 100

Figure 7-4. Lifetime analysis. Normalized ln(number of events with a lifetime > *t*) versus *t* plots for interactions of LFA-1 with ICAM-1 within catch bonds regime (A) and

slip bonds regime (B) or with mAb KIM127. Plots in (C) were linearly fitted..... 101

Figure 7-5. Plot of the fraction of events with a lifetimes >10s within each force bin vs. force of the interactions of LFA-1 with ICAM-1..... 102

Figure 7-6. Force-dependent lifetimes of LFA-1/ICAM-1 bonds upon 1μM XVA143 binding and analysis on these lifetimes. (A) Plot of lifetimes as a function of force, fitted by Bell model[43]. Error bars represented S.E.M.. (B) Normalized ln(number of events with a lifetime > t) versus t plots for the interactions of LFA-1 with ICAM-1 upon 1μM XVA143 binding. Each plot is linearly fitted..... 104

Figure 8-1. Photo micrograph of the Bio-membrane force probe (BFP). A micropipette-aspirated biotinylated RBC with a bead (probe) glued to its apex (*left*) was aligned against a cell (target) aspirated by a target micropipette (*right*). B) Functionalization of the BFP. ICAM-1-Fc, mAbs KIM127 or MEM83 were covalently linked on the streptavidin-coated probe bead via maleimide-PEG3500-NHS hetero-bifunctional polymers. LFA-1 integrins with bent or extended conformations were expressed on the target cell. KIM127's binding site on a LFA-1(light blue star) is on the genu site of the LFA-1's β subunit. Allosteric small molecule (XVA143, dark blue balls) binds to the LFA-1's βA domain, induces LFA-1's extended conformations, but locks the αA domain in close conformation and low affinity state. The probe bead moved up and down, indicated by a double headed arrow next to it.....111

Figure 8-2. Experimental observations of abrupt position changes of the probe bead after the PZT stopped. Plots of the position as a function of time (grey circle), showing that the probe bead move up 21nm (A) or move down in ~18 nm (B) after the PZT stopped. The solid gray curve is the smoothed plot of extension vs. time curve. C)-D) Plots of the binding forces measured by the BFP (blue circle) as a function of time, showing force decreases (C) or increases (D) after PZT-driven target pipette stopped (the moment is marked by vertical, dashed and grey line). The solid blue curve is the smoothed force-vs.-time plot. After the PZT stopped, time to force-drop (D) or time to force-increase (D) and the switching time are defined as t_0 and t_{sw} respectively. 114

Figure 8-3. Scatter plots of position changes of the probe bead upward movements (A) or downward movement (C) after the PZT stopped versus force. These two plots show that the displacements of position changes of BFP's probe beads were not dependent on binding forces between LFA-1 and ICAM-1. The average of the position changes of upward or downward movements of the probe bead (solid line) and one σstandard deviation (dashed lines) are superimposed on the scatter plots. On left side of each scatter plot is the corresponding histogram of the position changes fitted with Gaussian distribution (solid grey line) (B, D).....116

Figure 8-4. Comparison of the mean displacements of upward or downward movements of the BFP probe bead. The probe bead coated ICAM-1 were tested with three different types of cells (K562, PMN and Jurkat cells), and all of them expressed LFA-1, Error bars represent S.E.M......118

Figure 8-5. Comparison of occurrence frequencies of upward and downward movements of probe beads. A) Comparison of the occurrence frequencies of upward or downward movements of the BFP probe bead between LFA-1 integrin and its ligand (e.g., ICAM-1) at different conditions (2mM Mg^{2+}/EGTA, 1mM Mn^{2+}) or between LFA-1 and mAbs MEM83 (at 2mM Mg^{2+}/EGTA or 1mM Mn^{2+}) or KIM127 (at 1mM Mn^{2+} plus 100μg/ml sICAM-1). B) XVA143's dose-dependent occurrence frequencies of upward or downward movements of the BFP probe beads. XVA143's does ranges from 0 nM to 1000 nM. 121

Figure 8-6. Plot of force vs. extension for measuring molecular compliance. The slope of red dashed line provides the cellular compliance k_c, while the slope of the blue dashed line provides the effective compliance (k_{eff}) which represents two springs in serial. 123

Figure 8-7. Histograms of molecular spring constants of LFA-1-ICAM-1 complex at the condition of 2mM Mg^{2+}/EGTA (A) or at the condition of 1mM Mn^{2+}. Two sub-populations of the histograms were fitted by Gaussian distribution (red and blue solid line in (A) and dashed line in (B) respectively. 124

Figure 8-8. Plots of spring constants of LFA-1-ICAM-1 bonds versus XVA143's doses at the conditions of Mg^{2+}/EGTA (bottom dashed line), Mn^{2+} without or with different concentrations of small alloestric molecule, XVA143, and spring constants of LFA-1-KIM127 bonds at the conditions of 1mM $Mn^{2+}$and 100μg/ml soluble ICAM-1(upper dashed line). Error bars represent S.E.M.. 125

Figure 8-9. Histograms of molecular spring constants of LFA-1-1-ICAM-1 bonds of increased (gray) or decreased (yellow) displacements. Each histogram was fitted by different Gaussian distributions. The blue one (solid line) fits the histogram of increased displacements (gray), and the peak of this fitting is about 0.16 pN/nm. While the red one (dashed line) fits the histogram of decreased displacements (yellow), and the peak of this fitting is about 0.97 pN/nm. 127

Figure 8-10. Characterization of the conformational changes of LFA-1 integrins. A) Plots of switching times of conformational changes of LFA-1 integrins as a function of binding force. B) Comparison of average switching times between extension or bent-back of LFA-1 integrins on K562, PMN and Jurkat Cells. Error bars represent S.E.M.. C) Comparison of t_0, time to conformational changes after the PZT stops between extension or bent-back of LFA-1s on K562, PMN and Jurkat Cells. Error bars represent S.E.M.. 129

LIST OF SYMBOLS AND ABBREVIATIONS

6-Sulfo-sLe^x	6-sulfo-sialyl-lewis x
A_c	Contact area
AFM	Atomic force microscopy
BFP	Bio-membrane force probe
BSA	Bovine serum albumin
CR	Consensus repeat
DFS	Dynamic force spectroscopy
EDTA	Ethylene diamine tetraacetate
ECM	Extracellular matrix
EM	Electronic microscopy
GPCR	G-protein coupled receptor
HBSS	Hanks balanced salt solution
ICAM	Intercellular cell adhesion molecule
K_a	Affinity
K_D	Dissociation constant
k_{off}, k_{on}	Off-rate (reverse rate) and on-rate (forward rate)
LFA-1	Lymphocyte function-associated antigen-1
mAb	Monoclonal antibody
MHC	The major histocompatibility complex
m_l ,m_r	Site density of ligand, receptor
nm	Nanometer
OT	Optical tweezers
P_a	Adhesion probability (frequency)
PBS	Phosphate buffer saline
PE	Phycoerythrin
PMN	Polymorphonuclear leukocyte (neutrophil)
pN	Pico-Newton
PSGL-1	P-selectin glycoprotein ligand-1
RT	Room temperature
S.E.M	Standard error of the mean
sLe^x	Sialyl-Lewis x
TCR	T cell receptor
VCAM	Vascular cell adhesion molecule

SUMMARY

Cell adhesion plays an important role in inflammation and immunological responses. Adhesion molecules (e.g., selectins and integrins) are key modulators in mediating these cellular responses. Selectins, including L-, E- and P-selecitns, initiate and mediate leukocytes' tethering to and slow rolling on the vascular endothelial surfaces during leukocyte trafficking. Integrins (e.g., $\alpha 4\beta 1$ and $\alpha L\beta 2$) further slow down the selectin mediated slow rolling, and then completely arrest leukocytes by forming firm adhesion with their ligands (e.g., VCAM-1 and ICAM-1). Finally, integrins help arrested leukocytes to migrate out of blood vessels toward injured tissue. All above trafficking cascades occur under a very complicated mechanical environment with a very wide range of shear stresses.

The ability of these adhesion molecules to function in this complex, mechanically stressful environment has been attributed to their very special force-dependent kinetics, which are tightly tied to their molecular structures. It has been well demonstrated that shear flow could enhance leukocyte's tethering, and that catch bonds could regulate leukocytes rolling by prolong bond lifetimes of selectin/ligand interactions. Similarly, shear stress has also been known to regulate leukocyte adhesions by altering integrin's adhesiveness to its ligands. It is believed that the force-dependent kinetics of selectin and integrin interacting with their ligands are regulated through conformational changes in their molecular structures. Thus, the central theme of this thesis is to investigate the relation between force and kinetics rates and to dissect its mechanism on molecular basis.

In order to study the relation between force, kinetic rates and structural conformational changes, an advanced single molecule instrument, the bio-membrane force probe (BFP), was implemented to explore these fundamental biological questions. The spatial and temporal precisions of this newly implemented the BFP were about 3nm and 0.8 ms respectively. The spring constant of the BFP force probe was able to be set over a large range from 0.1 pN/nm ~ 1.2 pN/nm by adjusting aspirating pressures on the force probe. The BFP spring constant was calibrated using the equipartition theorem with motion blur correction. The calibration results suggested that the estimate of the BFP spring constant by Evans' model was accurate enough at hypotonic but not isotonic conditions. Thus, this instrument allowed us to measure force-dependent lifetimes of individual molecular bonds with a force sensitivity of ~1 pN and to detect molecular conformational changes larger than ~5 nm.

Since few convenient assays existed for scientists to directly measure 2D association rates of surface-anchored receptor-ligand interactions, we developed a new thermal fluctuation assay to monitor P-, L-selectin and PSGL-1 interactions between two opposing surfaces and to estimate their 2D on-rate and off-rates simultaneously. This assay used the deduction/resumption of the thermal fluctuations of the force probe to determine individual bond formation and association and then to estimate the kinetic rates by analyzing waiting times between two consecutive bond formations and the lifetimes of each bond. Compared to the adhesion frequency assay, this new thermal fluctuation assay is more efficient and convenient at estimating 2D kinetic parameters of surface-anchored receptor ligand interactions. The differences between estimates of 2D kinetic rates using the thermal fluctuation assay and the adhesion frequency assay were very small.

Using this new BFP, the relation between force and force history of selectin-ligand interactions was investigated. Based on the sliding rebinding model, the flexibility of L-selectin is an important factor regulating selectin's catch bonds. The lifetimes of bonds between the L-selectin hinge domain mutant (L-selectinN138G) and ligands were measured. The lifetime results showed that increasing the flexibility of the lectin domain by eliminating a hydrogen bond in the inter-domain hinge augmented the bond lifetimes in catch bond regimes. More interestingly, one more slip bond regime was observed in all three selectins at lower forces where previous experiments had never measured. All three selectins exhibited tri-phasic transition of force-dependent off-rates in interacting with their ligands. This tri-phasic transition could further support the sliding rebinding model as this model had predicted that breaking the interactions between the lectin and EGF domains before the lectin domain's pivoting could result in a typical slip bond, as postulated by G. Bell. In addition to regulation of catch bonds by biochemical factors, our results showed that biophysical factors (e.g., force loading rates) could also change the catch bonds' behavior. That is, as loading rates increased, L-selectin-PSGL-1's catch bonds gradually shifted to lower force and were completely converted to slip bonds once force loading rate increased to 10^4 pN/s. However, catch bonds in L-selectin-6-sulfo-sLe^x interactions were not changed by these increased loading rates. The mechanism of force loading rating regulation on catch bonds still remains elusive. More deep analysis and experiments are needed to reveal the mechanism.

The BFP was also used to characterize force-dependent lifetimes of LFA-1-ICAM-1 interactions. It has been hypothesized that catch bonds might also exist in LFA-1-ICAM-1 bonds due to the multiple affinity states of LFA-1's ligand binding

domain (αA domain). The experiments on the bond lifetimes between ICAM-1 and LFA-1 expressed on Jurkat cells showed that LFA-1/ICAM-1 bonds indeed behaved as catch bonds. As a control, the lifetimes of LFA-1 and anti-LFA-1 mAb (KIM127) showed slip bonds. Lifetime distributions of catch bonds revealed a two-state transition, while those of slip bonds did not. More importantly, LFA-1-ICAM-1's catch bonds were abolished by the binding of the small allosteric molecule, XVA143, to LFA-1 and converted to slip bonds. This abolishment provided a structural mechanism for catch bonds in LFA-1-ICAM-1 interactions, that is, the downward movement of α7 helix in αA domain adjusted the MIDAS in αA domain to a high affinity state by mechanical forces; such movement may prolong bond lifetimes in lower force regimes.

Finally, the BFP was applied to dynamically probe the global conformational changes of LFA-1 and to characterize force-regulated transitions among different conformational states on a living cell. Our results showed that dynamic transitions of LFA-1 between extended and bent conformations were probed on living cells by the measurement of force-independent distance changes of the BFP probe beads, by examining the frequencies with which these changes occur (they were modulated by cations, small allosteric molecule, XVA143, and different antibodies(i.e., KIM127 and MEM83)), and by mechanical analysis of LFA-1-ICAM-1 complexes in the above conditions. The observed average distance change of LFA-1's extensions was about 18nm, while that of the contraction was only about 14nm. Finally, our results showed that forces could facilitate extension but they slow down contraction of LFA-1. The observed transition time of extension was <=0.1s, while that of contraction was >0.2s.

In summary, our observations here are the first *in-situ* evidence to demonstrate how integrins dynamically transit different conformations and how force regulates these transitions.

CHAPTER 1

OBJECTIVES

The overall objective of this study was to characterize the kinetic and mechanical properties of selectins-ligands as well as LFA-1-ICAM-1 interactions, and to understand how their molecular structures regulate these kinetic and mechanical properties. A bio-membrane force probe (BFP) was implemented and a new thermal fluctuation assay was developed to estimate two dimensional kinetics (2D kinetics) between single receptors and ligands anchored on opposing surfaces. Kinetic and mechanical measurements combined with various statistical analyses were applied to examine force-dependent bond lifetimes and protein conformational changes.

1.1 Specific aim 1: to implement a bio-membrane force probe (BFP) and characterize its capacity to study specific interactions between receptors and ligands

The BFP, an ingenious instrument invented by Dr.Evans, is a very advanced and sensitive technique to probe surface anchored receptor and ligand interactions. It requires very stable and friendly designs of hardware and software systems as well as rigorous tests and characterization. The following sub-aims were used to fulfill specific aim 1.

1.1a. Implementation of the BFP, essentially adapted from the latest version of the BFP in Dr.Evans' lab. This implementation process mainly includes hardware designs and

assembly of the mechanical system, electrical system and optical system, development of several software programs with user-friendly human interfaces for complicated data analysis, and critical dimensional measurements for calculating the BFP's spring constant.

1.1b. Characterization of the spatial and temporal precision of the BFP for estimating its capacity to measure receptor and ligand interactions at the single molecule level.

1.1c. Calibration of the BFP spring constants using the equipartition theorem and motion blur corrections to evaluate the accuracy of the spring constant estimation.

1.2 Specific aim 2: to develop a thermal fluctuation assay to monitor receptor-ligand interactions between two opposing surfaces.

Surface anchored receptor-ligand interactions are mediated by their two dimensional (2D) kinetics, association rates (on-rates) and dissociation rates (off-rates). To date, few assays have been published to estimate the 2D on-rates. But these assays are too complicated to estimate 2D on-rates with very large uncertainties. Thus, in this specific aim, we took advantage of the low stiffness of the BFP force probe to develop a new assay, using the thermal fluctuation changes of the force probe's position, to detect bond formation and dissociation between surface anchored selectins and their ligands. This development included the following sub-aims:

1.2a. Characterization of the thermal fluctuations of the BFP force probe;

1.2b. Validation of the BFP‘s ability to report bond formation and dissociation respectively;

1.2c. Measurement of the 2D kinetics of selectin-ligand interactions using this new

thermal fluctuation assay. Waiting times between two consecutive bond formations and lifetimes of formed bonds were measured based on the thermal fluctuation changes. 2D on-rates and off-rates were then estimated from these waiting times and lifetimes by kinetic models of second order irreversible association and first order irreversible dissociation respectively.

1.2d. Comparison of 2D kinetics measurements between the thermal fluctuation assay and the adhesion frequency assay.

1.3 Specific aim 3: to functionally study the force and force history dependent lifetimes of selectins-ligand interactions.

"Catch bonds", a counter intuitive phenomenon of force prolonged lifetimes, were first observed in P-selectin-PSGL-1 interactions. In the following years, this unusual behavior was reported in many other molecular interactions, such as L-selectin/ligand and GPIb/VWF interactions. However, the structural mechanism of regulating "catch bonds" in molecular structures still remains elusive. Based on the structural differences of the interdomain hinge between crystal structures of P-selectin and L-selectin , Lou *et al.* proposed a sliding rebinding model to explain the structural basis of catch bonds. To test this model and to investigate the force and force history dependence of selectin-ligand interactions, the following sub-aims were used.

1.3a. BFP investigation of the effect of the hinge mutation (L-selectinN138G) on the force-dependent lifetimes of selectin-ligand interactions. Based on the sliding rebinding model, this N138G mutation should slow the dissociation in the catch bond regimes due to its effect on increasing the flexibility of the lectin domain.

1.3b. BFP investigation of tri-phasic force-dependent lifetimes of P-,E- and L-selectin and ligands interactions. Two factors motivate this investigation. First, the sliding rebinding model predicted a slip bond regime should exist in very low force regime. Second, discrepancies existed between published zero-force off-rates from SPR measurments and from the extrapolation of catch bonds of selectin-ligand interactions. We hypothesized that another slip bond should exist in the very low force regime where previous the AFM and the BFP experiments had not measured.

1.3c. Characterization of force-history dependent lifetimes of L-selectin/ligand interactions. Not only could biochemical mutation affect catch bonds, it was also hypothesized that biophysical factors, such as force and force history, could do so as well.

1.4 Specific aim 4: to characterize the force-dependent dissociation of LFA-1/ICAM-1 interaction on a living cell.

Many published works have been already suggested the potential existence of catch bonds in integrin/ligand interactions. However, previous DFS studies failed to reveal the catch bonds in integrin/ligand interactions due to their incorrect assumptions. Based on the published crystal structures of the αA domain and other published experimental results, we hypothesized that the downward movement of the α7 helix in the αA domain adjusting the metal ion dependent binding site (MIDAS) in the αA domain to a high affinity state by mechanical forces may prolong bond lifetimes in lower force regimes. Thus, we used the BFP to measure force-dependent bond lifetimes to investigate this hypothesis by the following steps.

1.4a. Characterization of the force-dependent lifetimes of LFA-1/ICAM-1 interactions on a living Jurkat cell. It was hypothesized that catch bonds existed in this interaction.

1.4b. Characterization of the force-dependent lifetimes of the interactions between KIM127 (anti-LFA-1 mAbs) and LFA-1 integrins. It was hypothesized that the force-dependent dissociation of this interaction should behave as slip bonds.

1.4c. Characterization of force-dependent lifetimes of LFA-1/ICAM-1 interactions upon XVA143's binding to LFA-1. We hypothesized that XVA143's binding abolished catch bonds in LFA-1/ICAM-1 interactions, as this binding blocked the downward movement of the $\alpha 7$ helix so that it locked the αA domain in close and low affinity conformation.

1.4d. Analysis of lifetime distributions in the catch bonds regime in LFA-1-ICAM-1 interactions and the slip bonds regimes in KIM127-LFA-1 interactions as well as in LFA-1-ICAM-1 interactions upon XVA143's binding. It was hypothesized that two binding states may exist in catch bonds while only one state may exist in slip bonds.

1.5 Specific aim 5: to probe force-regulated dynamic global conformational change of LFA-1 integrin on a living cell.

Switch-blade global conformational changes of integrins have been observed in many different integrins by negatively stained EM images. However, these observation were all static and at stress-free conditions. The dynamic properties of these global conformational changes were still not very clear. How mechanical force regulated this dynamic transition also remains elusive. Here, the BFP was used to probe this large scale global conformational change on a living Jurkat cell. The following sub-aims were

carried out for the first time to reveal dynamic transition of LFA-1 integrins between different conformational states.

1.5a Observation of two unusual movements (upward and downward movements) of probe beads after the PZT stopped. It was hypothesized that these upward and downward movements corresponded to LFA-1's extension and contraction respectively.

1.5b Characterization of upward and downward movements of probe beads to support the hypothesis. The distribution of the distance changes of these movements and the force regulation of their distributions were investigated.

1.5c Characterization of the occurrence frequency of these upward and downward movements of probe beads to support the hypothesis. Occurrence frequencies measured at different metal ion conditions were characterized, as different metal ions should have different effects on LFA-1 global conformations.

1.5d Characterization of the effect of XVA143's binding to LFA-1 on the two unusual movements. Since XVA143 could extend LFA-1, the occurrence frequency of moving up and moving down events should be different from that at XVA143 free condition. As well, XVA143-doses dependent occurrence frequencies were also characterized to support our main hypothesis.

1.5e Characterization of the effects of different anti-LFA-1 antibodies' binding to LFA-1 on the occurrence frequencies of upward and downward movements. Based on the known epitopes of KIM127 and MEM83 on LFA-1, it was hypothesized that with KIM127 coated probe beads it would be harder to observe moving up and moving down events, while with MEM83 coated probe beads we would be able to detect unusual movements.

1.5f Mechanical analysis on LFA-1-ICAM-1 and LFA-1-KIM127 molecular complexes

at different conditions (different metal ions or different doses of XVA143) as well as in the cases when upward and downward movements occurred.

1.5g Characterization of force-regulated global conformational changes of LFA-1. Switching times and times to switch were characterized.

CHAPTER 2

BACKGROUND

2.1 Cell adhesion and cell adhesion molecules (CAMs)

Cell adhesion is an important biological and physiological process whereby cells adhere to other cells or to the extracellular matrix (ECM). They do so in order to communicate with each other and to provide necessary biochemical and mechanical signals that regulate and mediate important biological functions, such as leukocyte trafficking, antigen recognition of T lymphotcyte, cell proliferation and differentiation, gene expression, etc. Cell adhesions also play extremely important roles in many patho-physiological diseases, such as inflammation, thrombosis, and cancer.

Cell-cell or cell-ECM adhesion is mediated by specific molecular interactions of proteins or carbohydrates, termed as receptors and ligands, or cell adhesion molecules. To date, at least four major families of CAMs include selectins, integrins, cadherins and members of the immunoglobin superfamily (IgSF). The process of receptor-ligand mediated cell adhesions is a dynamic process, which can be regulated by many intracellular and/or extracellular factors, such as affinity of intracellular or extracellular biological activating signals or mechanical stress. All these factors can regulate the binding affinity of a receptor to its ligand or the densities of receptor and ligand locally or they can globally mediate cell's adhesiveness to other cells or ECM. Thus, adhesion molecules not only stick a cell to a right location, but also form physical

linkages between the extracellular environment and the internal structures of cells and transmit important biological and mechanical signals bi-directionally across the cell membrane.

The leukocyte trafficking cascade has six steps that are mediated by several different receptor-ligand interactions. Since the typical leukocyte trafficking cascade of three steps, rolling, activation and arrest, was proposed in 1994 [1], it has been updated to seven steps supported by numerous published works in this field [2]. These seven steps include capture (or tethering), slow rolling, adhesion strengthening and spreading, intravascular crawling, and paracellular or transcellular transmigration (Figure 2-1) [2]. The selectin family mainly mediates the first two steps, tethering and slow rolling, while the integrin family ($\alpha L\beta 2$, $\alpha 4\beta 1$, $\alpha M\beta 2$, etc) mediates the other steps. Rapid transient binding and unbinding between the selectins and their ligands makes leukocytes slow down and roll along the vascular endothelia [1, 2] (Figure 2-1). During rolling, the leukocyte integrins are activated to a high-affinity state, accompanied by large scale conformational changes and by various biochemical and mechanical signals, and they induce firm leukocyte adhesion on the vascular surfaces. This firm adhesion brings the slow rolling leukocytes to a temporary halt, after which crawling begins and eventually transmigration across the endothelia into the injured tissue. All these directional amoeboid movements of leukocytes are achieved by the chemottractant gradient. Eventually, the leukocytes reach the site of infection by chemotaxis and then they participate in the process of phagocytosis [3, 4].

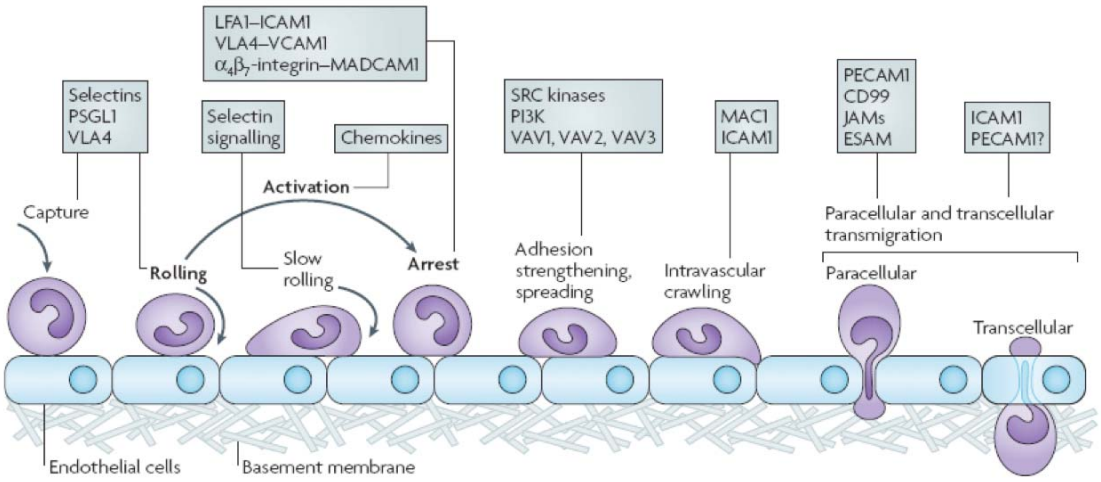

Figure 2-1 Leukocyte trafficking cascade [2].

2.1.1 Selectins and their ligands

The selectins are a family of cell adhesion molecules that play a critical role in mediating leukocyte trafficking during inflammation and immunological responses [5]. In leukocyte trafficking, selectins mainly mediate leukocytes tethering to and rolling on the endothelial surfaces near the inflamed or injured tissue.

The selectin family consists of three known members (Figure 2-2) named according to their expression pattern: 1) L-selectin, exclusively expressed on leukocytes 2) E-selectin, expressed on activated vascular endothelium; 3) P-selectin, expressed on activated platelets but also found on activated endothelial cells. L-selectin's expression is constitutive, but the expression of the vascular selectins (P- and E-selectin) is induced by inflammatory mediators and biochemicals, such as chemokines, from injured sites. P-selectin is stored in preformed granules in vessel endothelia as well as in platelets (Weibel-Palade bodies). Upon stimulation, the P-selectin is almost immediately transported to the vascular surface [1, 6]). Unlike

P-selectin, E-selectin is transcriptionally regulated with a peak expression after 4-6 hours of injury or upon induction of inflammation.

All three selectins share a common structure with a calciumtype lectin domain at the N-terminus (Lectin), an epidermal growth factor-like domain (EGF-like), multiple copies of Consensus Repeat (CRs), a transmembrane domain and a short cytoplasmic tail [5] (Figure 2-2). Crystal structures of the lectin and EGF domains of P- and E-selectin have been published [7, 8]. The ligand-binding region is at the top of the lectin domain opposite to where the EGF domain is attached [8]. This region includes a Ca^{2+}-coordination site that is shared with the fucose in sialyl Lewis x (sLe^x, NeuAcα2-3Galβ1-4[Fucα1-3]GlcNAcβ1-R), a capping structure on glycans of selectin ligands. The lectin domain forms other contacts with sialic acid and galactose and with sulfated components of some glycoproteins. P- and L-selectin bind to the N-terminal region of the leukocyte mucin P-selectin glycoprotein ligand-1 (PSGL-1) through cooperative interactions with sLe^x capping a core 2 O-glycan and with adjacent sulfated tyrosines and other amino acids [8-10]. L-selectin also binds to peripheral node addressin, a group of mucins on high endothelial venules of lymph nodes. The major binding determinant on the O-glycans of these mucins is 6-sulfo-sLe^x, a form of sLe^x with a sulfate ester attached to the C-6 position of GlcNAc [11]. PSGL-1 serves as a ligand for all three selectins. In fact, selectin-PSGL-1 interaction serves as a prototype for other biologically relevant selectin-ligand interactions. L-selectin-PSGL-1 interactions have been implicated in the rolling of one leukocyte over another. Lacking of expressions of selectins or deficiency in selectin-ligand binding is known to impact leukocyte mediated inflammation response[5].

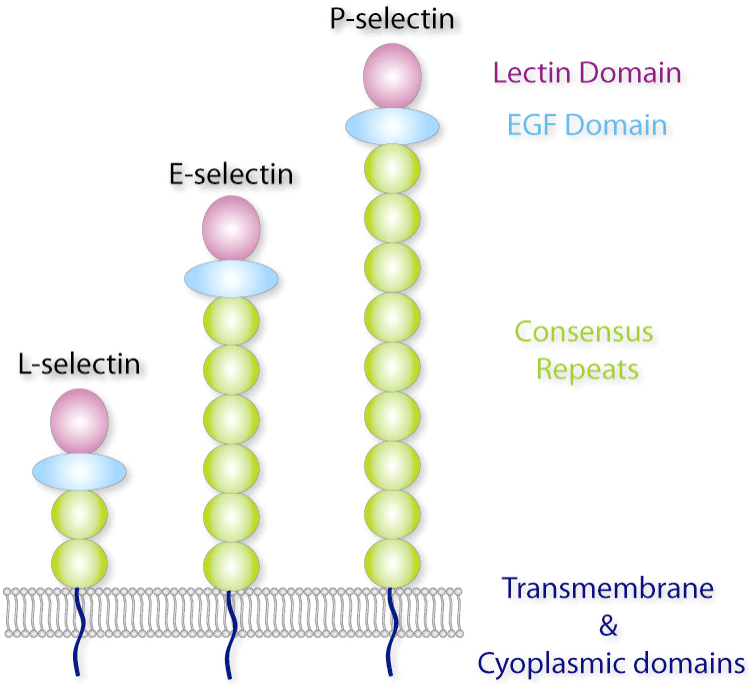

Figure 2-2. Schematic molecular structures of three selectins.

2.1.2 Integrins and their ligands

Integrin Family

Integrins are a large family of cell trans-membrane receptors that play important roles in mediating cell-ECM and cell-cell adhesion, cell migration and cell differentiation. To date, at least 18 different β subunits and 8 α subunits have been identified in vertebrates to form at least 24 heterodimers (Figure 2-3)[12, 13]. Half of integrins contain αA domain (e.g., αLβ2) which is the only ligand binding domain, while the other half lacks αA domains (e.g., α4β1).

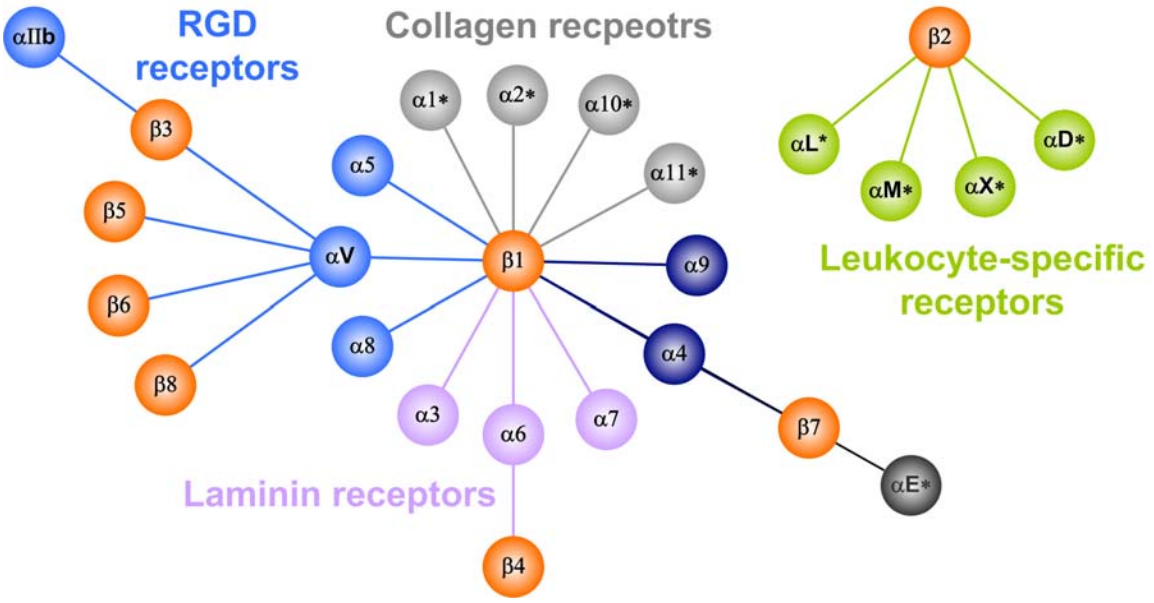

Figure 2-3. Integrin Family. Integrin α and β subunits form 24 heterodimers that recognize distinct but overlapping ligands. Half of the α subunits contain αA domains (asterisked) [13, 14]. This figure was adapted from ref.[13]

aαLβ2 (CD11a/CD18) is also known as lymphocyte function-associated antigen-1 or LFA-1 [4]. αLβ2, together with αMβ2 (CD11b/CD18, Mac-1), , αXβ2 (CD11c/CD18, P150,95), and αDβ2 (CD11d/CD18) constitute β2 integrin family, also called leukocyte integrins (Figure 2-3)[13]. All of β2 integrins contain αA domain, the only ligand binding domain. This β2 integrin family mainly mediated leukocyte's functions in many physiological processes, such as leukocyte trafficking and immunological synapse formation during antigen recognition of T lymphocyte. The discovery of the genetic basis of an inherited disease called leukocyte adhesion deficiency (LAD) syndrome, which manifests as defect in leukocyte adhesion and is caused by the lack of expression of β2 integrins on the cell surface[13].

Architecture of the αLβ2 integrin structure

LFA-1 is a heterodimeric glycoprotein with multiple domains. It comprises two non-covalently-associated type-I transmembrane glycoprotein α subunit (~120–180 kDa) and β subunit (~90-120 kDa). Each subunit contains a large extracellular domain, a single transmembrane domain and a short cytoplasmic tail (Figure 2-4). The N-terminal portions of each subunit combine to form a globular ligand-binding "head" connected to the membrane by a longstalk (~170Å).

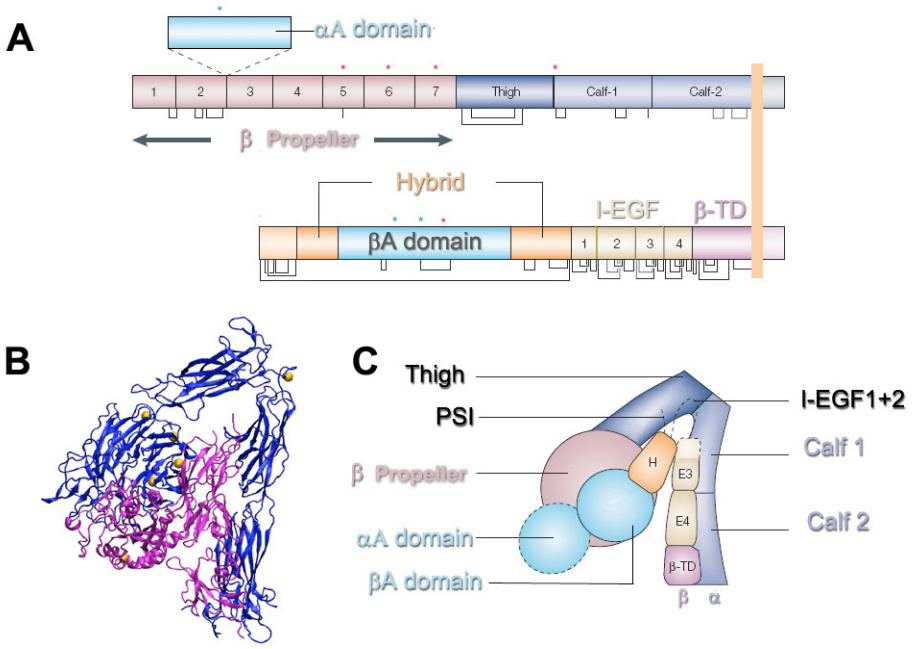

Figure 2-4. Integrin architecture. A) Organization of domains within the primary structure. Some α subunits contain an A domain inserted in the position denoted by the broken lines. Cysteines and disulphide bonds are shown as lines below the stick figures. Red and blue asterisk denote Ca^{2+}- and Mn^{2+}- binding sites, respectively. B) Crystal structures of αvβ3[15] adapted from [16] C) Arrangement of domains within the three-dimensional crystal structure of αvβ3[15], with an αA domain added. Each domain is color-coded as in Figure 2-4A. β-TD, β tail domain; I-EGF, integrin-epidermal growth factor domain; PSI, plexin/S.E.M.aphoring/integrin [14]. (A) and (C) are adapted from ref.[14].

Ligands of LFA-1 (αLβ2) integrin

Physiological ligands of LFA-1 include intercellular adhesion molecule (ICAM)-1,-2, and -3 [6, 7]. Two additional ligands, ICAM-4 and -5 have also been shown to bind specifically to LFA-1, but their physiological function is currently not clear [6, 8]. ICAM-1, -2, and -3 are structurally related glycoproteins that belong to the immunoglobulin superfamily (IgSF). Among them, ICAM-1 (CD54) is the major ligand for αLβ2. Its binding to αLβ2 mediates most biological functions of leukocytes.

ICAM-1, a Type-I transmembrane glycoprotein of 85–110 KDa, composed of five IgSF domains (D1-5), a trans-membrane domain, and a short cytoplasmic tail that binds actin (Figure 2-5A) [17]. It is expressed at relatively low basal levels on leukocytes and several other cell types, such as endothelial cells, but the expression is induced or greatly increased by various pro-inflammatory cytokines, phorbol esters or even shear stress [10, 11]. ICAM-1 is important for leukocyte trafficking and the development of specific immunological synapse in antigen recognition of T lymphocyte [12, 18]. Among the five Ig-like domains of ICAM-1, only the structure of domains 1-2 has been solved in X-ray crystallography (Figure 2-5B). The most important residue in ICAM-1 for binding to αLβ2 is Glu-34, which has been shown to ligate the Mg^{2+} in the MIDAS of the I domain[19](Figure 2-5B).

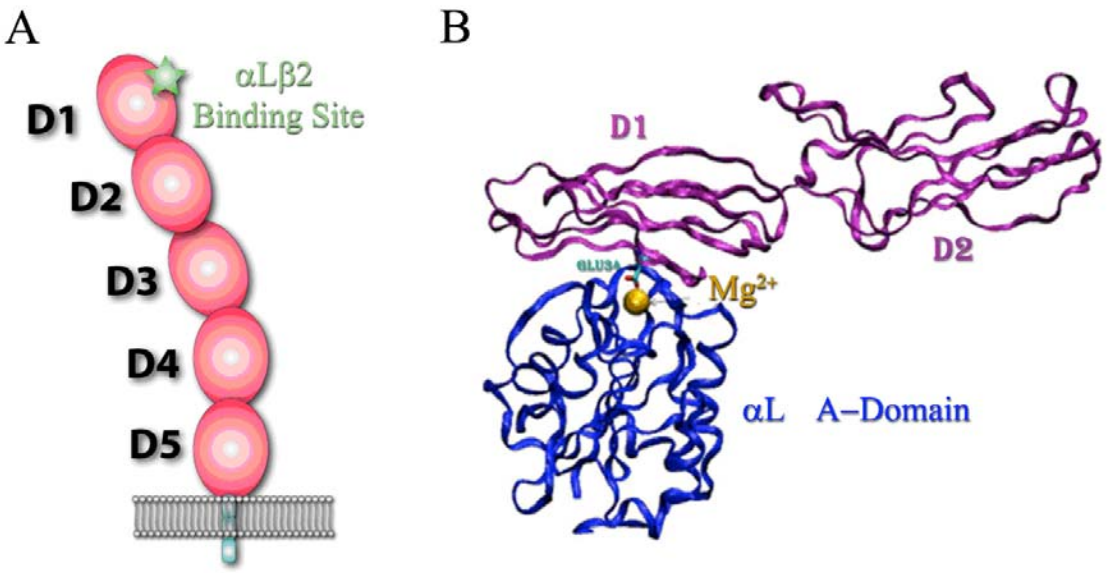

Figure 2-5. ICAM-1 Structure and binding to integrin. (A) Schematic of ICAM-1 structure. αLβ2 binding site is indicated by the green star. (B) Model of ICAM-1's binding to αL A domain[16].

2.1.3 Regulation of LFA-1 activity

LFA-1 integrin usually keeps in an inactive state on leukocyte surfaces. In inactive state, it is not very adhesive to its ligand and does not transmit downstream signals into the leukocyte. Its activity and adhesiveness need both local and global spatial and temporal regulations, which are very important for biological functions of LFA-1. During leukocyte trafficking in blood vessel, it is critical that LFA-1 remain inactive and non-adhesive to ICAM-1 on the surfaces to avoid unnecessary inflammation response. As well, when lymphocyte migrate inside of lymph node, LFA-1's adhesiveness needs to be shut down to help lymphocyte searching for cognate antigen. Once receiving correct signals (e.g., mechanical force or inside out signaling from chemokines receptors), LFA-1 can be [20] rapidly activated to high affinity state to allow proper immune

functions. Defects in either have pathological consequences and thereafter caused diseases. Therefore, the regulation of LFA-1 activity has become therapeutic targets for inflammatory diseases, autoimmune diseases, and cancer [32].

Even though within these years tremendous efforts have been made for studying LFA-1, the mechanism of how LFA-1's activity is regulated still remains elusive. But it is believed that molecular conformation or redistribution of the molecule in cell membrane seems most likely contributing to regulate LFA-1's affinity or avidity respectively. The affinity change is resulted by the conformation changes in a single molecule, while the avidity changes by LFA-1's redistribution on cell surfaces.

Dynamic regulation of LFA-1 activity requires integration of signals initiated by a wide range of biological or physical stimuli. Two main signaling pathways for integrins have been identified, termed "inside-out" and "outside-in" signaling pathways. "Inside-out" signaling transduction happens from the inside to the outside of cell, and activating signal is initiated by other receptors, such as T-cell receptor or G protein coupled receptor (GPCR)[18], and then transmitted through several adaptor proteins (e.g., talin) along cytoskeleton to the cytoplasmic tails of LFA-1 integrins. After receiving activating signals on its tails, LFA-1 separates its transmembrane and intracellular regions [21] and rearranges its extra-cellular domains to adopt high affinity conformations to its ligands [12]. In contrast, outside-in signaling is induced by ligand binding outside the cell membrane and then transmitted into the cell. Since ICAM-1 exists in multivalent manner, LFA-1's ligation to it may result in clustering of LFA-1 on cell surface, and thus enable the recruitment of signaling molecules to LFA-1's cytoplasmic tail to initiate downstream signaling events [20]. Outside-in signals could

also induce global conformational changes of LFA-1 and separation of LFA-1's tails followed by a series of downstream signaling.

2.1.4 Conformational changes of LFA-1 integrin

Conformational changes in αA domain

Isolated αA domain exists in two conformations, closed and open conformations (Figure 2-6), which equate respectively with the low- and high- affinity states of ligand binding [22-26]. All three MIDAS loops rearrange as the domain switches from the close to the open state (Figure 2.5). This appears to be driven by a major restructuring of the β6-α7 loop and is associated with a 10Å downward movement of the α7 helix. The rearranged contacts of the β6-α7 loop with the hydrophobic core lead to a 2Å inward pull of α1 helix, resulting in the open MIDAS configuration. The hydrophobic core plays a critical role on locking the β6-α7 loop at different states. The axial downward movement of the α7 helix allosterically changes the conformation of MIDAS. Some mutations that stabilize the closed or open conformation have exhibited constitutively low or high affinity for ligand, respectively [23, 27-31]. Mechanical force could also stabilize α7 helix in high affinity position after pulling the α7 helix down so that force potentially could increase bond lifetime (so-called "catch bonds") [32]. But, to date, "catch bonds" have not been observed in integrin/ligand interactions.

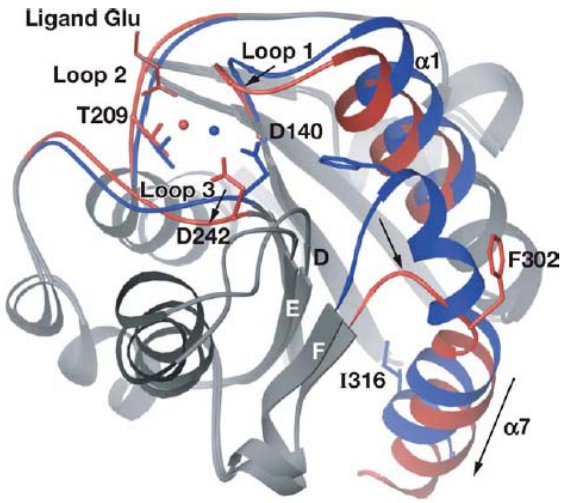

Figure 2-6. Ribbon diagram of the crystal structures of open and closed αA domain from integrin $\alpha_{M.}$[33].

Global conformational changes of LFA-1 integrin

In addition to the conformational changes in αA domain, LFA-1 has larger scale global conformational changes like a switch-blade. Since the crystal structures of αVβ3 extracellular segment alone[15] and with RGD peptide[34] provided us a surprising feature of knee-bent V shape conformation of $\alpha_V\beta_3$ integrin, subsequent research has confirmed that this conformation exists naturally in αVβ3 integrin as well as in other integrins: 1) recombinant integrin image visualized by electron microscopy (EM) in the presence of Ca^{2+} (Figure 2-7 A) [35, 36] revealed a bent form, consistent with the bent crystal structure (Figure 2-7 D); 2) exposure of epitopes which are buried in the genu or knee region[37] also showed the bent form; 3) observation between integrin bearing fluorescent ligands and lipid bilayers on cell surface by FRET [38] suggests that ligand binding site is within ~100Å of the lipid bilayers, consistent with the observed bent

structure. Further, the extended conformation was also observed under ligand binding condition or Mn^{2+} by EM[39] and FRET[38, 40]. But whether such bent conformation representing the low affinity state is still debatable, since another EM study of αVβ3 and its ligand complex [36] published a different view that is a bent conformation of αVβ3 can still stably bind to its ligand.

It is well believed that at least three different conformational states of integrins co-exist on cell surfaces but with different distributions[39] at different stimulating conditions. These three different confirmations are termed bent close headpiece conformation (Figure 2-7A and D), extended form with close headpiece (intermediate states) (Figure 2-7B and E), and extended form with open headpiece (Figure 2-7 C , F and G). Integrins can switch between any of these two conformations upon binding to different stimuli. For example, when small allosteric molecule (XVA143) binds to LFA-1 on the MIDAS of βA domain, it can induce about 20nm extension in LFA-1 and make the βA domain adopts high affinity conformation by swinging out the hybrid domain. But XVA143's binding also blocks the α7 helix downward movement and binding to βA domain so that it locks the αA domain in close and low-affinity conformations (Figure 2-7 F) [14]. Based to EM images of αLβ2 and αXβ2 and model structures of αLβ2, αLβ2 extends about 20nm from bent to extended conformation.

To date, most of published works about single integrin global conformational changes are static, and all experiments were done in stress free condition. Even though it has been know that force could enhance LFA-1's adhesiveness upon chemokine's activation[18, 41], no any publish work has ever shown that how force regulates this large scale global conformational changes and whether force can strengthen the

LFA-1/ICAM-1 interactions and how. As well, the dynamic properties of these conformational changes still remain unknown.

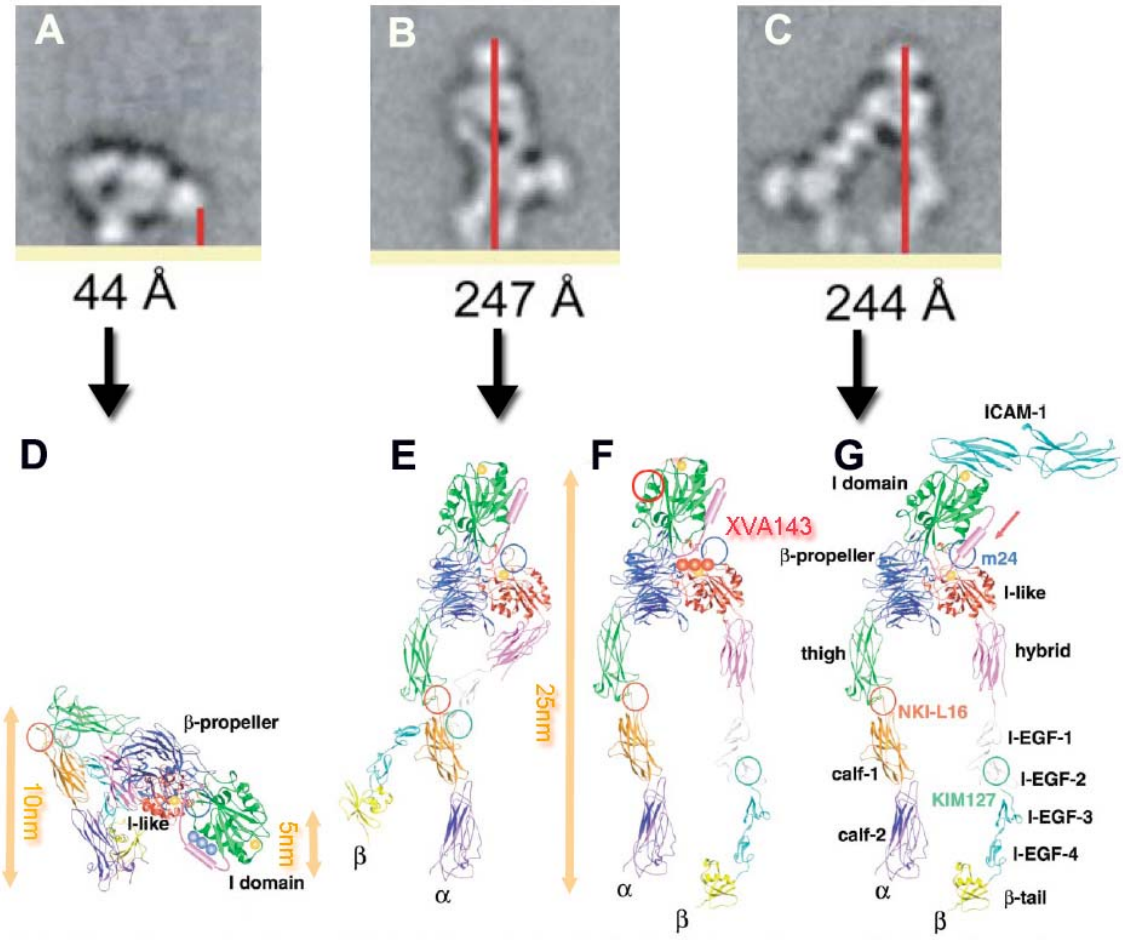

Figure 2-7. **Global and local integrin conformational states [14, 15, 29, 39, 42].** A) EM image of negatively stained average projections of clasped αXβ2, showing bent conformation with closed headpiece [42]. B) EM image of negatively stained average projections of clasped αXβ2 integrin in the presence of activating antibody, showing extended conformation with closed headpiece[42]; C) EM image of negatively stained average projections of unclasped αXβ2 integrin in the presence of activating antibody, showing extended conformation with open headpiece[42]; D) Model structure of bent αLβ2 with the close headpiece[15]. E) Model structure of the αLβ2 intermediate structure with close headpiece and extended conformation. The binding site of small allosteric molecule(XVA143) is drawn as three red balls[14]. F) Model structure of the αLβ2 extended conformation with open headpiece upon ICAM-1 binding.

2.2 Receptor-ligand binding kinetics

2.2.1 General receptor-ligand kinetics

For a receptor-ligand interaction, we usually use standard chemical kinetics framework to model it. For example, the following simple reversible reaction scheme models binding between a free receptor R and a free ligand L to form a bond B:

$$R + L \underset{k_r}{\overset{k_f}{\rightleftharpoons}} B, \qquad \text{Equation 2-1}$$

where k_f and k_r are the respective on-rate (forward rate) and off-rate (reverse rate) constants. These two kinetic rate constants regulate cell adhesion, since these parameters describe how rapidly receptor and ligand associates and how long remain bound [67]. The time rate of the change of the bond concentration [B] is dependent on these two rate constants as well as the free receptor concentration [R] and the free ligand concentration [L]. Their relation is:

$$\frac{d[B]}{dt} = k_f [R][L] - k_r [B], \qquad \text{Equation 2-2}$$

At equilibrium, the concentration of B is constant, as the amount of dissociation of B to R and L is equal to the amount of the newly formed B from the association of R and L, that is, $d[B]/dt = 0$. Therefore, the dissociation constant

$$K_D = \frac{k_r}{k_f} = \frac{[R][L]}{[B]}, \qquad \text{Equation 2-3}$$

The affinity constant is K_A, $K_A = 1/K_D$.

2.2.2 Force-regulated off-rate

In cell adhesion, receptor-ligand interactions behave more complicated than previous described common chemical reactions. Unlike the constant off-rates in chemical reactions, these rates could be regulated by many factors (e.g., forces) in the receptor ligand interactions during cell adhesions process. To date, two types of force regulation of dissociation rates have been identified; one is called slip bonds, in which force shortens bond lifetimes, and the other one is called catch bonds, in which force prolongs bond lifetimes[43, 44].

Slip bond

Slip bonds, a phenomenological term to describe force-regulated receptor-ligand dissociation rate, were first postulated by George Bell in 1978 [43]. His model indicated that the off-rate of receptor-ligand interactions was exponentially related to the force exerted on the receptor-ligand bond. From the viewpoint of the energy landscape, an applied force could lower the energy barriers hindering the receptor-ligand dissociation so that it accelerate dissociation of the non-covalent interactions between receptor and ligand[45]. Mathematically, the dissociation rate, k_{off} can be represented [43] as:

$$k_{off} = k^{0}_{off}\exp\left(\frac{-E_b(f)}{k_B T}\right) = k^{0}_{off}\exp\left(\frac{-f x_\beta}{k_B T}\right) = k^{0}_{off}\exp\left(-\frac{f}{k_B T / x_\beta}\right) = k^{0}_{off}\exp\left(-\frac{f}{f_\beta}\right), \quad \text{Equation 2-4}$$

where k^{0}_{off} represents the unstressed dissociation rate of receptor-ligand interaction (i.e. the off-rate of the receptor-ligand bond in the absence of any applied

force, f), k_B is the Boltzmann constant and T is the absolute temperature (in Kelvin). $E_b(f)$ is the height of energy barriers between bound and free state. This energy barrier is dependent on applied force[45] so that applying force can lower this height. x_β is the width of the energy barrier. Together with force *f*, it represents the work done on the bond to overcome the energy barrier. f_β is the scale for force by the k_BT. Slip bonds have been reported in many receptor ligand interactions, such as interactions between biotin and streptavidin [46] as well as antigen and antibody[47].

Catch bonds

Unlike slip bonds, catch bonds, a counter-intuitive phenomenon, described that lifetimes increase as applied force increases. Dembo *et al.* first introduced this concept[44] in 1988, but catch bonds were first observed in P-selectin and PSGL-1 interactions in 2003 by Marshall *et al.*[47]. So far catch bonds have been reported in the interactions of selecint/ligand[47, 48], glycoprotein Ib (GPIb) and von Willebrand factor (VWF) [49], actin and myosin [50] and FimH receptor and mannose [51]. Essentially catch bonds are thought to closely relate to the molecular structures of the receptor and ligands. Some structural models have been proposed to explained corresponding catch bonds [52-54]. From the biophysical point of view, two path ways model has been proposed by Evans *et al.* to explained catch bonds in P-selectin/PSGL-1[55] and FimH and manose bonds[54]. Whether catch bonds also exist in other molecule interactions, such as interactions between integrins and their ligand, remains unclear and needs more experimental works

to verify.

2.2.3 Forward association rate (2D-on-rate) of surface-anchored molecules

Forward association rates included two types, 2 dimensions (2D) and 3 dimensions (3D). 3D forward rates describe the association rate of molecules in solution without any restrictions of any surface. Unlike 3D forward rate, the 2D forward kinetic rate describes how fast two molecules that are surface-anchored can bind to each other to form a bond. Essentially, 2D forward rate are more relevant to cell adhesion molecules, because majority of cell adhesion molecules are expressed on the cell membrane.

Many factors can regulated the 2D forward rate, such as the movements and mechanical properties of the surfaces where these molecules are anchored, density of molecules on the surfaces, distance and contact area between to two molecules, temperature, and intrinsic on-rate and flexibility of molecules, which is largely dependent on molecular structure, etc.

Because of this complexity, so far very few assays have been developed to measure this important kinetic rate. Chesla *et al.* [56] developed a adhesion frequency assay to indirectly measure the 2D on-rate by measuring the binding affinity and off-rate of molecular interactions and then divided binding affinity by the off-rate to calculate the on-rate. Yago *et.al* [57]was trying to use flow chamber assay to characterize this on-rate by measuring the tethering rate of cells to a surface. But both methods are not very accurate and efficient to estimate the molecular association rate, because of two reasons: 1) large uncertainty of the on-rates from adhesion frequency assay, as the on-rates is from the measured affinity and off-rate which were obtained from nonlinear fitting a complicated model; 2) too many factors lumped together in the flow chamber assay to

accurately estimate the on-rates[57, 58]. Thus, it is necessary to develop a new assay to easily characterize this 2D on-rate as it is very important for understanding bio-molecular interactions.

2.3 Single molecule techniques and assays

2.3.1 Single molecule techniques

In the past two decades, with the fast development of science and technology, many advanced techniques have sprung out for scientists to study biomolecular interactions at single molecule level. All of these techniques utilized ultrasensitive probes: 1) the atomic force microscopy[47, 59] (AFM) where the force is sensed by detecting the deflection of a micro-fabricated cantilever; 2) the bio-membrane force probe (BFP) [45, 60-62], used in this thesis work, where the force is sensed by tracking axial movement of a glass bead that is glued the apex of a aspirated red blood cell; 3) optical tweezers [59, 63, 64] (OT), where the force is sensed by tracking the position of a bead trapped in a narrowly focused beam of laser light; 4) magnetic tweezers, where the force is sensed by tracking the position of a bead trapped by a magnetic field. Each of these force probe acts as an ultra-soft spring, the spring constant of which ranges from ~0.01pN/nm~1nN/nm. AFM's spring constant is about 10pN/nm~1nN/nm, BFP's is about 0.1~1pN/nm, while OT's and MT's are even softer than the BFP's, <0.01pN/nm[45].

2.3.2 Experimental assays to measure kinetics of receptor-ligand interactions

Adhesion frequency assay

The adhesion frequency assay was originally developed by Chesla *et al.* in 1998[56] to characterize 2D kinetics of receptor-ligand interactions. In brief, Chesla *et al.* developed a model of the binding frequencies measured at different contact durations between surface-anchored receptor and ligand. This model is described as:

$$P_a = 1 - \exp\{-m_r m_l A_c K_a [1 - \exp(-k_{off} t_c)]\}, \quad \text{Equation 2-5}$$

where P_a the adhesion frequency, A_c is the contact area and t_c is the contact duration, m_r and m_l are receptor and ligand surface densities, respectively, AcK_a is the binding affinity, and k_{off} is the dissociation rates. k_{on} can be calculated by K_a*k_{off}.

Equation 2-5 states that the likelihood of observing adhesion, P_a, depends on the time when the observation is made relative to the time when the contact is initiated, i.e., the contact duration, t_c. If the adhesion frequency is measured over a range of contact durations, fitting Equation 2-5 to the measured P_a vs. t_c binding curve then allows estimation of the 2D kinetic rates and binding affinity, provided that the receptor and ligand densities are measured from independent experiments.

Dynamic force spectroscopy (DFS)

Dynamic force spectroscopy was firstly developed by Evans *et al.* in 1997 [65]. DFS measured rupture forces under various steady loading speeds. When bonds are pulled until rupture, k_{off} becomes a function of time as the force on the bond is equal to the loading rate(r_f) multiplied by time *t*. The probability of remaining in a bound state is no longer a simple exponential, and it can be described as

$$P(\mathrm{t}) = \exp\left[-\int_0^t k_r\,(t')dt'\right], \qquad \text{Equation 2-6}$$

The probability density for a bond to be ruptured by a force is then given by:

$$p(f) = \frac{1}{r_f} k_{off}(f) \exp\left(-\frac{1}{r_f}\int_0^f k_{off}(f')df'\right), \qquad \text{Equation 2-7}$$

The peak rupture force is found when $\left.\frac{\partial p}{\partial f}\right|_{f=f^*_{rupture}} = 0$. If a Bell model relationship is used to describe the force dependence of k_{off}, from Equation 2-7, a relationship between peak rupture force and loading rate is found:

$$f^*_{rupture} = \frac{k_B T}{x_\beta} \ln\left(\frac{r_f}{x_\beta t_{off}}\right), \qquad \text{Equation 2-8}$$

The equation predicts a linear relationship between the most probable rupture force and log of the loading rate shown by Equation 2-8. The Bell model parameters (k^0_{off}, and x_β) can be derived from fitting the peak rupture force versus log loading rate graph with a straight line. Most likely the unbinding pathway consists of multiple energy barriers with different linear segments representing different energy barriers. Each separate linear regime in the peak rupture force vs. the $\log_e$ loading rate graph can be attributed to a separate set of Bell model parameters for that energy barrier. This

method has been applied to a number of molecular interactions with most bonds being described by an energy landscape consisting of two energy barriers [66-68].

Flow Chamber Assay

Flow chamber assay has been widely used to study receptor-ligand association and dissociation, especially for leukocyte adhesion molecules, such as selectins and integrins, as flow chamber environment mimics the blood vessel. Many groups [69, 70] have applied the constant force analysis to these experiments to measure the tethering lifetimes in order to determine the off-rate of selectins and integrins as a function of force. Most of reported off rates have been found to be dependent on force in a pattern followed by Bell model..

Additionally, a number of interesting observations have been made. The shear stress could enhance leukocyte's rolling and tethering which were mediated by selectin-ligand interactions [47, 48, 53]. As well, shear stress has been reported to greatly enhance αLβ2's adhesiveness to ICAM-1[41]. Even though catch bonds have been reported to explain the shear threshold phenomenon and the enhancement of leukocyte's rolling under shear, no clearly molecular mechanism to explain the share stress regulation on the enhancement of αLβ2's adhesiveness.

Flow chamber experiment is unable to directly and accurately control the binding event. The BFP allows measurement of single bonds with direct control over the applied force, the duration of the contact, the contact force, and the approach and retraction velocities. The BFP directly measures the applied force and bond lifetimes.

The BFP will be utilized to characterize the selectin-ligand and αLβ2-ICAM-1 interactions in a force range below the level used in flow chamber experiments.

CHAPTER 3

MATERIALS AND METHODS

3.1 Cells, Proteins and Small Molecules

3.1.1 Cell isolation and culture

Isolation of Human Red Blood Cell (RBC)

Human RBCs were isolated from a drop of fresh whole blood via a finger prick. The RBCs were then washed three times with the carbonate/bi-carbonnate buffer (pH 8.4, ~180 mOsm). In each wash, the centrifuging speed was 2000g for 30 seconds to 1 minute. Finally these washed RBCs were stored in the 100μl carbonate/bi-carbonate buffer for a few minutes for the following biotinylation of RBCs.

Isolation of human neutrophils

Human neutrophils were isolated from a drop of whole blood via a finger prick. The RBCs were lysed by brief hypotonic shock with 500μl of dH_2O for 10 seconds. The solution of the lysis was then recovered to isotonic condition by adding 500μl of 1.7% NaCl. The left blood cells were spinned down and re-suspended in 40μl of Hepes buffer (pH 7.4, ~300mOsm) with 1% human serum albumin (HSA, ZLB Plasma, Boca Raton, FL).

Culture of K562 cell line

Human erythroleukemia cell line K562 stably transfected with WT LFA-1 integrin was a generous gift of Dr. Timothy Springer (Harvard Medical School, Boston, MA) [23, 71]. The cells were cultured in RPMI with 10% fetal calf serum with L-glutamine (4mM) and penicillin/streptomycin (0.1mg/ml). Puromycin (4μg/ml) was used as a selection agent for K562 cells expressing LFA-1. Maximum cell densities were ~$5x10^5$/ml.

Culture of Jurkat cell line

Jurkat cell line was established from the peripheral blood of a 14 year old boy who had acute T cell leukemia[72] (American Type Culture Collection(ATCC), MA). The cells were cultured in RPMI with 10% fetal calf serum with L-glutamine (4mM) and penicillin/streptomycin (0.1mg/ml). Maximum cell densities were ~$5x10^5$/ml.

3.1.2 Proteins, antibodies and small molecule antagonists

Selectin- related reagents

The following selectin-related reagents were all generously provided by Dr.Roger.P McEver. L-selectin-Ig, L-selectin mutant-Ig (N138G) and P-selectin-Ig containing the lectin domain, EGF domain, and two or nine consensus repeats of human L- or P-selectin fused to the Fc portion of human IgG1 was expressed as described [73]. 6-sulfo-sLe^x has also been described[73]. Soluble recombinant monomeric PSGL-1 has also been described[73]. Soluble E-selectin has been described[74]. The blocking anti-L-selectin

mAb DREG56 and the blocking anit-P-selectin mAb PL-1 have been previously described[75, 76].

The following fluoresce-conjugated monoclonal antibodies were used to measure the site densities of L-selectin-Ig, L-selectin-mutants-Ig and P-selectin-Ig that were coated on glass beads. The PE-labeled mouse-anti-human mAbs were purchased: anti-PSGL-1 mAb PL1 (Santa Cruz Biotechnology, Santa Cruz, CA), anti-L-selectin mAb DREG-56 (eBioscience, San Diego, CA), and anti-P-selectin mAb AK-4 (eBioscience). Goat anti-human IgG polyclonal antibody was purchased from Chemicon International (Temecula, CA).

Integrin-related reagents

The human ICAM-1-Fc chimera was purchased from R&D Systems. Small molecule antagonists XVA143 was generously provided by Dr. Timothy Springer. The mAb MEM83 was from Abcam (Cambridge, MA) [77]. The mAb KIM127, kindly provided by M. Robinson (Celltech, Slough, U.K.), was used as a conformation reporting antibody[78].

3.2 Coupling biotins onto RBCs and proteins onto glass beads

These covalent link protocols were kindly taught by Dr.Evan Evans and his lab members, Andrew Leung and Koji Kinoshita.

3.2.1 Coupling biotins onto RBCs

Biotinylation of RBCs was used to provide strong linkage on the RBC to connect a streptavidin-coated glass bead. To biotinylated RBCs, a drop of whole blood via finger prick was washed 3 times (2000g, ~30 seconds) with carbonate/bi-carbonate buffer (pH 8.4, ~180mOsm). 2~3mg of the hetero-bi-functional polymer of SGA-PEG-Biotin (MW ~3500Da, JenKemUSA, TX) were measured and mixed with carbonate/bi-carbonate buffer to make a PEG polymer solution of 6mg/ml. To avoid hydrolyzing SGA functional group in the polymer (half-life of hydrolysis of the SGA, ~17minutes), after PEG polymer were diluted in buffer, 50μl of polymer solution should be quickly taken out to be mixed with 3μl of packed RBC pellets and 847μl of carbonate/bi-carbonate buffer. This mixture was then incubated at room temperature for 30 minutes on a rotator. After the incubation, the RBCs were washed 2 times with carbonate/bi-carbonate, and then were washed once with Hepes buffer (pH 7.4, ~300mOsm). Finally the RBCs were re-suspended in 100μl of Hepes buffer (pH 7.4, ~300mOsm) with 0.1% BSA for the BFP experiments.

3.2.2 Coupling proteins onto glass beads via PEG polymer linkage

Step 1: Silanization of glass beads

In order to covalently link proteins via PEG polymer onto glasses beads, glass beads had to be silanized. First of all, glass bead's surface was required to be modified from hydrophobic to hydrophilic in order to enhance protein's coating ratio in the following steps. To do so, glass beads (5mg) were washed with a boiling liquid of H_2O_2 (30%) and

NH_4OH (99%). Glass beads were then cooled down via washing with 50ml dH_2O. These beads were then three more time with methanol (99%) and re-suspended in 100µl methanol (Sigma). After washing, these beads were incubated in a 50ml Cornical tube with 48.1ml methanol, 5ml acetic acid (99%), 1ml dH_2O and 1.5ml MTPMS (United Chemicals) on a rotator. Having been incubated for 3 hours at RT, these beads were washed 3 times with methanol, and then re-suspended in 500µl methanol. This 500µl of beads solution was then divided into 20 glass vials for the following drying step. To dry these beads, each glass vial was exposed to blowing argon for less than 1 minute (try to make glass beads stick on the wall, not on the bottom of the glass vial). All these glass vials with beads were then placed in a pre-heated drying oven for 5 minutes. The temperature of the drying oven was set at 120 ^oC. Finally, all the glass vials were moved into a vacuumed desiccator for overnight cooling. This desiccators was covered a aluminum foil to prevent lights exposure.

Step 2: Hetero-bifunctionalizing silanized beads

After the silanization of glass beads, next step is to covalently link proteins onto glass beads via hetero-bifunctional PEG polymers, such as malimide-PEG3500-NHS polymers (MW ~3500Da, JenKemUSA, TX). Firstly, proteins, such as human IgG1 or ICAM-1, were covalently linked with the polymers. To do so, a certain amount of polymers and proteins were mixed with carbonate/bicarbonate buffer (pH ~8.5) and then incubated for ~30mins at RT. Usually the molar ratio of polymer to proteins was about 10:1. But this ratio was adjusted to suitable coating site densities of proteins in order to make binding frequencies of single molecule experiments on the BFP less than ~20%.

After the incubation, certain amount silanized beads and PBS buffer (pH~6.8) were added into the mixture. This mixture were then Incubated for overnight at RT. During this incubation, the mixture were kept stirring. After the incubation, the mixture was washed with PBS buffer (pH~6.8) twice and hepes buffer (pH ~7.4, 150mOsm) once. Finally these protein-coated beads were re-suspended with hepes (pH ~7.4, 150mOsm).

3.2.3 Coupling proteins onto glass beads via biotin-streptavidin's bond

Streptavidin-malimide (Sigma) were covalently linked on to silanized glass beads. Firstly, streptavidin-malimide solution (66.7uM) and silanized beads were mixed together with PBS buffer (pH~6.8) at RT, and then incubated on a rotator for overnight. During this incubation, the mixture was kept stirring in a 50ml conical tube which was mounted on a rotator. After the overnight incubation, the mixture was washed with PBS buffer (pH~6.8) twice and Hepes buffer (pH ~7.4, 150mOsm) once. Next, these protein-coated beads were re-suspended with Hepes (pH ~7.4, 150mOsm). Secondly, streptavinidated (S.A.) glass beads were incubated with biotinylated proteins (i.e., biotinylated PSGL-1, 6-sulfo-sLex or sLe^x) for 1 hour at RT. Following this incubation, the beads was washed three times with Hepes buffer (pH~7.4). Finally, these beads was re-suspendered in Hepes buffer (pH~7.4).

3.2.4 Coupling Fc-chimera proteins onto IgG coated glasses beads

To prepare Ig-chimera proteins-coated beads, such as L-, P-selectin-Ig, and L-selectin-mutants-Ig,etc, IgG-coated beads (prepared in 3.2.1) were incubated with

Ig-chimera protein in hepes buffer (pH 7.4,~150 mOsm) at 4 °C for overnight. In the second day, these beads was washed with hepes for three times and then re-suspended in hepes buffer (pH~7.4, ~150 mOsm).

3.3 Measurement of molecular site density

3.3.1 Fluorescence staining

Beads coupled with L-selectin/mutants, P-selectin, or PSGL-1 were respectively incubated with PE-labeled DREG-56, AK-4, or PL1 or irrelevant mouse IgG_1 (isotype control) (eBiosciences, CA) for 30 min at RT. Normally, the incubating concentration of these primary mAbs was saturating concentrations (usually 10μg/ml of purified mAb or follow the manufacturer's instruction).

3.3.2 Data acquisition

Site densities of samples were acquired by a BD LSR flowcytometer with FACS DiVa 3.1 software (BD Biosciences). Before running samples, standard beads were prepared and run through firstly for quantification of MESF (molecules of equivalent soluble fluorophore). To obtain the mean intensities of calibrated microbeads with five different molecular site densities, five 2D gates were created to gate on the histogram plot of fluorescene intensities vs. # of events. After completing the calibration procedure, the samples were run through the flow cytometer to measure the mean values of fluorescence. Generally, 5,000 events per sample were recorded.

3.3.3 Site density determination

To determine the site densities of samples, the measured fluorescence intensities were compared to standard calibration beads (BD Quantibrite™ PE Beads, BD Biosciences). The recorded five intensities of fluorescence of calibration beads were plotted as a function of numbers of PE fluorofore from BD biosciences. Linear fitting this plot generated the value of the slope, which was used to calculate the numbers of the molecules on samples. The site density was calculated as following equation:

$$\text{Site density} = \frac{\text{Sample's PE intensity}}{\text{Fitted slope} \times \text{Surface area of the sample bead}} \qquad \text{Equation 3-1}$$

3.4 The BFP system

BFP's setup is described in detail in chapter 4. In brief, the instrument of the BFP system was built up on a biological inverted microscope with 40X/0.75 objective lens (Zeiss). The BFP uses swollen biotinylated human RBC as a force sensor. A probe bead coated with streptavidin and ligand proteins was bonded onto the apex of the aspirated RBC by a micromanipulator. The adhesion force was determined by the deformation and the spring constant of RBC. The deformation of the RBC was from the axial movement of the probe bead tracked by a high-speed camera (SensiCam, Cooke). The spring constant of the BFP was estimated by Evans' spring constant model. Basically, this spring constant was dependent on radius of the probe pipette, the RBC and the contact area between probe bead and the RBC. The target bead or cell was aspirated on the target pipette. This target pipette's the steady and accurate movement was driven by a PZT

controlled by a computer.

3.4 Measurement of binding frequency

To measure binding frequency, the target bead or cell were driven by the PZT to touch the probe bead and then retract away. Upon retraction, an adhesion was detected mechanically by the observation of the rupture force events. This contact-retraction cycle was repeated 100 times to generate a random sequence of binary adhesion scores (1 for adhesion and 0 for no adhesion). An adhesion frequency was calculated from the sum of the adhesion scores divided by the number of repeated tests in a series. Usually these binding frequency measurements were repeated on 3-5 pairs of probe beads and target beads/cells to obtain the average adhesion frequency.

3.5 Measurement of bond lifetimes

The dissociation kinetics of receptor and ligand interactions were characterized by measuring the bond lifetime under a given force using the BFP. A lifetime experiment consisted of the following steps. A receptor coated bead or a receptor expressed cell aspirated by the target pipette was brought to approach to and then contact with ligand coated probe bead by the program-controlled PZT. The impingement of the BFP signified the contact. The compressive force and contact duration were controlled by software program. At the end of the contact duration, the PZT retracted target bead or cell away from the probe bead by a fixed distance. An axial deformation of the RBC toward the target pipette signified an adhesion. This deformation was detected by the

high speed camera. In the presence of an adhesion, the fixed distance imparted a constant mean force on the bond. While in the absence of an adhesion, this fixed distance did not generate a binding force on the molecular bond. Since the thermal fluctuation of the BFP (±1-2pN), the mean force was determined from the difference between the two mean positions of the edge between the RBC and the probe bead (Figure 3-1). The bond lifetime measurement was recorded from the moment the PZT retraction stopped until the target bead or cell dissociated from the probe. This cycle was repeated many times to obtain a collection of adhesion lifetimes. The holding force was varied over a range to forces. At each force, multiple measurements were made to generate a collection of lifetimes.

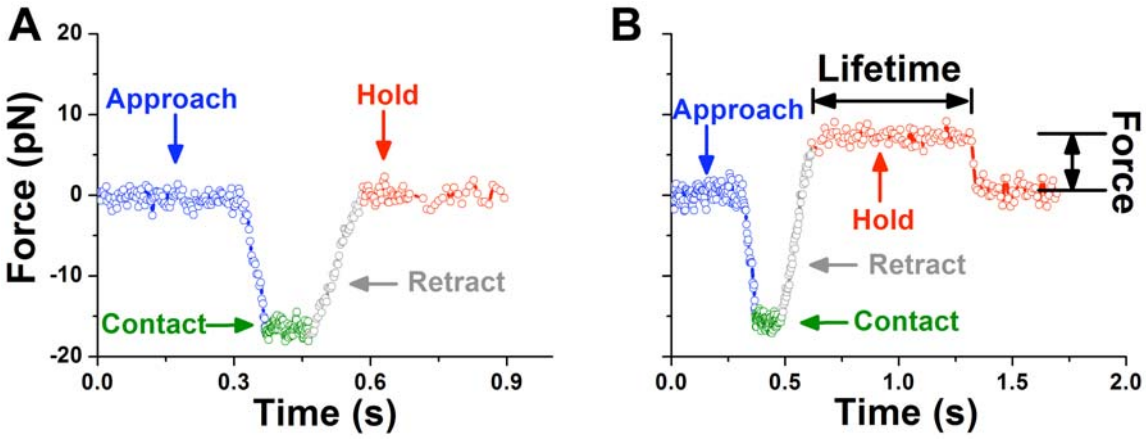

Figure 3-1. Plots of raw BFP lifetime data. (A) Plot of force vs. time in the absence of force. (B) Plot of force vs. time in the presence of force.

CHAPTER 4

INSTRUMENTATION AND CHARACTERIZATION OF THE BFP

4.1 Instruction

The BFP, an extremely smart invention for single molecule study, was originally invented by Evans *et al.* in 1995[61]. Compared to other advanced techniques (AFM, OT) of sensing forces at single molecule level, the BFP is very unique as it uses a red blood cell aspirated by micropipette as a very soft force sensor. This soft spring enables itself to probe very weak biomolecular interactions at the pico-newton (pN,10^{-12} Newton) level. It can also be adjusted from 0.1pN/nm~1pN/nm so that the BFP can probe very wide range of force from 1pN to 1000pN as well as very wide range of force loading rates from 10 pN/s to 10^4 pN/s. These two force-related features are very useful to study various receptor-ligand interactions, for example, to probe their chemical energy landscapes [46]. Moreover, with its very soft spring, we can utilize BFP's thermal fluctuation to study molecular association and dissociation and to measure the kinetic parameters. As the amplitude of the fluctuation reduces very more than stiffer sensor, such as AFM, the BFP is more suitable to detect molecular bond formation. Based on this idea, a thermal fluctuation assay was developed and was discussed in detail in the next chapter. the BFP could be utilized directly study the membrane proteins that are directly expressed on cells, for instance, Evans *et al.* used it to directly study the membrane tether

formation and interactions between cytoplasmic domains of membrane proteins and adaptor proteins or cytoskeleton [60].

4.2 The BFP System

With very kind and important technical support and help from Dr.Evans and his lab members (Andrew Leung, Dr.Koji Kinoshita), we duplicated a latest version of the BFP in Dr.Evans' lab in a short time. The BFP consisted of hardware system (optical, mechanical and electrical components) and a software system developed with Labview. The optical system was mainly to magnify the sample by ~200X. The mechanical hardware system was to steadily hold the micropipette on the microscope, manually and coarsely adjust the micropipettes' positions, and, most importantly, isolate vibration from the environment. The electrical system was the most important part of the BFP. It consisted of one high speed camera for tracking probe bead's movement, one normal speed camera for measuring required dimensions, four PZTs and their controllers, and a fast computer that run control program. Software program mainly analyzed the grabbed images from the high speed camera to generate, store and analyze the data, and feedback control the PZT movement. Each system was described in detail in the following parts.

4.2.2 The hardware system of the BFP

BFP's hardware system was the key component, as it needed to provide a stable but convenient stage to run the force measurement experiment at single molecular level. Hardware system consisted of optical, mechanical and electrical components (Figure 4-1). Optical components were comprised of an inverted biological microscope (Zeiss Axiovert

100) with 40X/NA0.75 objective lens and a condenser with a top lens, the maximum numerical aperture of which is 0.8. Two video tubes were used to mount high speed camera and normal speed camera onto the camera ports on the microscope and provided 4X magnifications. The magnifications of these two video tubes were from the combination of a 0.25X tube lens with 16X eyepieces. The light source was a mercury lamp, which provided abundant light for high speed camera's grabbing. Due to the dynamic range limitations on both cameras, different neutral density filters were placed on the light path from the lamp to the camera to reduce the brightness. To reduce chromatic abbreviation of RBC, a band pass filter (560nm±20nm) only allowing green light to pass through was mounted on the top of the condenser.

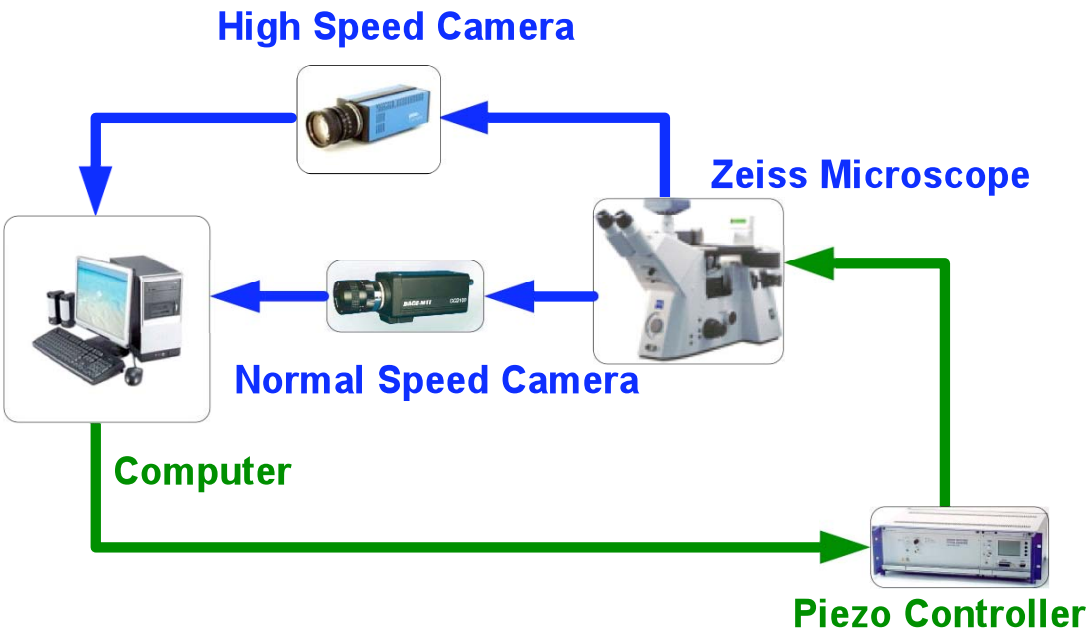

Figure 4-1. Schematic of the BFP system.

The mechanical system included several components: 1) a optical table supporting

the whole microscope and isolating the mechanical vibrations from the environment; 2) two 3D X-Y-Z mechanical stages (Newport and PI) holding and positioning micropipettes, the 3D stage on the probe side only use micrometers to position the micropipette coarsely, but the other one could adjust the target pipette's positions finely with three PZTs of nanometer precision; 3) a one dimension freedom PZT stage (PI) with capacitive feedback control and sub nanometer precision, driving the target pipette to move along the axial direction; 4) pneumatic micromanipulator with a pneumatic joystick to position the probe bead onto the apex of the red cell; 5) customized microscope steel stage with a chamber holder, built with steal so that this stage was heavy enough to reduce the vibration transmission to the chamber in which the BFP experiment runs; 6) customized manometer to control the aspirating pressure on the three micropipettes, and the one controlling the probe pipette had a pressure sensor to accurately measure and indicated the pressure difference for correctly determining the RBC's spring constant.

The electrical system consisted of an imaging grabbing module and a PZT control module. The imaging grabbing module was composed of a high-speed camera (~1500 fps, Sensicam, or ~1800 fps, Procilica) for tracking the deflection of RBC and a normal speed camera (~30 fps, Dage MTI) for measuring the dimension and monitoring the experiments process. Both cameras' images were grabbed by framegrabbers installed in a PC. The frame grabber for the high-speed camera was much more powerful than the one for the normal-speed camera, since it had to handle much large amount of image data. The PZT control module included a PZT stages, a PZT controller and a wave-board installed in the PC. The wave-board output signals and transferred to the PZT controller.

The PZT controller amplified the signal and output voltage signals (0-100V) to control the PZT's steady movement.

4.2.3 The software system of the BFP

The software system for the BFP consisted of an imaging grabbing module, an imaging analysis module, a PZT control module and a data analysis module. The imaging grabbing module mainly handled grabbing images from the high speed camera and pre-processed grabbed images for following imaging analysis. The imaging analysis program was used to analyze the grabbed images and to extract the position information of the edge between the probe beads and RBC as shown in (Figure 4-2A, indicated by yellow arrow). To speed up the process of the image analysis and increased the frame rates, only center 27 lines of the whole view field were analyzed by binning into one line (Figure 4-2A, bright area), other lines of images were completely block out by a slit (Figure 4-2A, dark area). The new model of the high speed camera, using CMOS chip, could directly readout the images from the region of interest without a blocking slit. To obtain the edge position, the binned grey line, the intensity profile of which is shown in Figure 4-2B, was fit by Gaussian distribution. The peak of fitting curve (orange dot in Figure 4-2B) provided the position of the edge.

To determine the spring constant of the BFP, the radius of probe pipette, RBC and contact area were measured by the software program customizedly written by Labview 8.5. The tracking data were stored in the hard disk during the experiment. Next, all the stored data were analyzed by the data analysis program that is customizedly written with Labview 8.5.

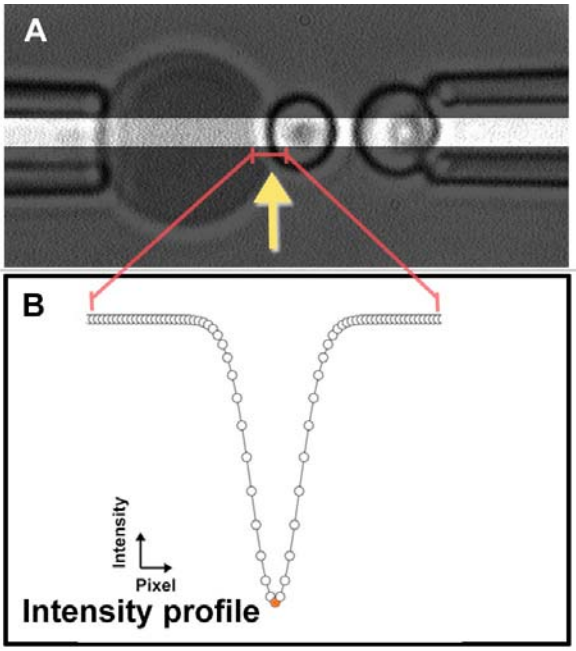

Figure 4-2. Imaging tracking region and intensity profile for the BFP. (A) Image analysis region, the bright area, for tracking system, the dark area was blocked out not for analyzing. The tracking edge is indicated by the yellow arrow. (B) Intensity profile of the bead's edge in (A). The region in (B) corresponds to a smaller region in (A) which is indicated by a red marker. The orange point in (B) is the peak of Gaussian distribution fitting to the profile.

4.3 Characterization of the BFP

4.3.1 Characterize spatial precision of the tracking system of the BFP

Since our BFP was custom-designed by Dr. Evan Evans, who helped us assemble it in our laboratory, we characterized of our new BFP apparatus here. To determine the spatial precision of our BFP, we compared the displacements of the target bead tracked by the image tracking system (Figure 4-3A, red circles, left ordinate) with the displacements of the PZT that drove the right pipette on which the target bead was aspirated (Figure 4-3A, green squares, left ordinate). The PZT used an integrated capacitive feedback control to achieve sub-nanometer spatial precision and was programmed to travel back

and forth in a quasi-rectangular waveform. It is evident that the tracked displacements followed the programmed displacements very well (Figure 4-3A). The differences between the two (Figure 4-3A, blue triangles, right ordinate) were analyzed by histogram (Figure 4-3B), which follows a Gaussian distribution with a standard deviation of ~3 nm. This analysis establishes that the spatial precision of our image tracking system is ±3 nm.

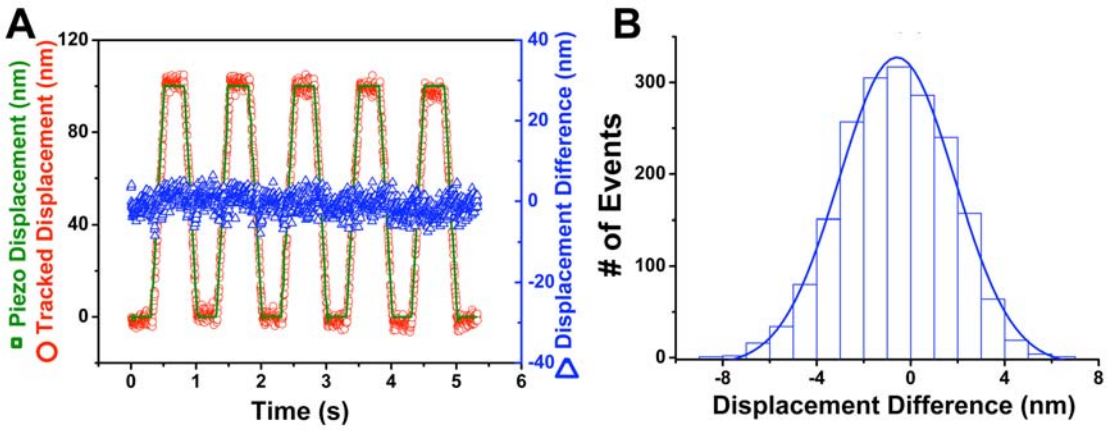

Figure 4-3. Characterization of the tracking precision of the BFP. (A) Comparison of the piezo displacements (green, □) and the tracked displacements (red, ○). The differences between them are shown as blue (Δ)). (B) Histogram (bars) of the differences between the piezo and tracked displacements. It is fitted by a Gaussian distribution (curve).

4.3.2 Motion-blur correction on the thermal fluctuation of the BFP

The BFP (Figure 4-2A) uses a pressurized RBC as an ultrasensitive force transducer. The 3-nm spatial precision of the BFP's image tracking system can be translated to sub-piconewton force sensitivity by multiplying the axial deflection of the RBC force transducer by its "spring constant", k_p. Several approximate expressions for k_p have been derived based on membrane mechanics, for example, the equation by Evans et al.[60]

reads

$$k_p \approx \frac{\pi R_p \Delta p}{(1 - R_p / R_0)\ln\left[4R_0^2 / (R_p R_c)\right]}, \qquad \text{Equation 4-1}$$

where Δp is the suction pressure and R_p, R_0, and R_c are the respective radii of the pipette lumen, the spherical portion of the aspirated RBC, and the adhesive contact between the RBC and the probe bead (cf. Figure 4-2A).

Calibration of the BFP spring constant can be done using thermal fluctuation analysis, which is based on the equipartition theorem,

$$\frac{1}{2} k_p \,\mathrm{var}(X) = \frac{1}{2} k_B T, \qquad \text{Equation 4-2}$$

where var(X) is the variance of the thermally-excited random displacements X of the force probe, k_B is the Boltzmann constant and T is the absolute temperature. Figure 4-4 compares the time courses of displacements of the target bead (Figure 4-4*A*), the probe bead (Figure 4-4*B*), and the left pipette mouth on which the RBC was mounted (Figure 4-4*C*) while the two pipettes were held stationary. It is evident that the force probe displacements exhibit significantly larger fluctuations than those of the other two sites, indicating that the large fluctuations are caused by thermal excitation of the force probe confined by a very soft spring.

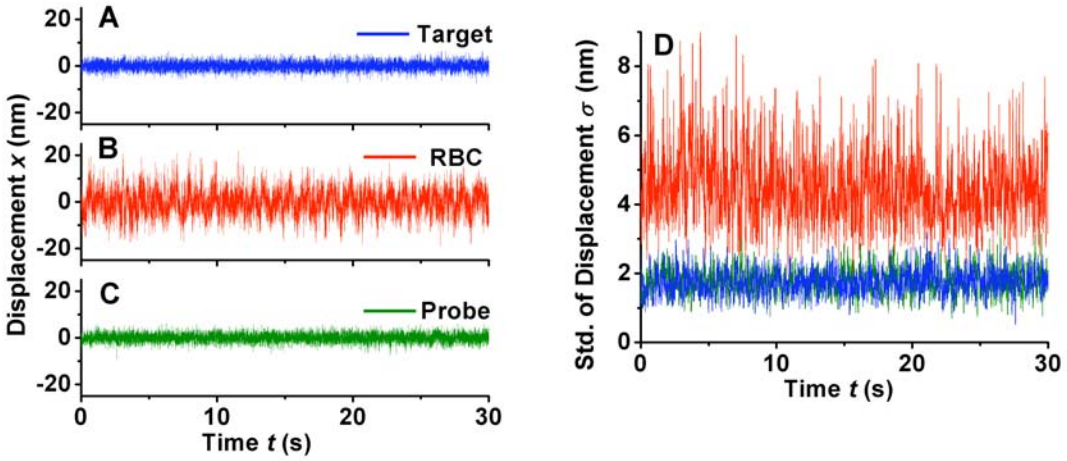

Figure 4-4. Illustrations of thermal fluctuations. Tracked displacements of the target pipette (A), the force probe (B) and the probe pipette (C) over time during which both pipettes were held stationary. (D) Comparison of the 15-point sliding standard deviations of the fluctuating displacements in A-C (color-matched).

Due to the finite temporal resolution (limited by the camera speed), the measured displacements X_m are an average of X over the time window during which a single frame of image is acquired. This causes a so-called "motion-blur" effect, as discussed by Wong et al.[79] and references therein, that reduces the measured variance var(X_m) from var(X) by a factor of $S(\alpha)$, i.e.,

$$\mathrm{var}(X) = \mathrm{var}(X_m) S^{-1}(\alpha). \qquad \text{Equation 4-3}$$

$S(\alpha)$ is the motion-blur correction function,[79]

$$S(a) = \frac{2}{\alpha} - \frac{2}{\alpha^2}\left[1 - \exp(-\alpha)\right], \qquad \text{Equation 4-4}$$

where a is the ratio of the camera exposure time to the characteristic fluctuation time of the BFP, represented by the ratio of its spring constant to its friction coefficient. Thus, $\alpha = Ak_p$ where A is proportional to the camera exposure time but inversely proportional to the BFP friction coefficient. Since $k_p = C\Delta p$ from Equation 4-1, it follows from

substituting Equations 4-2 and 4-4 into Equation 4-3 that

$$\mathrm{var}(X_m) = \frac{k_B T}{C\Delta p}\left\{\frac{2}{AC\Delta p} - \frac{2}{(AC\Delta p)^2}\left[1 - \exp(-AC\Delta p)\right]\right\} \qquad \text{Equation 4-5}$$

To correct for low frequency drifts, we calculated a series of var(X_m) values after passing the displacement data through a series high-pass filters and extrapolated the "drift-free" variance from the var(X_m) vs. filter frequency plot[79].

Two sets of drift-free var(X_m) were plotted vs. $1/\Delta p$, one measured in hypotonic condition (Figure 4-5*A*) and the other in isotonic condition (Figure 4-5*B*). As expected, the var(X_m) of the force probe increased as the suction pressure decreased. By comparison, the control var(X_m) measured from the target bead and the left pipette mouth did not response to the changes of the suction pressure and was very small (< 2 nm^2), indicating a very low noise level of our system. Equation 4-5 was nonlinearly fit to the background-subtracted var(X_m) vs. $1/\Delta p$ data, which returns two parameters, A and C. This allows for calculation of the corrected var(X) from var(X_m) using Equations 4-3 and 4-4 with $\alpha = AC\Delta p$, which is plotted vs. $1/k_p$ calculated from Equation 4-1 for hypotonic (Figure 4-5*C*) and isotonic (Figure 4-5*D*) conditions. Both data sets display a linear trend, as predicted by Equation 4-2. The linear fit to the data in Figure 4-5*C* has a slope of 4.0 pN-nm, in excellent agreement with the $k_B T$ value at room temperature, supporting the validity of Equation 4-1 in the hypotonic condition. By comparison, fitting the data in Figure 4-5*D* with a straight line returns a slope of 2.5 pN-nm, significantly smaller than the 4.1 pN-nm value predicted by the equipartition theorem, suggesting that Equation 4-1 is not valid in the isotonic condition. The assumptions underlying the analysis that yield Equation 4-1 are reasonable when the RBC is swelled in hypotonic medium and forms a

sphere after being aspirated by a pipette of 2-3 μm inner diameter to form a short cell tongue inside the pipette (cf. Figure 4-2A). These assumptions break down when isotonic medium is used. RBCs have a biconcave discoid shape in isotonic medium. To form a sphere from part of the cell requires the use of a smaller pipette to aspirate the rest of the cell into the pipette to form a much longer cell tongue, which greatly increases the friction between the pipette wall and the cell membrane, invalidating the frictionless assumption required for the analysis. Nevertheless, we should still be able to directly use the value C obtained by fitting Equation 4-5 to Figure 4-5*B* to calculate $k_p = C\Delta p$ for the spring constant for a BFP in the isotonic condition.

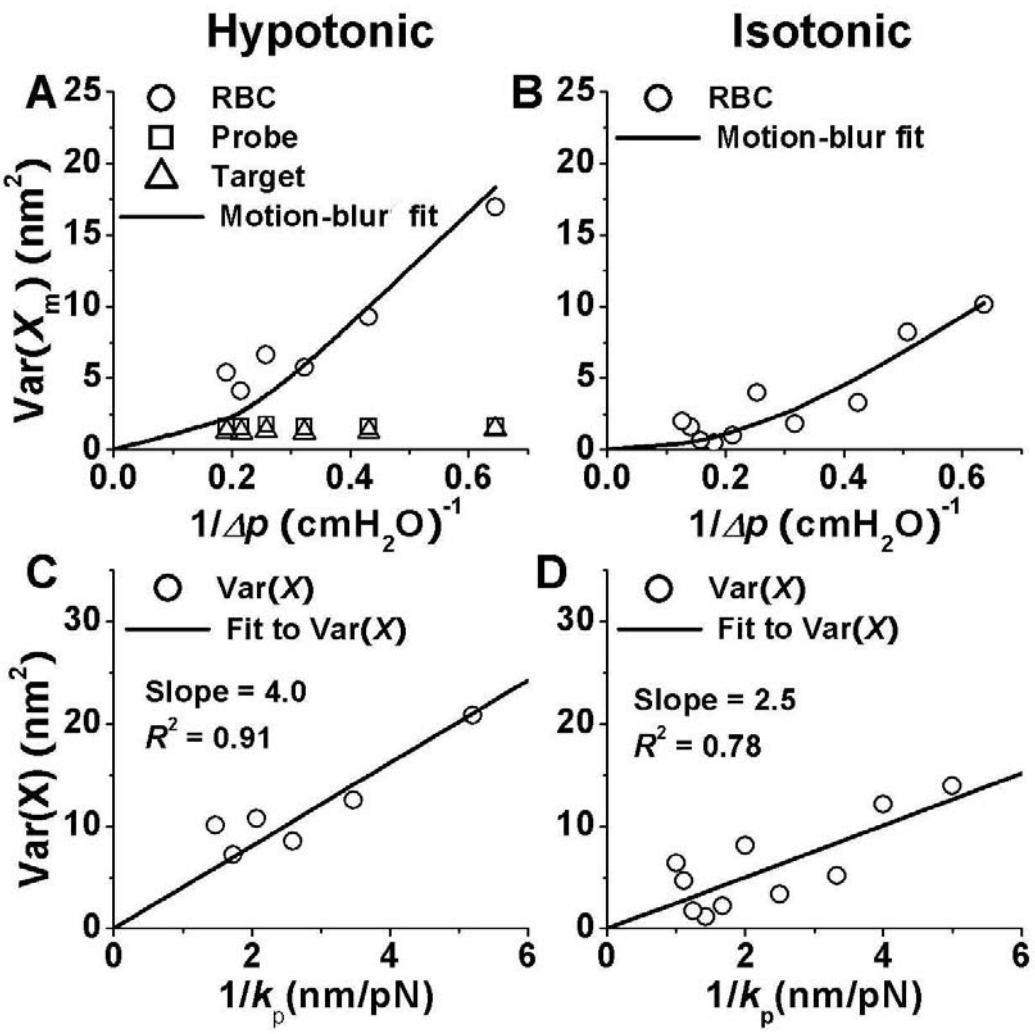

Figure 4-5. Calibration of the BFP spring constant. (A and B) The background-subtracted drift-free variance var(Xm) of a BFP force probe (○) is plotted vs. reciprocal suction pressure 1/*p* under which the fluctuating displacements were measured in hypotonic (A) or isotonic (B) condition (contributed by Dr.Veronika in Dr.Zhu's lab) and fitted by motion-blur model Eq. 11 (curve). The variances of the target bead (D) and the probe pipette (□) are also plotted in A, which serve as the background. (C and D) The motion-blur corrected variance var(*X*) (○) is plotted vs. 1/*k*p calculated from Equation 4-5 using parameters from the experiments under which the fluctuating displacements were measured in hypotonic (C) or isotonic (D) condition and fitted by a straight linear that passes the origin.

CHAPTER 5

MONITORING RECEPTOR-LIGAND INTERACTIONS BETWEEN SURFACES BY THERMAL FLUCUTATIONS

5.1 Introduction

Cells communicate with their environment via receptors that bind to soluble ligands in the fluid phase (three-dimensional or 3D binding) or to tethered ligands on surfaces of other cells or in the extracellular matrix (two dimensional or 2D binding). 2D binding mediates critically important cell adhesion and signaling events in diverse tissues [80]. The force dependence of 2D dissociation off-rates of receptor-ligand interactions have been studied by several approaches, including lifetime measurements of single bonds or single-cell tethers [47] and rupture force measurements by dynamic force spectroscopic analysis [55]. By comparison, few assays have measured how receptors and ligands associate in two dimensions. Tether rates in a flow chamber measure a lumped parameter that multiples on-rate with collision frequency, encounter duration, and contact time [57, 81]. The adhesion frequency assay extracts kinetic information from the dependence of adhesion frequency on contact time [82]. In the latter case, adhesion is measured mechanically using an ultrasensitive force transducer such as a BFP [61], which detects the presence of a receptor-ligand bond at the end of a contact but not when a bond forms or dissociates. Therefore, kinetics of molecular interaction must be inferred from the

contact time dependence of adhesion frequency [82]. Here, we develop a method that uses decrease/resumption of thermal fluctuations of a BFP to pinpoint association/dissociation events at the single-bond level during the contact period. This greatly enhances the quantity, quality, and reliability of the information obtained, which makes kinetic measurements much simpler and more robust.

As a model system, we study the interactions of L-selectin, expressed on leukocytes, and P-selectin, expressed on activated platelets and endothelial cells, with their common leukocyte ligand, P-selectin glycoprotein ligand-1 (PSGL-1) [83]. These rapidly reversible interactions mediate rolling adhesion of leukocytes on vascular surfaces during inflammation. L- and P-selectin bind to the same N-terminal region of PSGL-1 but with different affinities in 3D assays. Here, we use the thermal fluctuation method to directly compare the 2D association and dissociation rates for interactions of L- and P-selectin with PSGL-1. The formation of an L-selectin-PSGL-1 bond decreases the BFP thermal fluctuations more than a P-selectin-PSGL-1 bond, as predicted by the higher stiffness of L-selectin than P-selectin [84]. The new method can be extended to measure cell adhesion mediated by several receptor-ligand pairs that bind independently or cooperatively, the initiation and termination of cell signaling, and other complex 2D interactions of purified macromolecules or of live cells.

5.2 Results

5.2.1 Change in Thermal Fluctuations Identifies Bond Association or Dissociation

We used BFP to monitor interactions between PSGL-1 coated on the probe glued to the apex of a RBC pressurized by micropipette suction (Figure 5-1A, left) and L-selectin or P-selectin coated on the target aspirated by an apposed micropipette (Figure 5-1A, right). The experimental procedure is illustrated by a representative probe position x vs. time t plot for PSGL-1 interacting with L-selectin (Figure 5-1B) or P-selectin (Figure 5-1C). The target was driven by a computer-programmed piezoelectric translator with capacitive feedback control to approach the probe, which pushed it to a compressive position ($x << 0$) upon contact. The target was retracted by exactly the same distance as it was used to push the probe, thereby allowing the probe to spring back to a null position ($x \approx 0$). The target was then held in that position to allow the probe and the target to contact via thermal fluctuations but not by compression, thereby providing an opportunity for selectin and PSGL-1 to interact. At the end of the holding period the target returned to its starting position, which might (Figure 5-1C) or might not (Figure 5-1B) pull the probe to a tensile position ($x >> 0$), depending on whether a bond(s) was present at that instant. This approach-push-retract-hold-return test cycle was then repeated many times to acquire an ensemble of data for statistical analysis.

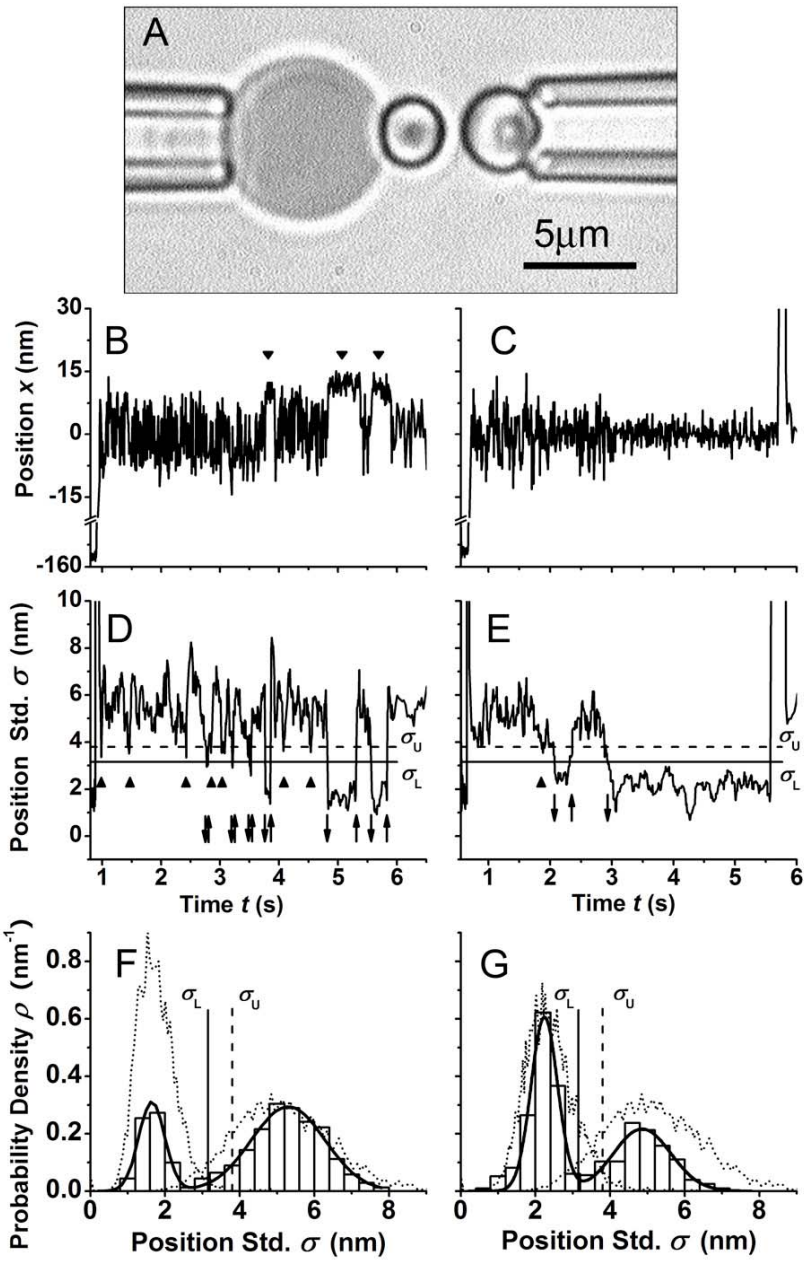

Figure 5-1. Thermal fluctuation method. (A) Photomicrograph of a BFP. (B and C) Horizontal position x of the right edge of the probe is plotted vs. time t for a representative test cycle measuring the interaction between PSGL-1 coated on the probe and L-selectin (B) or P-selectin (C) coated on the target. Two periods of high positions in (B) are indicated by arrowheads. (D and E) Sliding standard deviations σ of 15 consecutive points of the position data in B and C, respectively. (F and G) Histograms of the σ data in D and E (bars), respectively, each fitted by Equation 5-1 (solid curves). Also superimposed on each panel are two histograms of σ values calculated from x(t) data of two unencumbered probes recorded for the same duration of time (dotted curves). One unencumbered probe had the same spring constant of k = 0.15 pN/nm as the

probe used to acquire the data in D and E. The other unencumbered probe had spring constant of k = 1.7 (F) or 0.8 (G) pN/nm. All histograms were normalized to have a unity area. The vertical dashed line σ_U = 3.8 nm on each panel is one standard deviation (1.3 nm) to the left from the peak at 5.1 nm. The vertical solid line σ_L = 3.15 nm on each panel is 1.5 standard deviation to the left from the same peak. These thresholds are marked in D and E as horizontal lines to identify bond association and dissociation events, which are marked by the respective down and up arrows. Arrowheads indicate intervals deemed indeterminate as to whether they corresponded to free or bound probes because data lay between the two thresholds.

The probe position $x(t)$ exhibited significant fluctuations even when neither the probe nor the target was moved by the micropipette (Figure 5-1 B and C). These reflect thermal fluctuations from the ultra soft RBC membrane because the position of the target tracked by the same image analysis software displayed substantially lower fluctuations (data not shown). Three periods in Figure 5-1B can be identified (arrowheads) where the average probe positions appear higher (x ~ 10-12 nm), suggesting that the probe was pulled by a small force (~1-2 pN) due to the presence of an L-selectin-PSGL-1 bond(s). This hypothesis predicts reduced thermal fluctuations in these periods because bond formation is equivalent to adding a molecular spring in parallel to the force transducer spring to stiffen the system [84, 85]. While qualitative evidence for this prediction can be directly observed from Figure 5-1B, quantitative data are shown in Figure 5-1D where the sliding standard deviation σ was plotted vs. time t; σ was calculated from every 15 consecutive points of the position $x(t)$ data in Figure 5-1B to gauge the level of thermal fluctuations. It is evident that the three periods with high average positions correspond to three periods of low standard deviations (Figure 5-1 B and D).

Bond formation is not expected to pull the fluctuating probe to a new equilibrium position closer to the target if the target was retracted to and held at a position so close to the probe that the mean distance between the two surfaces was comparable to the length of a molecular crossbridge [84]. This might be the case in Figure 5-1C, which shows reduced thermal fluctuations but the $x(t)$ data appear to have similar levels as the null position ($x \approx 0$). The corresponding $\sigma(t)$ data are shown in Figure 5-1E, which clearly reveal two periods of reduced thermal fluctuations.

The σ data in Figure 5-1 D and E were analyzed by histograms (Figure 5-1 F and G, *bars*) to see if the reduced BFP thermal fluctuations caused by the formation of putative bonds could be separated from those expected from an unencumbered BFP. Only σ data from 1.0-6.0 s were included because the low σ values from 0.8-0.9 s (Figure 5-1D) or 0.6-0.7 s (Figure 5-1E) corresponded to the time when the target was impinged against the probe, which suppressed the thermal fluctuations (Figure 5-1 D and E). Data from 5.5-6.0 s in Figure 5-1E were also excluded because they corresponded to the time when the probe was pulled by the target, which produced nonrandom long-distance travels and resulted in artificially large σ values. It is evident that the σ values are clustered into two subpopulations in the histograms, which were well fitted by the following dual Gaussian distributions (Figure 5-1 F and G, solid curves):

$$\rho(\sigma) = \frac{A_1}{\sqrt{2\pi}\Delta\sigma_1}\exp\left[-\frac{(\sigma-\overline{\sigma}_1)^2}{2(\Delta\sigma_1)^2}\right] + \frac{A_2}{\sqrt{2\pi}\Delta\sigma_2}\exp\left[-\frac{(\sigma-\overline{\sigma}_2)^2}{2(\Delta\sigma_2)^2}\right] \qquad \text{Equation 5-1}$$

where $\overline{\sigma}_i$ (1.6 or 5.3 nm in Figure 5-1F and 2.2 or 5.0 nm in Figure 5-1G, for i = 1 or 2) and $\Delta\sigma_i$ (0.35 or 0.99 nm in Figure 5-1F and 0.35 or 0.0.77 nm in Figure 5-1G, for i = 1 or 2) denote the mean and standard deviation of the ith Gaussian distribution. A_i (0.27 or

0.73 in Figure 5-1F and 0.54 or 0.42 in Figure 5-1G, for i = 1 or 2) is the area under the ith Gaussian distribution curve; $A_1 + A_2 = 1$ as required by normalization.

To identify the origins of the two subpopulations in the histograms, we superimposed two histograms of σ values on each panel of Figure 5-1 F and G (dotted curves), which were calculated from $x(t)$ data of two unencumbered probes recorded for the same duration of time. These were used as calibration for the BFP spring constant k according to the equipartition theorem, $0.5k\langle\sigma^2\rangle = 0.5k_BT$, where $\langle\sigma^2\rangle$ is average of σ^2 over the entire population, k_B is the Boltzmann constant, and T is the absolute temperature. One unencumbered probe had the same spring constant of k = 0.15 pN/nm as the probe used to acquire the data in Figure 5-1 D and E; the histogram of its σ values matched that of the subpopulation peaked at $\bar{\sigma}_2$ = 5.3 (Figure 5-1F) or 5.0 (Figure 5-1G) nm, indicating that the right subpopulation corresponded to periods when the probe was free. The spring constant of the other unencumbered probe was tuned to k = 1.7 (Figure 5-1F) or 0.8 (Figure 5-1G) pN/nm in order to generate a histogram to match that of the subpopulation peaked at $\bar{\sigma}_1$ = 1.6 (Figure 5-1F) or 2.2 (Figure 5-1G) nm, indicating that the left subpopulation corresponded to periods when L-selectin (Figure 5-1F) or P-selectin (Figure 5-1G) on the probe was bound to PSGL-1 on the target.

The two subpopulations in the histograms in Figure 5-1 F and G overlap. To assign a given data point to a particular subpopulation, we chose σ_U = 3.8 nm, one standard deviation (1.3 nm) to the left from the peak at 5.1 nm, as the upper threshold above which data were considered to correspond to a free probe (Figure 5-1 F and G, vertical dashed lines) and σ_L = 3.15 nm, 1.5 standard deviation to the left from the same

peak, as the lower threshold below which data were considered to correspond to a bound probe (Figure 5-1 F and G, vertical solid lines). These thresholds are also marked in Figure 5-1 D and E as horizontal lines to identify bond association (when the data curve runs downward across the solid line) and dissociation (when the data curve runs upward across the dashed line) events, which are marked by the respective down and up arrows. Arrowheads indicate intervals deemed indeterminate as to whether they correspond to a free or bound probe because data lie between the two thresholds.

The threshold method identified two intervals in Figure 5-1E where a bond was present despite the fact that no mean force was detected by the BFP (Figure 5-1C). The suggested presence of a bond immediately prior to the end of the holding phase was confirmed by the pulling of the probe upon the target return (Figure 5-1C). Likewise, in Figure 5-1D the σ values were above the upper threshold prior to the target return indicating the absence of any bond, which was confirmed by the fact that no pulling was observed upon the target return (Figure 5-1B).

The validity of using reduction/resumption in σ as an identifier for bond association/dissociation event (thermal fluctuation method) was tested by examining the correlation of (or the lack thereof) its results with those determined by an independent method: the presence or absence of probe pulling during the target return (pulling method). A total of 812 tests like those in Figure 5-1 D and E were analyzed. Of these, 87 were discarded because their σ values immediately prior to the target return were in between the upper and lower thresholds. Remarkably, a very strong correlation was found: in >96% of the remaining 725 tests the thermal fluctuation method reported correctly for either having (159 tests) or not having (541 tests) a bond as confirmed by

the pulling method (Figure 5-2). Only 13 tests were scored as having a bond by the thermal fluctuation method but not confirmed by the pulling method (false positive) and only 12 tests were scored as not having a bond by the thermal fluctuation method but shown to have a bond by the pulling method (false negative) (Figure 5-2), which would give rise to a <3.5% error. These might be bond association/dissociation events that occurred at the beginning of the target return, which might have been missed due to insufficient temporal resolution of the thermal fluctuation method. These data demonstrate the reliability of using the reduced thermal fluctuations to report the presence of bonds.

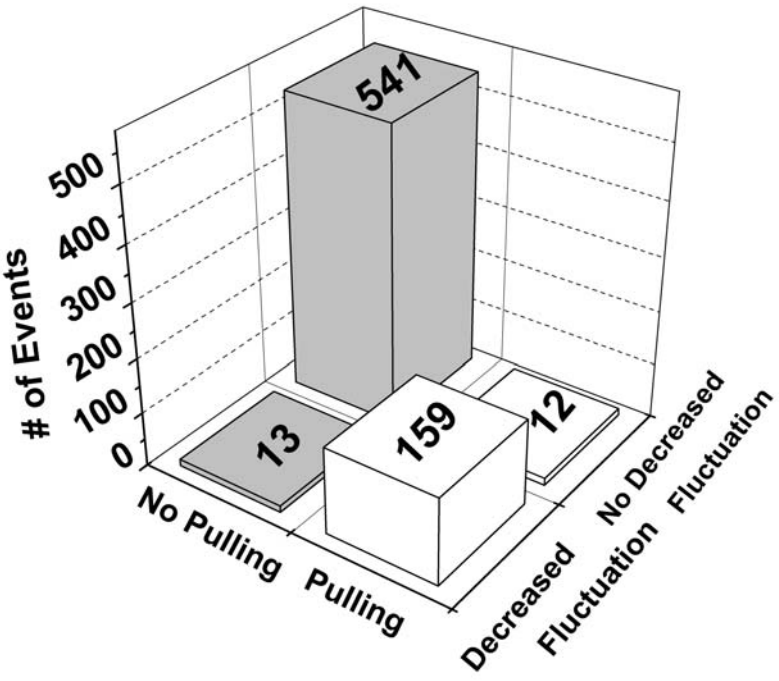

Figure 5-2. Comparison between two methods for determining the presence of a bond. A total of 812 tests like those in Figure 5-1D for L-selectin-PSGL-1 interactions were segregated into two groups. The first group of 87 tests had σ values immediately prior to the target return that were between the upper threshold σ_U = 3.8 nm and the lower threshold σ_L = 3.15 nm, which were deemed as indeterminate and excluded. The second group of 725 tests were further

segregated into four subgroups depending on whether they had σ values immediately prior to the target return above the upper threshold (no decreased fluctuation) or below the lower threshold (decreased fluctuation) and whether the returning target produced pulling or no pulling of the probe. The number of tests in each subgroup was plotted against the four conditions marked on the *x*-*y* plane (and also indicated on the top of each bar).

5.2.2 Measuring 2D Kinetic Rates of Receptor-ligand Interactions

Many applications can be envisioned for our thermal fluctuation method for identifying bond formation/dissociation events in two dimensions. To exemplify this, we next demonstrate the application of this method to measurement of 2D binding kinetics of receptor-ligand interactions. To do that, we realized that the period from the instant of dissociation of an existing bond to the instant of association of the next bond, termed waiting time t_w, contains on-rate (k_{on}) information because the faster the on-rate, the shorter the expected waiting time. It should also depend on the site densities of receptors (m_r) and ligands (m_l), because the higher the density, the greater the chance for receptors to find ligands, and the shorter the expected waiting time. Waiting times were measured from a large number of test cycles, pooled, and analyzed by a model for the first-order kinetics of irreversible association of single bonds [57]:

$$P_a = 1 - \exp(-m_r m_l A_c k_{on} t_w) \qquad \text{Equation 5-2}$$

where A_c is the contact area and P_a is the probability for forming a bond before t_w. Taking the natural log of $(1 - P_a)$ linearizes the exponential waiting time distribution given by Equation 5-2, a prediction supported by data in Figure 5-3*A*, which align quite well along a straight line. This indicates that intervals from an abrupt resumption to the next abrupt reduction in thermal fluctuations indeed distribute as waiting times for single

bond formation. It follows from Equation 5-2 that the negative slope of the ln(# of events with a waiting time ≥ t_w) vs. t_w plot equals $m_r m_l A_c k_{on}$, which can be thought of as a cellular on-rate [57].

Similarly, we realized that the period from the instant of bond association to the instant of bond dissociation, termed bond lifetime t_b, contains off-rate (k_{off}) information because the faster the off-rate, the shorter the expected bond lifetime. Bond lifetimes were measured using data collected from the same test cycles as those used to obtain waiting times, pooled, and analyzed by a model for the first-order kinetics of irreversible dissociation of single bonds [47]:

$$P_b = \exp(-k_{off} t_b) \qquad \text{Equation 5-3}$$

where P_b is the probability for a bond formed at time 0 to remain bound at time t_b. Taking the natural log of P_b linearizes the exponential bond lifetime distribution given by Equation 5-3, a prediction supported by data in Figure 5-3*B*, which align quite well along a straight line. This indicates that intervals between an abrupt reduction and an abrupt resumption in thermal fluctuations indeed distribute as single bond lifetimes. It follows from Equation 5-2 that k_{off} can be estimated from the negative slope of the ln(# of events with a lifetime ≥ t_b) vs. t_b plot [47].

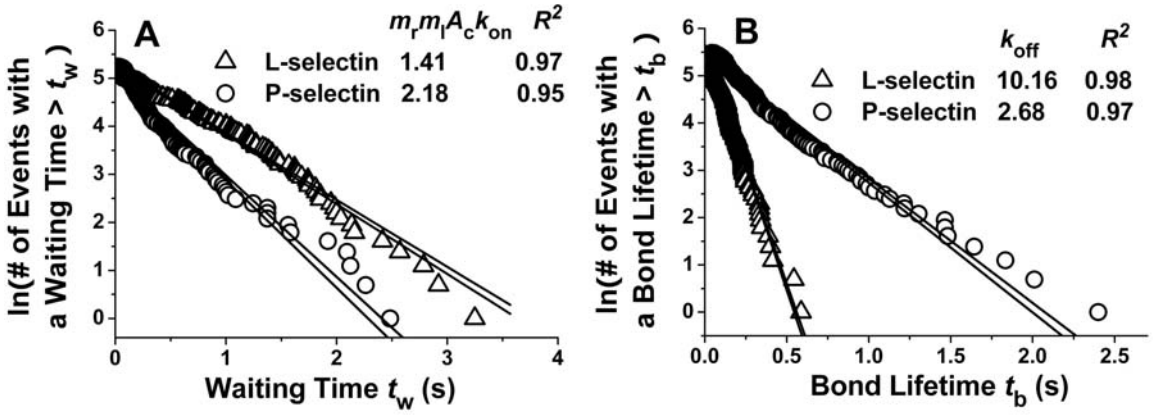

Figure 5-3. Exponential distributions of waiting times (A) and bond lifetimes (B). Pooled ensembles of 156 (L-selectin) or 190 (P-selectin) waiting times (A), defined as intervals from a dissociation event to the next association event, and 172 (L-selectin) or 240 (P-selectin) bond lifetimes (B), defined as intervals from an association event to the next dissociation event, of PSGL-1 respectively interacting with L-selectin (Δ) or P-selectin (○) were respectively sorted according to their durations. The natural log of the number of events with waiting times > t_w (A) or bond lifetimes > t_b (B) was respectively plotted against t_w or t_b, respectively, and respectively fitted by a straight line (not shown). The negative slopes of the best-fits represent cellular on-rate $m_r m_l A_c k_{on}$ and off-rate k_{off}, respectively, whose values are indicated. The variations in these values are shown by the 95% confident intervals of the best-fit (lines). The goodness-of-fit was measured by the R^2 values, which are also indicated.

If the negative slopes of the linear fits to the data in Figure 3 A and B indeed represent respective cellular on-rates and off-rates, then the former should increase linearly with, and the latter should be independent of, the site densities of the receptors and ligands, provided that the observed events reflect predominately single bonds. To test this prediction, we measured the 2D kinetics of L-selectin-PSGL-1 interaction using four different site densities. The cellular on-rate constant, $m_r m_l A_c k_{on}$, was found to be proportional to the site densities of L-selectin and PSGL-1 (Figure 5-4*A*), as expected

from the 2nd order forward reaction (Equation 5-2), supporting our prediction. The slope of the linear fit to the data is the effective average on-rate, $\langle A_c k_{on} \rangle = 5.9 \times 10^{-5}$ $\mu m^4 s^{-1}$. By comparison, the off-rate constant was found to be independent of the site densities (Figure 5-4*B*), as expected from Equation 5-3, again supporting our prediction. The mean off-rate is $\langle k_{off} \rangle = 10.2$ s^{-1}.

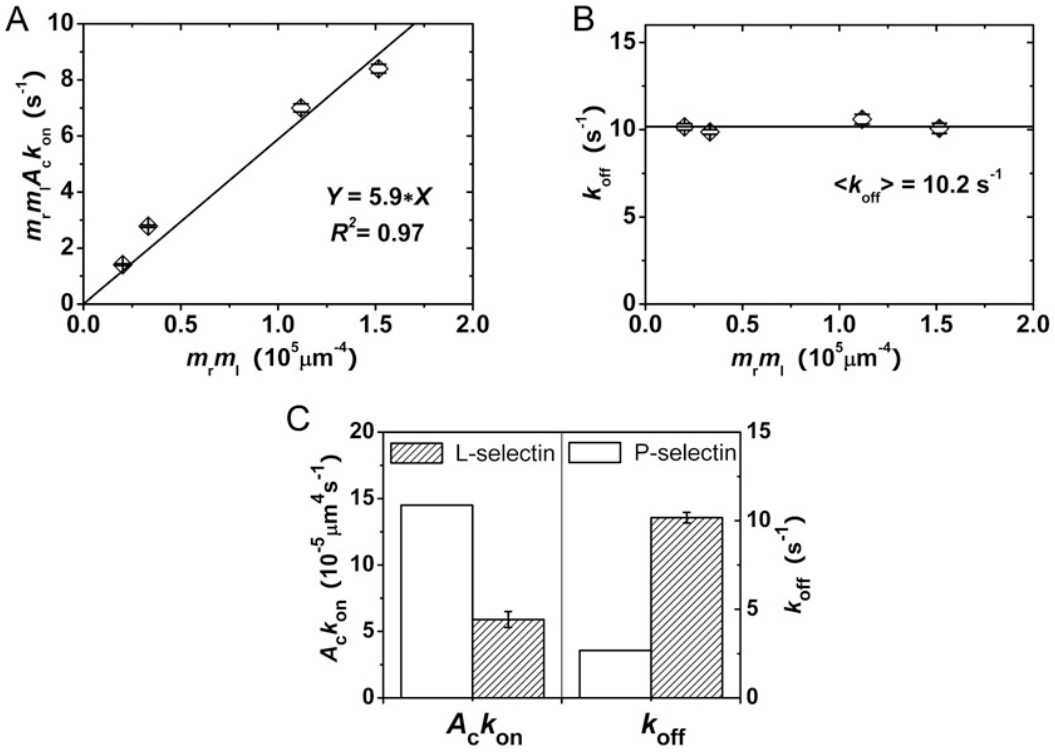

Figure 5-4. Kinetic parameters. Cellular on-rate (A) and off-rate (B) were plotted vs. product of the site densities of the interacting molecules, L-selectin and PSGL-1. Data (points, error bar = 95% confident interval) were respectively fitted by a straight line that passed the origin (A) to estimate a molecular 2D effective on-rate $\langle A_c k_{on} \rangle$ (best-fit equation and R^2 were indicated) or by a horizontal line (B) to estimate the average off-rate $\langle k_{off} \rangle$ (indicated). (C) Comparison of kinetic rates of PSGL-1 interacting with L-selectin and P-selectin.

If the negative slopes of the linear fits to the data in Figure 5-3 A and B indeed represent respective cellular on-rates and off-rates, then they should depend on the molecular interaction tested. To test this prediction, we measured 2D kinetics of two molecular interactions: L- and P-selectin respectively interacting with PSGL-1 at comparable site densities. Distributions of waiting times and lifetimes of these two interactions are compared in Figure 5-3, which clearly show that PSGL-1 has a faster on-rate, but a slower off-rate, with P-selectin than L-selectin. Previous surface plasmon resonance experiments show that P-selectin binds PSGL-1 with higher 3D affinity and slower off-rate than binding of L-selectin to glycosylation-dependent cell-adhesion molecule-1 [86, 87], not withstanding the fact that this technique did not have sufficient temporal resolution to accurately determine the fast off-rate of L-selectin [86, 87]. Figure 5-4*C* represents the first quantitative evidence that P-selectin has a higher 2D on-rate than L-selectin for the same ligand.

5.2.3 Comparison between the thermal assay and the adhesion frequency assay

To further validate the thermal fluctuation method, we compared the 2D kinetic rates measured by this method with those measured by the adhesion frequency assay [82], which has been extensively used to determine many receptor-ligand interactions. In the adhesion frequency assay, binding is determined mechanically by separating the two surfaces like the pulling method (Figure 5-1 B and C). The

presence of a molecular bond is detected using an ultrasensitive picoforce transducer, such as a pressurized RBC or a BFP, because the interaction force will resist surface separation until the bond ruptures. Rather than measuring rupture forces, the adhesion frequency assay estimates the likelihood of adhesion, or adhesion probability, P_a, from the frequency of adhesion enumerated from a large number of repeated controlled contacts. P_a is related to the contact time t_c through a probabilistic model [82]:

$$P_a = 1 - \exp\{-m_r m_l A_c k_{on}[1 - \exp(-k_{off} t_c)]/k_{off}\} \qquad \text{Equation 5-4}$$

Using the same BFP, same reagents, same site densities, and experiments prepared the same way as those in the thermal fluctuation method, we measured adhesion frequencies in a range of contact durations for both L-selectin and P-selectin interacting with PSGL-1. The P_a vs. t_c data (points) are shown in Figure 5-5. Also shown are predictions of Equation 5-4 (curves) using the values of $A_c k_{on}$ and k_{off} estimated previously from the thermal fluctuation method (Figure 5-4*C*) and the known site densities m_r and m_l. It is evident that the predictions agree with the data reasonably well for both the L-selectin and P-selectin cases (Figure 5-5), further supporting the validity of the thermal fluctuation method.

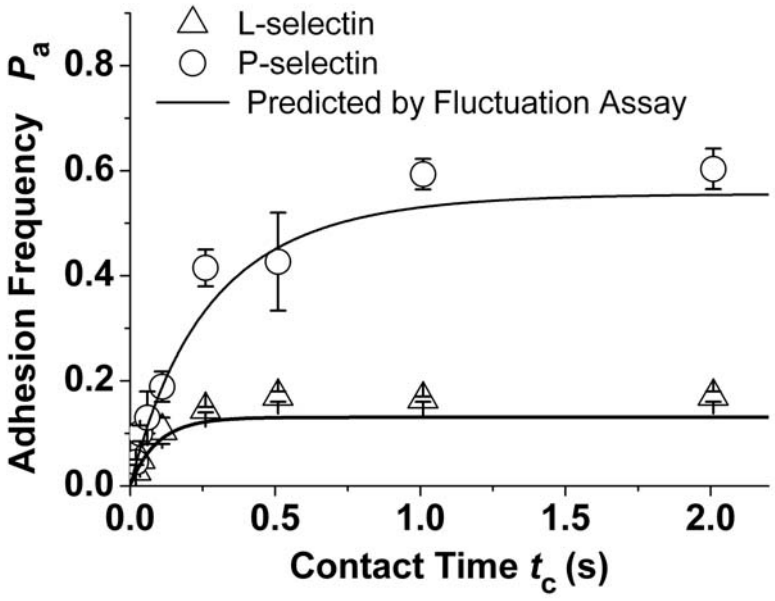

Figure 5-5. Comparison between theory and experiment. Frequencies of adhesion mediated by PSGL-1 interacting with L-selectin (Δ) or P-selectin (○) were measured at indicated contact times (points, mean ± S.E.M. of three probe-target pairs) by averaging the adhesion scores (1 for pulling and 0 for no pulling at the end of the contact time of each test cycle) from 100 test cycles per probe-target pair. Theoretical adhesion frequencies as functions of contact time were predicted (curves) by Equation 5-4 using the kinetic rates from Figure 4-4C and molecular densities measured from independent experiments ($m_r m_l$, = 0.2 and 0.15×10^5 μm^{-4} for the L- and P-selectin cases, respectively).

5.3 Discussion

In this chapter we developed a method for monitoring 2D receptor-ligand interactions based on thermal fluctuations of a BFP probe. The ability of our method to identify events of bond association/dissociation has been demonstrated by rigorous control experiments (Figure 5-1 and 5-2) and kinetic experiments (Figure 5-3). The control experiments included: 1. matching the periods with higher mean positions ($x > 0$) and those with reduced standard deviations ($\sigma < 3.15$ nm) (Figure 5-1 B and D); 2. matching the two subpopulations in the histograms of σ values with those of a free probe with the same spring constant and an increased spring constant (Figure 5-1 F and G), respectively; and 3. correlating the thermal fluctuation method with the pulling method for determining the presence/absence of a bond (Figure 5-2). The kinetic experiments included: 1. independently measuring on-rate and off-rate as well as their dependence on the interacting molecules from separate data of the same experiment (Figure 5-3); 2. confirming the mass action effect on the cellular on-rate $m_r m_l A_c k_{on}$ and the lack of such effect on the off-rate k_{off} (Figure 5-4); and 3. comparing the theoretical P_a vs. t_c curves predicted using kinetic rates obtained by the thermal fluctuation method with the experimental data measured directly by the adhesion frequency assay (Figure 5-5). Collective data from all these tests provide convincing evidence for the validity of the new method.

We have demonstrated the utility of the thermal fluctuation method by 2D kinetics measurement, which is an extension of our previous adhesion frequency method [82]. Both assays employ the same experimental procedures (Figure 5-1 B and C). However, the adhesion frequency assay acquires only one bit of information: whether adhesion is

present or not at the end of the contact time. By comparison, the thermal fluctuation assay measures when bonds form and dissociate, which greatly increases the quantity, quality, and variety of information. For example, the adhesion frequency assay obtained a binary adhesion score, 0 or 1, for each of the two test cycles shown in Figure 5-1 B and C. By comparison, we learned from the thermal fluctuation assay that bonds formed six (Figure 5-1B) or two (Figure 5-1C) times, respectively, at 2.75, 3.15, 3.48, 3.76, 4.82, and 5.56 s (Figure 5-1*B*) or 2.07 and 2.93 s (Figure 5-1*C*), respectively, which dissociated at 2.80, 3.25, 3.54, 3.86, 5.31, and 5.83 s (Figure 5-1B) or 2.35 and 5.8 s (Figure 5-1C), respectively. Simple processing of these data yields 0.35, 0.23, 0.22, 0.96, and 0.25 s (Figure 5-1B) or 0.58 s (Figure 5-1C) waiting times and 0.05, 0.10, 0.06, 0.10, 0.49, and 0.27 s (Figure 5-1B) or 0.28 s (Figure 5-1C) bond lifetimes, respectively.

Compared to the adhesion frequency assay, the thermal fluctuation assay acquires more data in a shorter time and improves the reliability of the estimated kinetic rates. The kinetic rates are evaluated by a two-parameter fit of Equation 5-4 to the P_a vs. t_c data in the adhesion frequency assay [82], which may use errors in one parameter to compensate for errors in the other parameter to achieve an apparently good fit. By comparison, the bond formation and dissociation events can be visualized individually in the thermal fluctuation assay, which enables segregation of waiting times from bond lifetimes to allow their respective analysis with two separate single-parameter fits, one for on-rate (Equation 5-2) and the other for off-rate (Equation 5-3), which are much more robust.

Careful inspection of Figure 5-5 reveals that the theoretical predictions slightly underestimate the experimental data. Fitting Equation 5-4 to the data returns a larger cellular on-rate $m_r m_l A_c k_{on}$ than, but a similar off-rate k_{off} to, their respective counterparts

measured from the thermal fluctuation method. A possible explanation is that in the adhesion frequency assay, the probe and the target are pressed against each other, resulting in a larger contact area A_c than that in the thermal fluctuation method where the two surfaces are in contact via thermal fluctuation but not by compression. In fact, the data of higher mean positions when a bond was formed, as observed in Figure 5-1B, suggest that the two surfaces were separated by an average distance greater than the molecular length of the receptor-ligand complex by 10-12 nm. Although thermal fluctuations did bring the probe into contact with the target to enable bond formation, such contact was likely transient and discontinuous. In other words, the holding time of the approach-push-retract-hold-return cycle was likely broken down into interlude periods of contact and noncontact [57]. This is in contrast to the case of the adhesion frequency assay where the two surfaces were more likely to be in continuous contact.

The above reasoning suggests that the thermal fluctuation method can be used to measure not only on-rate but also its dependence on the mean distance x_m between the two surfaces. Increasing this gap distance is expected to reduce the mean collision frequency, encounter duration, and contact area, thereby decreasing the rate of bond formation. Furthermore, thermal fluctuations of the probe are Brownian motion confined in an energy well $U = 0.5k(x - x_m)$ with an equilibrium position at x_m and a curvature defined by the BFP spring constant k. Tuning the spring constant stiffer is expected to reduce the probe thermal fluctuations, thereby decreasing the rate of bond formation. Thus, our method can be used to measure the mechanical regulation of on-rate by separation distance between the probe and target and by the BFP stiffness.

The thermal fluctuation method measures both on- and off-rates by sorting

different intervals from the same time course into waiting times and bond lifetimes. Increasing the separation distance will affect not only on-rate as described above, but also off-rate because the bonds so formed will be subjected to a force *f*, as visualized in Figure 5-1B. Lifetimes of bonds of P-selectin [47] and L-selectin [48] with PSGL-1 have been measured as functions of force for f > 5-10 pN by atomic force microscopy [47, 48] and by the BFP [53]. Extrapolating these k_{off} vs. f data to zero force yields values much greater than those actually measured here, suggesting that there may be unexpected changes in the range of $0 < f < 5$ pN. The thermal fluctuation method should be ideal for such studies.

Measuring mechanically regulated 2D kinetics is only one of many possible applications of the thermal fluctuation method. Different receptor-ligand complexes exhibit different mechanical properties, which are predicted to reduce thermal fluctuations by different amounts [84]. Indeed, preliminary support for this prediction has already been seen in the histogram analysis of σ data (Figure 5-1 F and G). It is evident that the peak of the subpopulation of σ values that corresponded to the probe bound to the target by an L-selectin bond (Figure 5-1*F*, $\bar{\sigma}_1$ = 1.6 nm) was left-shifted relative to that by a P-selectin bond (Figure 5-1*G*, $\bar{\sigma}_1$ = 2.2 nm). These data suggest that we may be able to identify the type of bonds formed/dissociated in addition to when they are formed/dissociated. This expanded capability can be used to study how multiple species of receptor-ligand interactions cooperate to mediate adhesion not only between two beads but also between a bead and a live cell to allow study of signaling.

Finally, we note that the thermal fluctuation method can be implemented using an optical trap or laser tweezers. In fact, optical trap was used as a force sensor to monitor

the mean bead position change as an identifier for antibody-antigen dissociation and association events in a manner similar to those observed in Figure 5-1B (arrowheads) [88]. Thus, our newly developed method should have broad applications because it can measure a wide variety of parameters for interacting receptors and ligands using commercially available instruments.

CHAPTER 6

FUNCTIONAL STUDY OF FORCE REGULATION ON SELECTIN-LIGAND INTERACTIONS

6.1 Introduction

The interactions of selectins with their ligands mediate leukocyte tethering to and rolling on endothelial surfaces during inflammation and immune responses [89, 90]. But their interactions do not only depend on their own structures; they also heavily depend on the hydrodynamic environment of the circulation to impose kinetic and mechanical stresses. It has been well known that mechanical force applied to these bonds affects their dissociation rates and hence their lifetimes [47, 48].

L-selectin requires a counterintuitive threshold shear to mediate both tethering and rolling [91, 92]. As flow increases to an optimal level, more cells tether and the cells roll more slowly. Above the flow optimum, fewer cells tether and the cells roll more rapidly. Distinct physical mechanisms regulate flow-enhanced tethering and rolling. Three mechanisms have been postulated to explain how transport augments tethering: sliding of the cell bottom on the surface, Brownian motions of the cell, and rotational diffusion of L-selectin and its ligand[93]. As well, mechanical force enhances the leukocytes' rolling by decreasing the rate of L-selectin's dissociation from its ligands. Normally, forces shorten the lifetimes of receptor-ligand interactions (slip bonds) [94]. However, at low

levels force paradoxically prolongs the lifetimes of selectin-ligand interactions (catch bonds) before they convert to slip bonds at higher forces [95, 96]. Catch bonds are particularly evident for L-selectin [96] as well as for P-selectin [47]. As flow increases from the threshold to an optimal value, rolling becomes slower and more regular as force prolongs the lifetimes of L-selectin, so-called catch bonds [97]. Above the flow optimum, rolling becomes faster and less regular as higher forces shorten the lifetimes of slip bonds. Several models to explain transitions from catch bonds to slip bonds have been proposed [98]. However, little is known about the structural basis for catch bonds.

All three selectins share similar structures but there are different numbers of consensus repeats [89, 90]. There are only a few non-covalent interactions between the lectin and EGF domains, most of which are conserved among the three selectins. Two P-selectin structures have been described, one with a more open angle between the two domains [8] (Figure 6-1A). The structures suggest that the P-selectin lectin domain can pivot on a hinge over the EGF domain. Compared to P-selectin's structure, x-ray structures of lectin and EGF domain of L-selectin showed closer angles (contributed by Dr. McEver's lab). Thus, we postulated that this conformational change is common to all three selectins and that it plays an important role in regulating the kinetic off-rate of selectin-ligand interactions. The sliding-rebinding model[52] predicts that substituting Gly for Asn138 in L-selectin (L-selectinN138G) will reduce the force required to elicit catch bonds, prolong their lifetimes, and lower the force where catch bonds convert to slip bonds even with molecularly distinct ligands. Here, we show that eliminating a hydrogen bond by N138G mutation to increase flexibility of the inter-domain hinge in

L-selectin indeed augments catch bonds in the low force region by the BFP lifetime measurements.

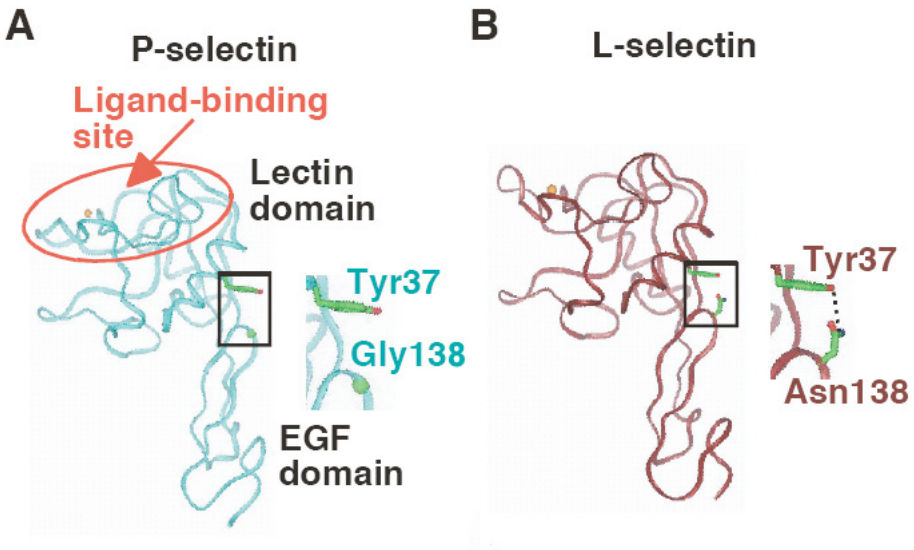

Figure 6-1. X-Ray structures of the lectin and EGF domains in P-selectin (A) [8] and L-selectin (contributed by McEver's lab)(B).

In addition to the external forces, the history of applied force can also regulate the dissociation of selectin-ligand interactions. Previous P-selectin-PSGL-1 AFM studies have shown that off-rate (inverse of bond lifetime) depends not just on the instantaneous force value (Bell model), but, in fact, it also depends on the entire history of force application [99]. Here, we used a new and different assay that was originally invented by S. Krishnna (previous graduate student in Dr.Zhu's lab) to measure L-selectin-ligand bond lifetimes at different loading rates and at different forces. This is a little difference from the widely used DFS analyses[65], in which the bonds were loaded continuously with different loading rates till rupture. S.Krishnna *et al*. first observed this force-history dependent transition of bond lifetimes in L-selectin/ligand interactions (S.Krishnna *et al.*

published data). Here, the BFP was used to confirm the force history effect on the catch bonds.

Regarding no-force off-rates, discrepancies exist between the published zero-force off-rates of P-, and L-selectin and ligand interactions measured by SPR [100, 101] and by extrapolation to zero-force from the catch bonds measured by AFM[47, 48]. The sliding rebinding model predicted that another slip bond region may exist in the very low force region in which the interaction between lectin and EGF domain has not been broken yet. Thus, to further support this model as well as to reconcile the discrepancies, the BFP and lifetime measurement were used to identify the potential existence of slip bonds in the lower force regime where previous the BFP and AFM experiments had not touched.

6.2 Results

6.2.1 L-selectin hinge mutation augmenting catch bonds in low force regimes

To confirm and support the sliding rebinding model [52], we measured how force affected the lifetimes of interactions of recombinant L-selectin-Ig and L-selectinN138G –Ig with two different ligands, PSGL-1 and 6-sulfo-sLe^x. The BFP was used to obtain lifetimes. In the BFP experiments, interactions of L-selectin or L-selectinN138G coated on a target bead with PSGL-1 or 6-sulfo-sLe^x coated on a probe bead were stressed through a red blood cell to allow lifetime measurements at various levels of constant forces.

Before measuring lifetime experiments, binding specificity was determined firstly to make sure we were indeed measuring the interactions between L-selectin and its ligand.

To ensure that the binding between L-selectin and ligand was at single molecular level, we coated molecules on beads at very dilute concentration to keep the binding frequency less than 20%. When testing the probe bead without PSGL-1, we found very low binding frequency (< 20%) as shown in Figure 6-2. Since L-selectin and their ligand binding is Ca^{2+} dependent, we added 5mM EDTA into the experimental buffer to remove the Ca^{2+} and measured the binding frequency again between target and probe beads. We found that the binding frequency greatly dropped to ~ 3%, which should be from non-specific binding. Further more, we added 10ug/ml anti-L-selectin mAb DREG56 to block the ligand binding site on L-selectin and then measured binding between target and probe bead again. We found that the binding frequency also dropped to ~3%, just like the condition with 5mM EDTA. The decrease in the binding frequency to a very low level following the addition of EDTA or DREG56 mAb clearly suggested that our measurements between L-selectin coated target bead and PSGL-1 coated probe bead were highly specific (Figure 6-2).

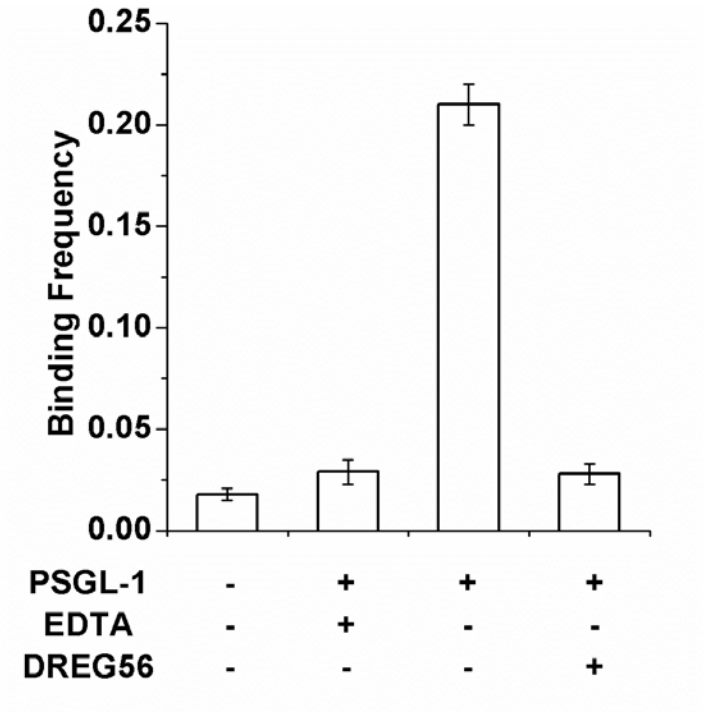

Figure 6-2. Binding specificity.

In lifetime experiments, a large number of lifetime measurements were used to derive the mean lifetime (which equals the reciprocal off-rate $1/k_{off}$ for first-order dissociation of single bonds) for each interaction at each tensile force. As observed previously [97], the lifetimes of L-selectin interactions with both ligands demonstrated a biphasic pattern characteristic of transitions from catch to slip bonds . Initial increases in force prolonged mean lifetimes until an optimal value was reached; further increases in force shortened lifetimes. Although L-selectinN138G interactions with both ligands also exhibited transitions between catch and slip bonds (Figure 6-3), the lifetimes in the catch bond regime were significantly longer and the transitions to slip bonds occurred at lower forces. In contrast, there was little difference in the lifetimes of L-selectin and L-selectinN138G interactions in the slip bond regime.

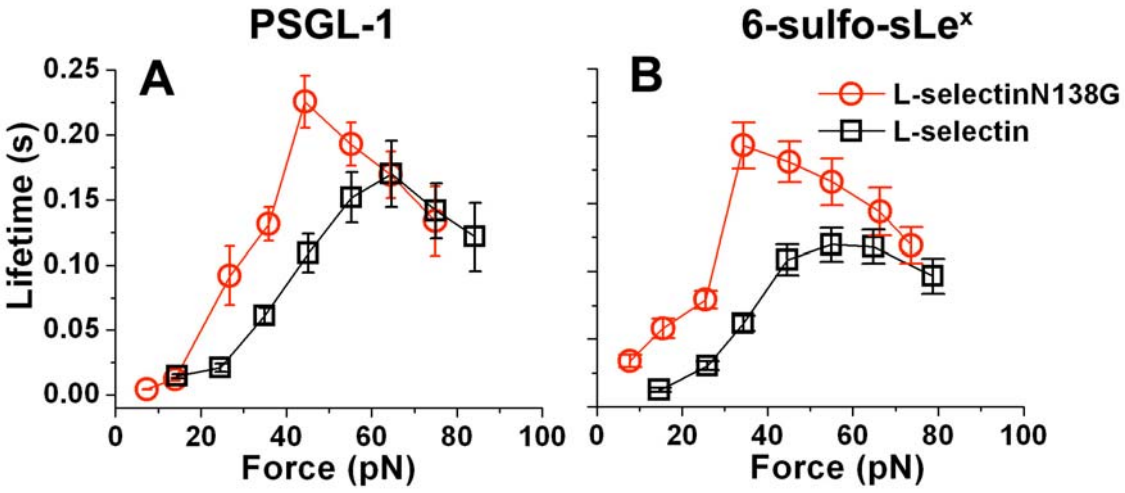

Figure 6-3. Bond lifetimes measurement between L-selectin (or L-selectinN138G mutant) and PSGL-1 (A) or 6-Sulfo-sLe^x (B). The data in A, **B represent the mean ± S.E.M. of ~500 lifetime measurements.**

6.2.2 Tri-phasic transition of fore-regulated off-rates of selectin-ligand interactions

The sliding rebinding model predicted the existence of slip bonds in the lower force regime (<10pN) before the interactions between lectin and EGF domain broke, and it predicted the existence of discrepancies between reported zero-force off-rates measured by SPR and extrapolated off-rates from catch bonds by the AFM and the BFP. Based on these observations, we highly suspected that another slip bond regime may exist in the very low force regime where the AFM and the BFP had not ever touched before. Flow chamber studies of E-selectin-ligand interactions have already shown tri-phasic pattern (Wayman A. *et al.* unpublished data), which highly increased the possibility of observing tri-phasic transition in selectins/ligands interaction by the BFP. Thus, to test this hypothesis, we first measured force-dependent lifetimes of P-selectin-PSGL-1 bond. As

shown in Figure 6-4A, in the force regime above 5pN, P-selectin-PSGL-1bonds show catch-slip transitions measured by the BFP that are similar to those measured by AFM before [47], even though the optimal forces were a little bit different. More interestingly, the BFP detected another slip bond regime existing in the force regime below 5pN, where AFM was unable to detect due to its stiffer force sensor and much lower force sensitivity. The average lifetime at the lowest force (~1pN) was about 0.55s, which is much closer to the reported zero-force lifetime by SPR, 0.7s[100]. As three selectins share similar structures, we also highly suspected that other two selectins (E- and L-selectin) and their ligand interactions might have the tri-phasic transitions of force-regulated bond lifetimes observed in P-selectin-PSGL-1 bonds. Thus, we measured force-dependent lifetimes of E-, L-selectin and their ligands interactions. As expected, all of these three interactions indeed showed slip-catch-slip tri-phasic transitions of force-regulated bond lifetimes (Figure 6-4 B, C and D). Our results showed that the lifetime at 1pN of L-selectin and its ligands interactions were about ~0.1s, which is very close to the reported zero-force lifetime ($\leq$ 0.1 s) measured by SPR [101].

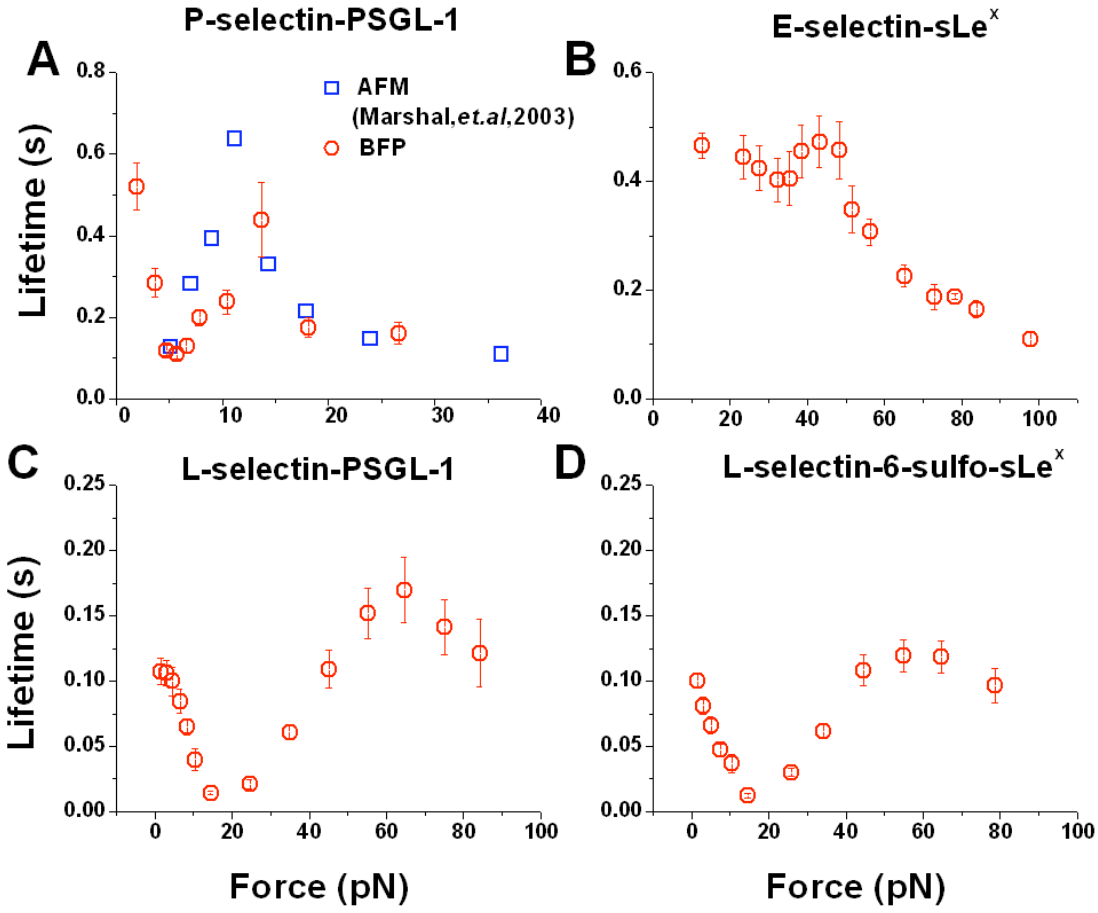

Figure 6-4. Triphasic transition of force-dependent lifetimes of P-selectin-PSGL-1(A), E-selectin-sLex(B), L-selectin-PSGL-1 (C) and L-selectin-6sulfo-sLex bonds (D). Each point in every plot has at least 50 measured lifetimes.

6.2.3 Force-history dependent off-rates of L-selectin-ligand interactions

Unlike the lifetime assay used in the L-selectin hinge mutant experiments, here, we varied both clamping force and loading rates. The clamping force ranged from 10 pN~80 pN, and the three loading rates were used, 10^3pN/s, 3x10^3pN/s and 10^4pN/s. The raw lifetime data of 10^3 pN/s and 10^4 pN/s loading rates are shown in Figure 6-5.

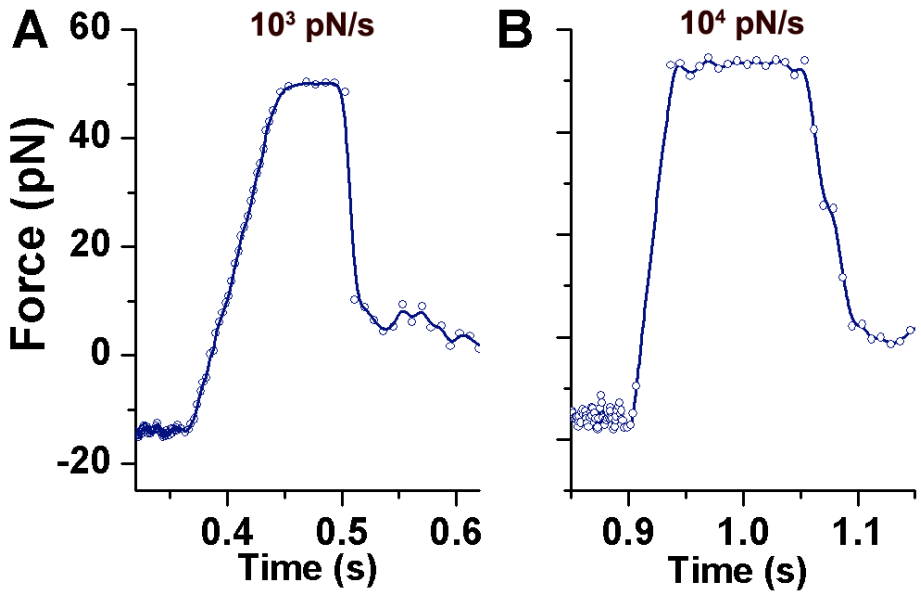

Figure 6-5. Raw data of lifetimes at the loading rates of 10^3pN/s (A) and 10^4pN/s (B).

We only characterized the interactions between L-selectin and PSLG-1 with different force loading rates. Interestingly, we found as force loading rates increase, the optimum lifetime gradually shifted leftwards to the lower force regime, and finally catch bonds behavior was abolished and completely replaced by slip bonds once the force loading rate

was increased to 10^4 pN/s (Figure 6-6 A). These results showed that increasing loading rates augmented the bond lifetimes in the low force regime of catch bond, but they shorten bond lifetimes in the high force slip bonds regime (Figure 6-6A). In contrast, the L-selectin-6-sulfo-sLe^x bond was quite resistant to loading rates; that is, as loading rates increased, the optimum force did not shift to lower force, and the lifetimes in catch bonds regime were not enhanced (Figure 6-6B).

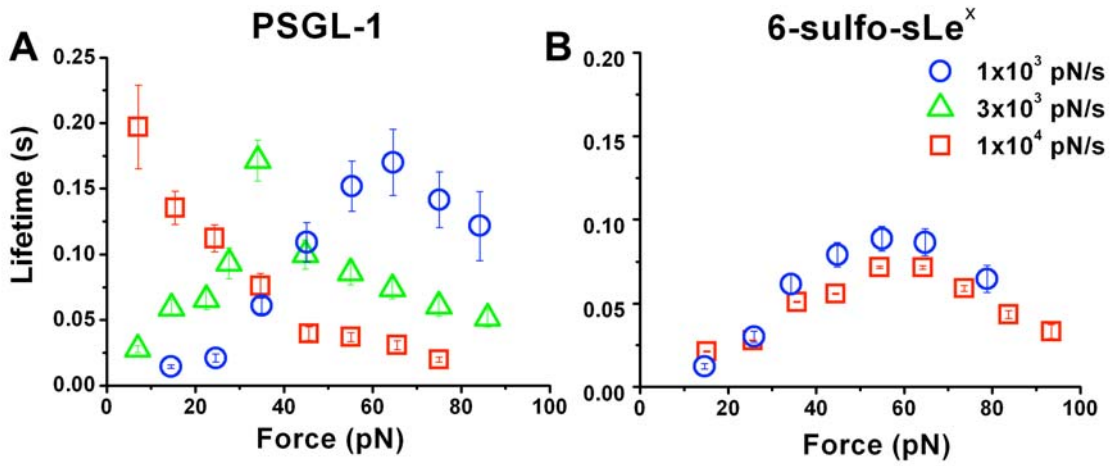

Figure 6-6 Lifetimes of L-selectin-PSGL-1 bond (A) and L-selectin-6-sulfo-sLe^x bonds (B) regulated by force loading rates and clamping forces.

6.3 Discussion

In this study, we used the BFP to carry out functional studies of selectin-ligand interactions by characterizing how catch bonds were regulated by biochemical and biophysical factors in order to reveal the mechanism of catch bonds. First, we characterized how a single residue mutation, specifically substituting Asn for Gly on the residue 138 at the inter-domain hinge between lectin and EGF domain of L-selectin, regulated the catch bonds between L-selectin and ligand interactions. At the putative hinge region of P-selectin, Tyr37 of the lectin domain is located close to Gly138 of the EGF domain (Figure 6-1A). As previously proposed [8], the lack of a side chain in Gly138 should favor flexibility between the domains. By contrast, E- and L-selectin have an Asn at residue 138, and published structures of E-selectin reveal a hydrogen bond between Tyr37 and the side chain of Asn138 in a closed-angle conformation [7, 8]. With a solved but unpublished crystal structure of the lectin and EGF domains of L-selectin (P.M., V. Oganesyan, S. Terzyan, T. Mather, and R.P.M, unpublished data), we found that there was a hydrogen bond between Tyr37 and Asn138 in a closed-angle conformation (Figure 6-2B). This one residue difference may bring about a difference in flexibility of the lectin domain, which could result in intrinsic on-rates and off-rates that differ from L-selectin's ligand based on the sliding rebinding model proposed by Lou *et al.*[52]. But how could this flexibility cause these differences in ligand binding kinetics?

According to the sliding rebinding model, "catch" results from the forced opening of an interdomain hinge that tilts the binding interface, allowing the two sides of the contact to slide against each other. This sliding promotes formation of new interactions and even rebinding to the original state, thereby slowing dissociation and prolonging bond

lifetimes [52, 53](Figure 6-7). L-selectinN138G mutation made the lectin domain more flexible by eliminating one hydrogen bond. This mutation tilts the lectin domain's angle to favor open configuration than L-selectin, so more sliding and rebinding takes place between the ligand and lectin domain interfaces even at lower force regime. Therefore, at lower force regime, L-selectinN138G mutant-ligand bond lifetimes were longer and the optimal force was smaller than L-seletin-ligand's. Once the inter-domain angle is fully open, further increases in force can no longer increase rebinding, resulting in transition from catch bonds to slip bonds.

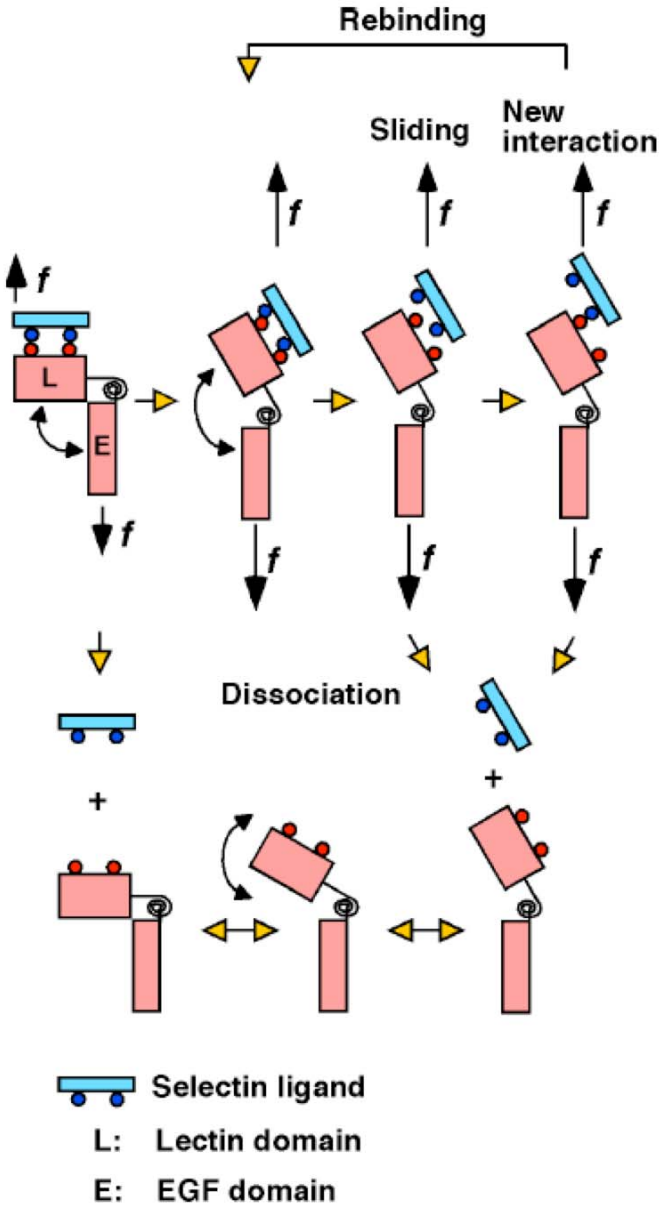

Figure 6-7. Sliding rebinding model for selectin-ligand interactions[53].

The tri-phasic transitions of force dependent lifetimes of selectin-ligand interactions were observed in all three selectins. This tri-phasic transition was predicted by the sliding rebinding model. Two threshold forces are critical in this sliding rebinding model. The lower one is the force to break the interactions between lectin and EGF domain to release the lectin domain and allow it to rotate to an open configuration. The higher one is the force to fully open the lectin domain. When the force is below the lower threshold, no sliding and rebinding occur at the ligand binding interface, so the dissociation follows the Bell model, which is single exponential decay, for so-called slip bonds. As force increases further, the selectin's lectin domain starts to open to allow more sliding and rebinding to occur, as mentioned previously. Our observed tri-phasic transitions not only reconcile the discrepancies between data measured by SPR and AFM, but also further support the sliding rebinding model, which provides a very nice structural basis to explain the counter-intuitive "catch bond" behavior in selectin ligand interactions. Whether this model could also be applied to other catch bonds in other molecular systems needs further careful investigation and more experiments.

In addition to the ability of biochemical mutation on the selectin structure to alter catch-slip bond transition, biophysical factors could also regulate this transition. By increasing force loading rates, both AFM and AFM (S.K.K.'s unpublished data) results showed that the catch bonds gradually shift to the lower force regime and finally convert to slip bond. From the biophysical view, the two states model has nicely explained the catch bond in P-selectin and its ligand interactions[55].This two state model suggests that P-selectin could dissociate along two different pathways with different dissociation rates. It was assumed that initially ligand binding has two states with different subpopulations,

and that it can convert between two binding states in equilibrium. Mechanical force loading rates could select different subpopulations of two binding states to dissociate along two different pathways. Therefore, our force history data suggested that different loading rates may be able to pre-select pathway to dissociate. The higher loading rate may select the slow dissociating pathway but may completely block the fast pathway so that force dependent lifetimes at the loading rate of 10^4 pN/s behaved with only single exponential decay. Using the view of molecular structure to explain this interesting phenomenon, we were still not very clear as to how loading rates regulated the hinge domain rotation. Since ligand dissociation rates not only depend on the hinge site but are also heavily dependent on the ligand binding site, the change of loading rates might greatly alter the conformation on the ligand binding site and strengthen binding. This strengthening might cause single exponential decay on the force-dependent lifetimes. The lifetimes of L-selectin-6-sulfo-sLex were highly resistant to the loading rates. Since this binding does not involve peptide binding, we suspect that the peptide binding part may be important for changing the binding site's conformation.

CHAPTER 7

FORCE REGULATION ON LFA-1-LIGAND INTERACTIONS

7.1 Instruction

Integrins, a large family of cell adhesion receptors, mainly mediate cell adhesion to other cells or to extracellular matrix. They behave as mechano-chemical transducers transmitting mechanical and biochemical signals bi-directionally across the cell membrane in various cellular processes [12, 13]. For example, the bindings of LFA-1 to ICAM-1 mediate leukocytes' rolling on and firm adhesion to inflamed endothelial beds during leukocyte trafficking, they regulate T lymphocyte's rest in the T-cell zone of secondary lymph node tissues, and they modulate the immunological synapse formation. Integrins' functions in these cellular processes are tightly regulated by the affinity of binding to their ligands[18]. However, most of time LFA-1s are kept in an inactive and low affinity state so that they are not very adhesive to their ligands. Once activated by inside-out signals from other receptors (i.e., GPCR, TCR) or by outside-in signals from its ligands, LFA-1 rapidly switches to a high affinity state and becomes very adhesive [12]. These activation processes are believed to be facilitated by mechanical forces[18].

Integrin's binding affinity is known to be controlled by its local and global conformational changes[12]. Global conformational rearrangements mainly include large scale switch-blade like extensions of integrins. In the inactive and low affinity state, two subunits of a hetero-dimeric integrin are highly compact, and their headpieces stay

close and bent toward cell membrane[13]. Upon activation, an integrin dramatically extends its headpiece away from the cell membrane, like a switch-blade. Companied with these large scale global conformational changes, local conformational rearrangements occur in the βA domain of all integrins as well as in αA domain if an integrin contains an αA domain, i.e., LFA-1. The key component of the local conformational changes in LFA-1's αA domain is the downward movement of c-terminus α7 helix. This downward movement allosterically rearranges the conformation of MIDAS in the αA domain to the open and high affinity state with longer bond lifetimes in binding with LFA-1's ligands. This is caused by the downward movement of the α7 helix, the Glu127 at end of the α7 helix anchors onto the MIDAS of the βA domain and it acts as its intrinsic ligand [12]. Thus, most of time, these local conformational changes in the αA domain always were accompanied by global conformational changes. But some small allosteric molecules, such as XVA143, can separate these global and local conformational changes; that is, such molecules induce extension of LFA-1 but prevent the binding of the α7 helix in the αA domain to the MIDAS in the βA domain so that the αA domain is locked in close and low affinity state[19].

Considering the mechanical environment where integrins work, mechanical force plays a critical role in facilitating global and local conformational changes of integrins to activate integrins to a high affinity state by substantially increasing bond lifetimes. Experimentally, recent studies have demonstrated force-enhanced integrin's functions [102, 103]. Also, by steered molecular dynamics simulations, researchers have suggested how force-activation of an integrin might occur [104, 105]. Thus, it is reasonable to

speculate that catch bonds, a counter-intuitive phenomenon of increasing bond lifetimes with increasing forces, exist in integrin/ligand bonds. To date, catch bonds have been observed in many molecular interactions, such as interactions between selectins and ligands [95, 106], glycoprotein Ib (GPIb) and von Willebrand factor (VWF) [49], actin and myosin [50], FimH receptor and mannose [51]. However, catch bonds for integrin/ligand interactions were not observed by loading rate-dependent rupture force measurements with AFM's force-ramp experiments and DFS analysis [107-109], nor did cell tether lifetime measurements with a flow chamber [110]. Here, we used the BFP to measure bond lifetimes of LFA-1/ICAM-1 bonds at single molecule level. Catch bonds were observed in 5pN~15pN range. More importantly, we observed that XVA143's binding to LFA-1 abolished its catch bonds in interacting with ICAM-1. Therefore, this abolishment by XVA143 may provide a structural mechanism to explain the catch bonds in the interactions between αA domain containing integrins and their ligands.

7.2 Results

7.2.1 Binding specificity in the BFP experiment

Using the BFP (Figure 7-1A), we directly measured the interactions between ICAM-1-Fc coated on a probe bead and LFA-1 expressed on a Jurkat cell. As shown in Figure 7-1, the Jurkat cell was aspirated on a micropipette driven by the PZT to approach and contact the probe bead (Figure 7-1). As described previously in chapter 3, the absence (Figure 3-1A) or presence (Figure 3-1B) of adhesion was detected upon the retraction of the target micropipette by the PZT to a desired force for a lifetime

measurement (Figure 3-1B).

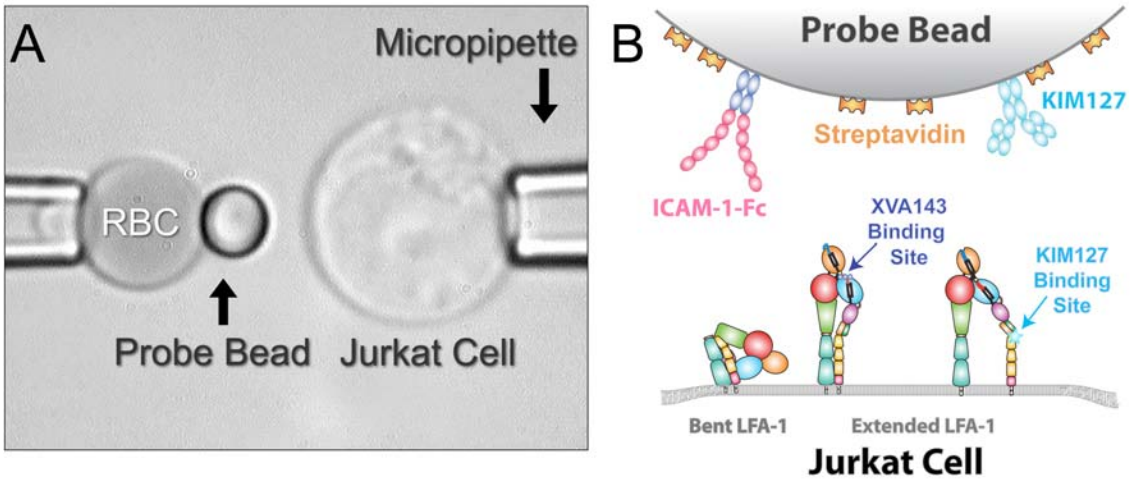

Figure 7-1. The BFP experiment. (A) Photomicrograph of a BFP. (B) Functionalization of the BFP. ICAM-1-Fc or KIM127 mAb were covalently linked to a streptavidin-decorated probe bead via hetero-bifunctional polymers, maleimide-PEG3500-NHS. LFA-1 integrins with bent or extended conformations were expressed on the Jurkat cell. KIM127's binding site on a LFA-1(light blue star, pointed by the light blue arrow) exposed after LFA-1 extends is on the genu site of the β subunit of a LFA-1. The binding site of allosteric small molecule (XVA143, dark blue balls) is in the αA domain of LFA-1 (pointed by the dark blue arrow).

To ensure that the interaction between ICAM-1 and LFA-1 was specific, the binding frequencies were measured between a Jurkat cell and a probe bead coated with or without ICAM-1. As shown in Figure 7-2, the binding was highly specific, for it was almost suppressed when the probe bead was coated without ICAM-1 but only with streptavidin. In order to have majority (>90%) of adhesion events from a single ICAM-1/LFA-1 bond, the coating densities of ICAM-1 on the probe bead were specifically adjusted at Mn^{2+} or Mn^{2+} plus XVA143 (Mn^{2+}/XVA143) to keep the adhesion frequency low enough, e.g.,

15%~20%. The adhesion frequency was also kept in the same range in the lifetime measurement of the interactions between KIM127 mAb and LFA-1.

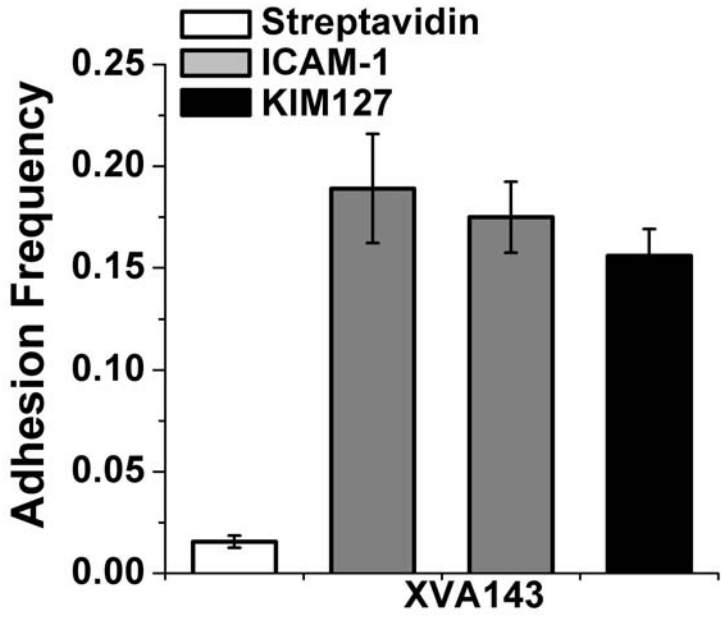

Figure 7-2. Binding specificity. Binding frequencies between a Jurkat cell, expressing LFA-1, and a probe bead covalently coated with streptavidin only, streptavidin and ICAM-1 or KIM127 mAb, were measured in ~50 tests of each pair of a target cell and a probe bead at 1mM Mn^{2+}, 1mM Mn^{2+}, 1mM Mn^{2+} plus 1μM XVA143, or 1mM Mn^{2+} plus 100μg/ml soluble ICAM-1 respectively. Error bars represented as mean ± S.E.M. of 3-5 pairs.

7.2.2 Observation and characterization of catch bonds in the LFA-1/ICAM-1 interaction

Mechanical regulation of the dissociation of ICAM-1 from LFA-1 on Jurkat cells was quantified by measuring the force-dependent lifetimes of single ICAM-1/LFA-1 bonds at

a 1mM Mn^{2+} condition. With hundreds of lifetimes at different force levels, mean lifetimes were plotted as a function of binding forces. As expected, our results clearly show that LFA-1/ICAM-1's binding exhibited catch bonds in low force regime and then transited to slip bonds once forces were beyond ~15pN. At ~15pN, the optimal force, the binding was strengthened to the optimal level and of the longest mean bond lifetime, ~2.5s (Figure 7-3A).

To further reinforce the observed catch bonds, force-dependent lifetimes of the interactions of LFA-1 with its antibody KIM127 were also measured. Since KIM127's binding required the exposure of KIM127's epitope in LFA-1 [111] (Figure 7-1B), Jurkat cells were incubated in HBSS- buffer (pH~7.4, ~150mOsm) with 1mMMn^{2+} and 100μg/ml soluble ICAM-1. As shown in Figure 7-3 B, the mean lifetimes of the interaction between LFA-1 and KIM127 exhibited slip bonds. This was consistent with the force-dependent lifetimes of typical antigen-antibody interactions modeled by Bell[43]. Compared to the catch bonds in the LFA-1/CAM-1 interaction, this slip bond observation implies that the catch bonds observed previously were real, and that the catch bonds really depended on the binding of ICAM-1.

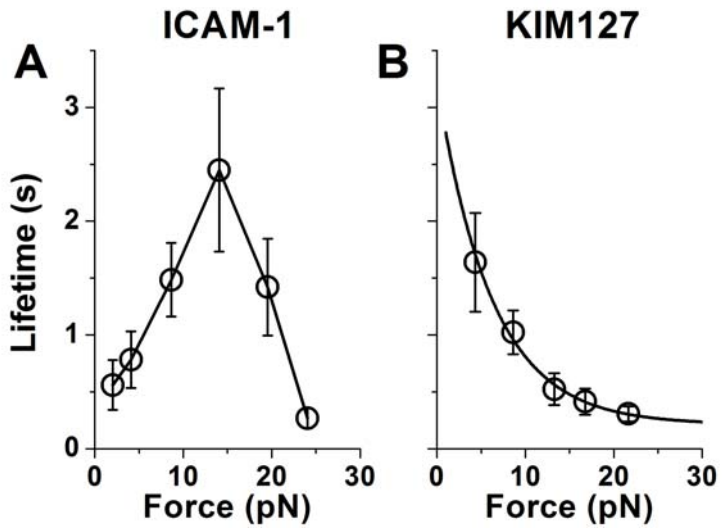

Figure 7-3. Force-dependent lifetimes of LFA-1/ICAM-1 and LFA-1/KIM127 bonds. (A) Plot of lifetimes (mean ± S.E.M.) vs. force of the interaction between ICAM-1 coated probe bead and the a Jurkat cell at 1mM Mn^{2+}. This plot shows the catch bonds in LFA-1-ICAM-1 bonds. (B) Plot of lifetimes (mean ± S.E.M.) vs. force of interactions between a KIM127 mAb coated probe bead and a Jurkat cell at 1mM Mn^{2+} and 100ug/ml soluble ICAM-1. This plots shows slip bonds in LFA-1-KIM127 bonds. Error bars in both (A) and (B) represent S.E.M..

Besides different patterns of the transitions of force-regulated mean lifetimes in the above two interactions, the distributions of lifetimes of these two interactions at all force levels also exhibited different orders of exponential decay. To analyze a lifetime distribution, ln(# of events with a lifetime > *t*) versus *t* was plotted. As the minimum threshhold set in the lifetime measurements was 10s, only those lifetimes shorter than 10s were included in this analysis. As shown in Figure 7-4A, LFA-1-ICAM-1 bonds exhibited a two-slope pattern in the plots of ln(# of events with a lifetime > *t*) versus *t* of each force in both the catch bonds regime (Figure 7-4A) and the slip bonds regime (Figure 7-4B). This two-slope pattern suggested a second order of exponential decay, which implied the coexistence of two binding states in the LFA-1/ICAM-1interaction. This two state binding observation suggested that ICAM-1 may dissociate from LFA-1

along two different pathways with two different dissociation rates. In contrast, the LFA-1-KIM127 bond exhibited the one-slope pattern of lifetime distributions, consistent with first order dissociation kinetics (Figure 7-4C). Furthermore, the lifetime distributions of LFA-1-ICAM-1 bonds clearly showed that in the low force regime (< 14pN) as force increased the plot of each lifetime distribution gradually swung rightwards (Figure 7-4A), indicating catch bonds; while in the high force regime (>14 pN) as force increased the plot of each lifetime distribution gradually swung leftwards, indicating slip bonds (Figure 7-4B and C).

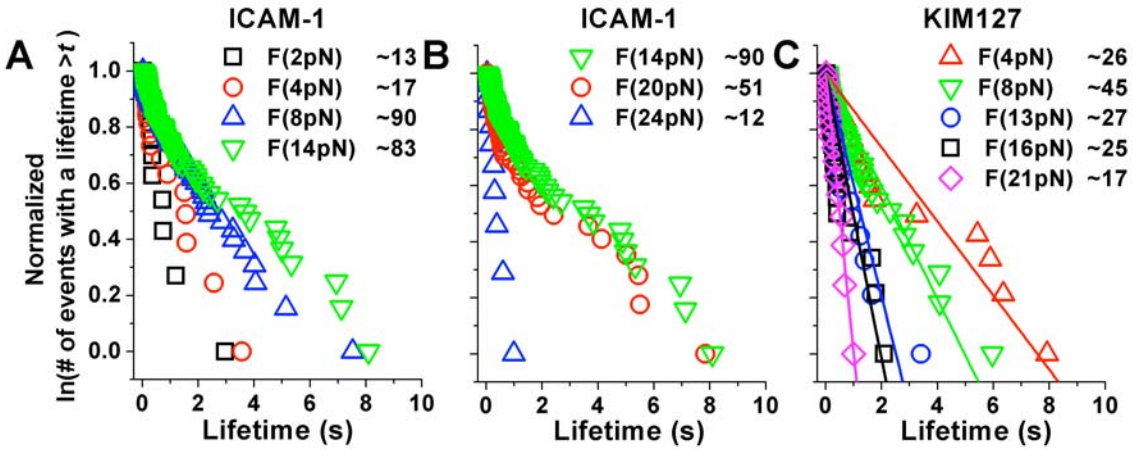

Figure 7-4. Lifetime analysis. Normalized ln(number of events with a lifetime > *t*) versus *t* plots for interactions of LFA-1 with ICAM-1 within catch bonds regime (A) and slip bonds regime (B) or with mAb KIM127. Plots in (C) were linearly fitted.

More interestingly, the fractions of all lifetimes longer than 10s were also dependent on the binding force between LFA-1 and ICAM-1. As shown in Figure 7-5, as force increased in the low force range, the fractions increased first but decreased when force was further increased. This biphasic transition pattern of the force-dependent fractions of long-lived lifetimes suggested that mechanical force could strengthen the

LFA-1-ICAM-1 bond by shifting more short-lived LFA-1-ICAM-1 bonds to long-lived bond lifetimes. Thus, this shifting of bond lifetimes further supported previously observed catch bonds.

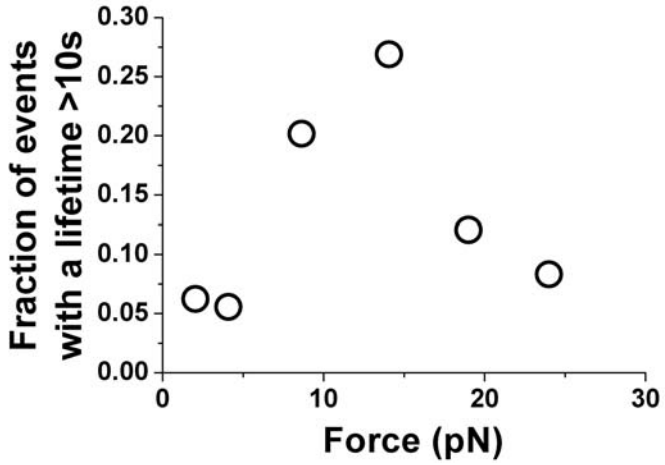

Figure 7-5. Plot of the fraction of events with a lifetimes >10s within each force bin vs. force of the interactions of LFA-1 with ICAM-1.

7.2.3 Binding of XVA143's to LFA-1 abolished LFA-1-ICAM-1's catch bonds

Having observed catch bonds between LFA-1 and ICAM-1 by previous lifetime analysis, we were more interested in the structural mechanism by which force regulates LFA-1's catch bonds. Related two-state transitions of bond lifetimes with closed and open conformations in LFA-1's αA domain, it was reasonable to hypothesize that the downward movement of the α7 helix in the αA domain regulated the catch bonds in the LFA-1-ICAM-1 interaction. To test this hypothesis, a small allosteric molecule, XVA143,

that induced LFA-1 switch-blade extension but locked αA domain in the close conformation, was used in the lifetime measurements of LFA-1-ICAM-1 interactions. As before, the force-dependent lifetimes of LFA-1-ICAM-1 bonds were measured and quantified upon XVA143's binding to LFA-1. As expected, our results showed that XVA143's binding to LFA-1 completely abolished catch bonds in the interactions between LFA-1 and ICAM-1 at 1mM Mn^{2+}, and the lifetimes of LFA-1-ICAM-1 bonds exhibited only slip bonds, decreasing from the maximum, ~0.3s, at the lowest force, ~8 pN (Figure 7-6A). More interestingly, the two-slope pattern did not exist in the plots of ln(# of events with a lifetime > *t*) versus *t*.(Figure 7-6B) at this condition. Instead, these plots only exhibited single exponential decay, suggesting that LFA-1 dissociated from ICAM-1 along a single pathway that might overlap with the fast dissociating pathway in the catch bonds. These lifetimes of LFA-1-ICAM-1 bonds upon XVA143's binding not only provided a control to further support the observed catch bonds, but also, more importantly, might reveal a structural mechanism to explain the catch bonds.

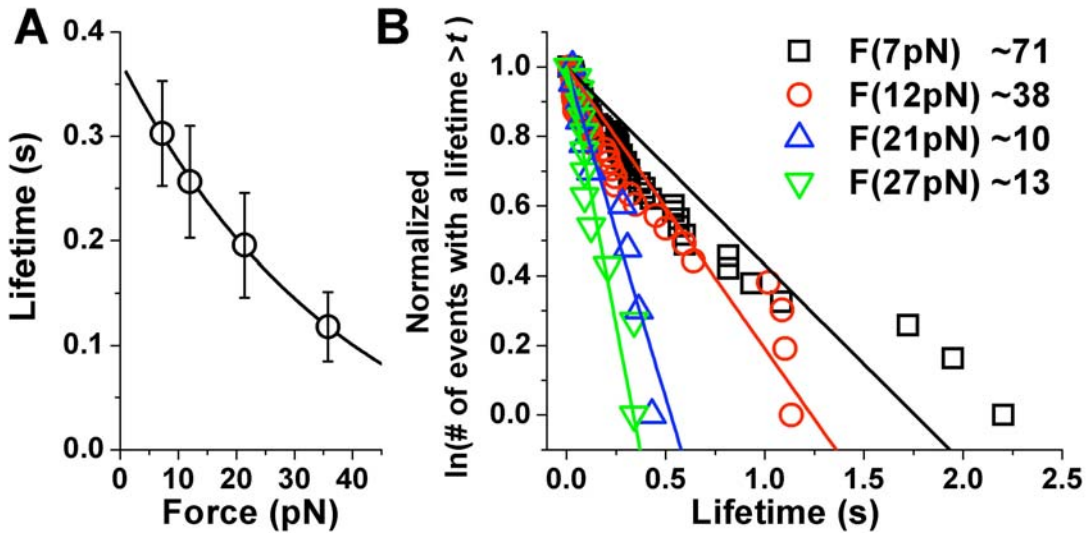

Figure 7-6. Force-dependent lifetimes of LFA-1/ICAM-1 bonds upon 1μM XVA143 binding and analysis on these lifetimes. (A) Plot of lifetimes as a function of force, fitted by Bell model[43]. Error bars represented S.E.M.. (B) Normalized ln(number of events with a lifetime > *t*) versus *t* plots for the interactions of LFA-1 with ICAM-1 upon 1μM XVA143 binding. Each plot is linearly fitted.

7.3 Discussion

Many molecular interactions, such as selectin-ligand [47, 48], GPIb/VWF[49] actin/myosin[50], and FimH/mannose [51] interactions, have exhibited counter-intuitive catch bonds phenomena. It has been also speculated for a few years that integrin/ligand interactions may also behave as catch bonds based on integrin's special structures and on models of their global and local conformational changes. However, previous published works did not reveal the existence of catch bonds in integrin/ligand interactions, because in these works researchers used DFS, assuming that dissociation occurred along a single exponential pathway and that bond lifetime decreased exponentially with increasing forces [107-109] as modeled by Bell [43], to analyze rupture forces from force-ramping experiments. In this chapter, using the BFP lifetime experiments, the catch bonds were observed in-situ in the interaction between LFA-1 and ICAM-1.

Catch bonds have been believed to tightly relate to the molecular structures of receptors, especially the ligand binding domain. Structural models have been proposed for the catch bonds between selectins and ligands [112], FimH and mannose [51], and GPIb and VWF [49]. Whether is global or local conformational changes required for LFA-1/ICAM-1's catch bonds? It has been known that extending an integrin could change integrins from a bent and low affinity state with short bond lifetimes to an extended and high affinity state with long bond lifetimes. Extension of the αA domain

containing integrin, i.e., LFA-1, could rearrange the local conformations of the αA domain by pulling down C-terminus α7 helix. The downward movement of this α7 helix allosterically opened up the αA domain to a high affinity state. Thus, mechanical forces could stabilize the position of the α7 helix in the position where the αA domain adopted high affinity state so that force could prolong bond lifetimes in a low force regime. This structural mechanism of the stabilization by mechanical force could be supported by our observed catch bonds in ICAM-1/LFA-1 interactions and slip bonds upon XVA143's binding to LFA-1. Upon XVA143's binding, the lifetimes of LFA-1-ICAM-1 become much shorter than those of catch bonds. This was consistent with a previous observation that XVA143's binding to LFA-1 could only support K562's rolling but not firm adhesion on ICAM-1 coated surface in flow chamber experiments[113]. This abolishment of catch bonds further supported our hypothesis and clearly suggested one possible structural mechanism of catch bonds in ICAM-1/LFA-1 interactions. This structural mechanism might be that force facilitated the α7 helix downward movement, allosterically opened up the MIDAS in the αA domain, and stabilized the MIDAS in high affinity state. So the higher force could result in a better stabilization of open conformations of the MIDAS so that it prolonged bond lifetimes between LFA-1 and ICAM-1. However, XVA143 blocked this α7 helix downward movement toward and binding to the MIDAS in the βA domain so that the αA domain was kept in the low affinity state under stressed condition[19]. As the α7 helix in the βA domain behaved in a manner similar to that in the αA domain[114], it is reasonable to speculate that catch bonds should exist in the αA domain bond lacking integrins and their ligands, and that

movement of the α7 helix in the βA domain might be the key to unravel the mechanism of αA domain lacking integrin's catch bonds.

In addition to this structural explanation, catch bonds could also be explained from the biophysical view of point. Without XVA143, the distributions of lifetimes of LFA-1-ICAM-1 bonds at each force level did not follow first order kinetic of single bond dissociation, single exponential decay. Instead, two-slope patterns, suggesting dual exponential decays, were very pronounced in both the catch-bond regime (Figure 7-4A) and the slip-bond regime of LFA-1-ICAM-1 bonds (Figure 7-4B). The dual exponential distribution of lifetimes suggested that two binding states may co-exist in the LFA-1-ICAM-1 bonds, and these bonds could switch between these two states, like interactions between selectins and their ligands [48, 55]. Upon force-activation, mechanical force can shift some subpopulation of LFA-1-ICAM-1 bonds from the state with low affinity and short lifetime to the other with high affinity and longer lifetimes. Phenomenologically, this shift results in increasing the mean lifetimes as force increased in low force regimes, so-called "catch bonds". Once all bonds were shifted to the high affinity state, further increasing force could not prolong lifetimes any more; lifetimes would instead decrease as the Bell model predicted. XVA143's binding to LFA-1 converted catch bonds to slip bonds in the LFA-1/ICAM-1 interaction, implying that this binding shifted all bonds to the low affinity state and blocked the transitions between these two states at the same time.

As a mechnotransducer, integrins transmit both mechanical and biochemical signals bi-directionally across the cell membrane via either inside-out or outside-in signaling pathway. Since mechanical forces are very complicated in the biological environment,

integrins should be able to respond differently to various mechanical stimuli. For example, LFA-1 behaves completely differently at an inflamed vascular site where shear stress exists from at lymph nodes where shear stress is free. This ability to strengthen bonds with forces may be important for LFA-1/ligands bonds for regulating leukocyte rolling and firm adhesion during leukocyte trafficking. As well, the ability to greatly reduce lifetimes of the LFA-1/ICAM-1 bond in order to shut down the adhesiveness of LFA-1 is very important for a leukocyte searching for its cognate antigens inside the secondary lymphatic organs. Therefore, catch bonds provide a mechanical mechanism at the molecular level for the cell to regulate adhesion by applying different forces externally or internally as desired.

CHAPTER 8

PROBE FORCE REGULATED DYNAMIC CONFORMATIONAL CHANGES OF LFA-1 INTEGRIN ON A LIVING CELL

8.1 Introduction

Integrin, heterodimeteric membrane proteins (e.g., LFA-1 or αLβ2), play a critical role in the interactions between cells and cells or between cells and extracellular matrix (ECM) in various cellular processes. For example, LFA-1 (αLβ2 integrin), containing an αA domain where ligands (e.g., ICAM-1) bind, mainly mediates leukocyte rolling on and firm adhesions to endothelial beds at inflamed sites during leukocyte trafficking. Integrins regulate their physiological functions by changing their conformations between multiple states.

To date, multiple conformational states of integrins have been identified by many groups with various advanced high-resolution techniques. Using crystallography, the first crystal structure of integrin αVβ3 was published by Xiong *et al*. in 2001, showing an unexpected V-shape bent conformation in 2001[15]. Later, EM was utilized by some groups to probe integrin's conformations with nanometer resolution. For example, Springer's group at Harvard utilized negative stained EM to identify multiple conformations of integrins α5β1[115, 116], αIIbβ3[39, 117], αxβ2 and αLβ2[42]. All these integrins have been reported to be able to switch between bent and extended

conformations, like a switchblade, upon different extracellular or intracellular stimuli, such as RGD peptide, cations (Mn^{2+}), activating mAbs, signaling from other receptors (e.g., TCR or GPCR) and small allosteric molecules [39, 42], such as XVA143. XVA143 is believed to act on the MIDAS of the βA domain and to lead to the βA activation by swinging out the hybrid domain while preventing downward movement of the α7 helix in the αA domain and locking it in the close and low affinity state[14]. Once the integrin is extended, the ligand binding site of the top of the integrin would pivot away from the cell membrane by about 15nm for αA domain lacking integrin, such as α5β1, αvβ3 and αIIbβ3, or ~20nm for the αA domain containing integrins, such as αxβ2 and αLβ2, based on the EM studies [36, 39, 115, 116].

Since majority of integrins behave as mechano-chemical sensors, they could transmit both mechanical and biochemical signals bi-directionally across the cell membrane. External and internal mechanical forces are believed to be a very important regulator on changing integrin's conformations. For example, during leukocyte trafficking, shear stress could up-regulate αLβ2 and α4β1 integrin's adhesiveness to their ligands by changing integrin's conformations after the T lymphocytes received chemokine signals. Behaving like external forces, it has been postulated that internal forces from the myosin's pulling on the cytoskeleton might also be able to change αLβ2 integrin's conformations in order to activate them in the immunological synapse formation[18].

All previous experiments reported only static conformational states of integrins under stress-free condition, but the dynamic properties of these conformational changes and the way that external forces facilitate these transitions remain elusive. With the FRET technique, Chigave *et al.* detected population conformational changes of integrins α4β1

that were expressed on cells and reported some temporal information concerning $\alpha_4\beta_1$ integrin's conformational changes[118, 119], but their results were still collected in a stress-free environment, and the behavior of a single integrin under forces was still not clear. Here, using the BFP (Figure 8-1A), the interaction was directly measured between ICAM-1-Fc, mAb MEM83 or KIM127 coated on a probe bead and LFA-1 expressed on a Jurkat cell. As shown in Figure 8-1A, a Jurkat cell was aspirated on a micropipette driven by the PZT to approach and contact the probe bead that was covalently linked with ICAM-1. The processes of the dynamic transitions of LFA-1 integrin between extended and bent conformations on living Jurkat cells were demonstrated by the force-independent position changes of the BFP probe beads, by the frequencies at which of these changes are modulated by cations (e.g., Mn^{2+} and Mg^{2+}, small allosteric molecule, XVA143, and different antibodies (e.g., mAb KIM127 or MEM83), and by the mechanical analysis on LFA-1-ICAM-1 complexes in the above conditions. Our results showed that the observed mean distance change of LFA-1's extension was about 18nm, while that of contraction was about 14nm. Finally, the way the external forces facilitated the extending and contracting processes was characterized by the BFP.

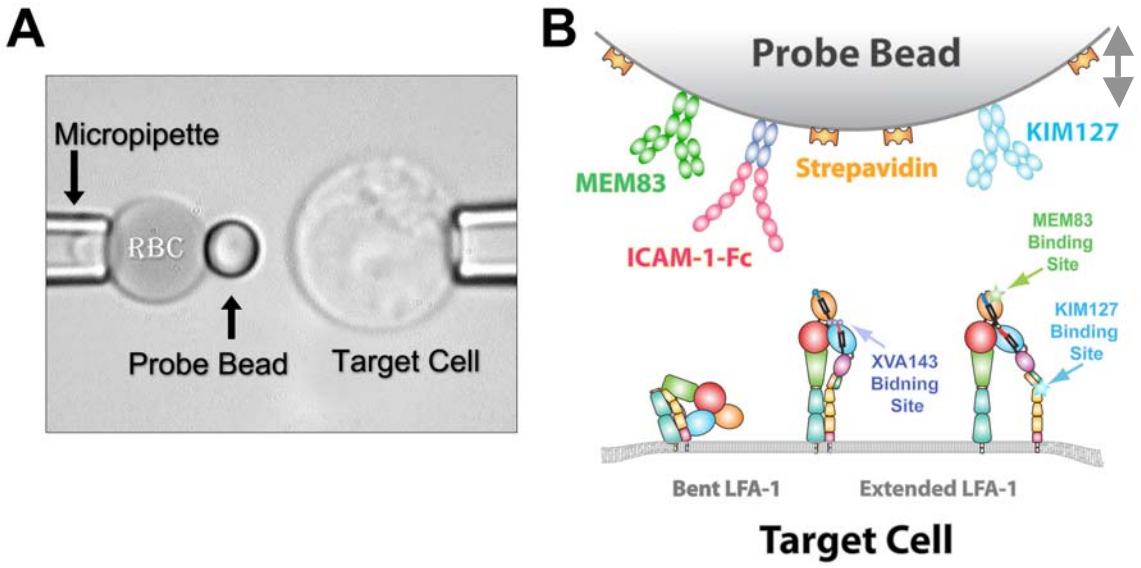

Figure 8-1. Photo micrograph of the Bio-membrane force probe (BFP). A micropipette-aspirated biotinylated RBC with a bead (probe) glued to its apex (*left*) was aligned against a cell (target) aspirated by a target micropipette (*right*). B) Functionalization of the BFP. ICAM-1-Fc, mAbs KIM127 or MEM83 were covalently linked on the streptavidin-coated probe bead via maleimide-PEG3500-NHS hetero-bifunctional polymers. LFA-1 integrins with bent or extended conformations were expressed on the target cell. KIM127's binding site on a LFA-1(light blue star) is on the genu site of the LFA-1's β subunit. Allosteric small molecule (XVA143, dark blue balls) binds to the LFA-1's βA domain, induces LFA-1's extended conformations, but locks the αA domain in close conformation and low affinity state. The probe bead moved up and down, indicated by a double headed arrow next to it.

8.2 Results

8.2.1 Observations of the upward and downward movements of the probe beads after the PZT stopped

Using the BFP to measure the LFA-1/ICAM-1 interaction, we observed unusual upward and downward movements of the probe bead at different force levels (Figure 8-1B). Since our results showed that the distances of these movements seemed to be narrowly distributed in a 20 nm range, we hypothesized that these position changes of the probe bead might result from the global conformational changes of LFA-1. To test this hypothesis, the distance distributions of the probe bead's upward and downward movements were firstly characterized at different levels of binding forces, and the occurrence frequencies of these movements at different modulating conditions were also measured.

In order to probe these position changes of probe beads, the BFP was run at a distance-clamp mode. In this mode, the target pipette, holding the LFA-1 expressing cells, was driven to approach to and then contact the ICAM-1 (or other mAbs, e.g., MEM83 or KIM127) coated probe bead; it was then retracted away from the probe bead to a certain distance, and held at that position for ~30s. Since the target cell's position was clamped, any distance changes between two surfaces linked by a molecular bond could possibly result in upward or downward movements on the probe bead. After the distance-clamp phase, the target pipette was fully retracted back to the initial position, and the BFP recovered to the unstressed state. Repeating this cycle many times, the occurrence frequencies of the upward and downward events of probe bead's position changes were measured. In order to ensure the measurements at single molecule level, the adhesion

frequencies were kept lower than 15%~20%.

To acquire the distances changes of these upward and downward movements, the plots of the displacements of the probe bead movements as a function of time (Figure 8-2 A and C) were carefully analyzed. The first type of position change of the probe bead was an increased displacement, so-called upward movement; that is, the probe bead was moving up after the PZT stopped. This upward movement of the probe bead might indicate an extension of LFA-1, this speculation needed further investigation. As shown in Figure 8-2A, after the PZT stopped, the position of the bead was at 40nm for about 0.1 second, and it was then suddenly increased by ~21nm. This position change of the probe bead resulted in a ~7pN force drop from ~35pN (Figure 8-2C). Contrary to the first type of position changes, the other type of observed position change was of a decreased displacement, so-called downward movement, that is, the probe bead moved down after the PZT stopped. As shown in Figure 8-2 B and D, initially the LFA-1-ICAM-1 bond was loaded to ~20pN (Figure 8-2D), and then the position of the probe bead moved down ~16nm (Figure 8-2B) after the PZT stopped. This downward movement of the probe bead resulted in ~7pN force increment from ~18pN (Figure 8-2D).

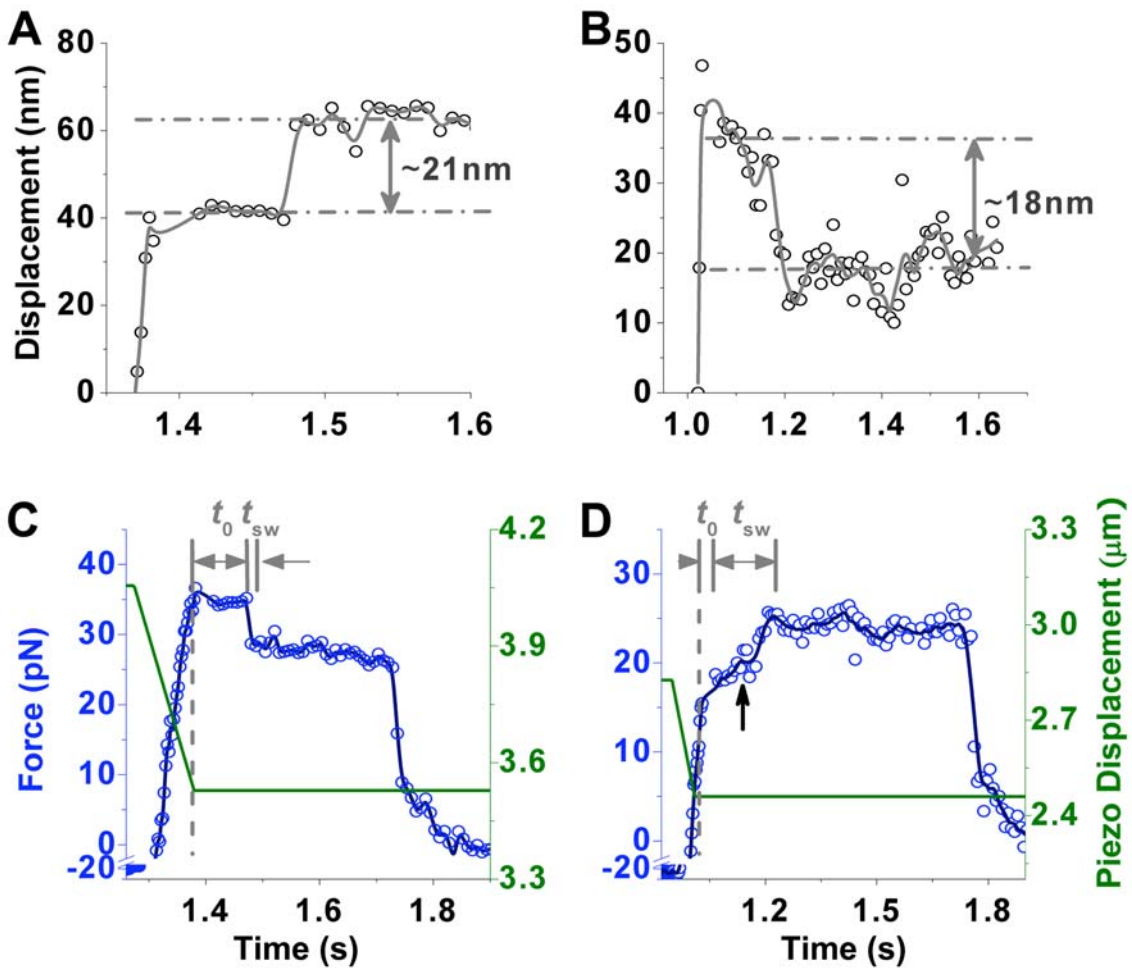

Figure 8-2. Experimental observations of abrupt position changes of the probe bead after the PZT stopped. Plots of the position as a function of time (grey circle), showing that the probe bead move up 21nm (A) or move down in ~18 nm (B) after the PZT stopped. The solid gray curve is the smoothed plot of extension vs. time curve. C)-D) Plots of the binding forces measured by the BFP (blue circle) as a function of time, showing force decreases (C) or increases (D) after PZT-driven target pipette stopped (the moment is marked by vertical, dashed and grey line). The solid blue curve is the smoothed force-vs.-time plot. After the PZT stopped, time to force-drop (D) or time to force-increase (D) and the switching time are defined as t_0 and t_{sw} respectively.

8.2.2 Statistical analysis of probe beads movements reveals integrin's global conformational changes

To further investigate whether these upward and downward movements of the probe beads were indeed caused by the global conformational changes of LFA-1 integrins, a series of experiments and statistical analyses were carried out to test this hypothesis. Firstly, the impact of binding force on these up and down movement was characterized. As shown in Figure 8-2, that distance changes of upward and downward movements were narrowly distributed as Gaussian around 18nm±3nm (SD) and 14nm±4nm (SD) respectively (Figure 8-2 C and D), and they were independent of the binding forces between LFA-1 and ICAM-1 (Figure 8-2 A and B). Since the distances of these movements were much shorter than cellular movements, which should be hundreds of nanometers, it was reasonable to exclude the possibility of cellular movement. Furthermore, the force-independent displacements of these movements suggested that these movements were not caused by the membrane tether extrusion, for the extrusions were strongly dependent on pulling forces [120].

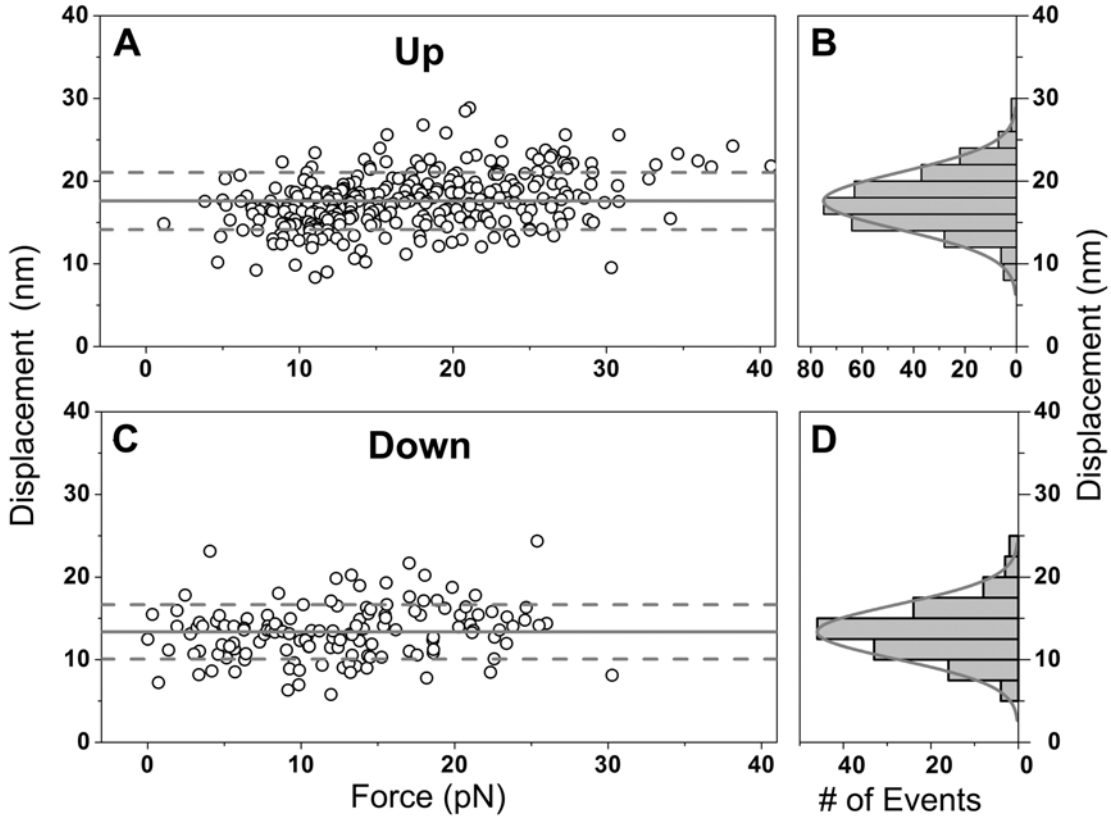

Figure 8-3. **Scatter plots of position changes of the probe bead upward movements (A) or downward movement (C) after the PZT stopped versus force.** These two plots show that the displacements of position changes of BFP's probe beads were not dependent on binding forces between LFA-1 and ICAM-1. The average of the position changes of upward or downward movements of the probe bead (solid line) and one σ standard deviation (dashed lines) are superimposed on the scatter plots. On left side of each scatter plot is the corresponding histogram of the position changes fitted with Gaussian distribution (solid grey line) (B, D).

To further exclude the possibility that these movements were caused by the cell's motions, the same experiments were repeated on three different types of cells (K562, PMN and Jurkat cells). All of these cells expressed LFA-1 integrins. If these movements indeed were caused by LFA-1's conformational changes, the distances of probe bead's movements should be consistent on all of three different cells. Comparison of data collected from three different types of cells showed that the mean distances of upward and downward movements of the probe bead were statistically similar on all of the three different cells (Figure 8-4). This similarity strongly suggested that these upward and downward movements were not dependent on cell types but were more likely dependent on adhesion molecules, LFA-1. Thus, these cell types' independent and force-independent position changes of the probe beads with narrow distributions around 10~20nm ruled out the possibility of cell movements and also supported our hypotheses that these displacements more likely were molecular behaviors. The most likely candidate was integrin's conformational changes, as the displacement changes of upward and downward movements fit very well in the range of LFA-1's conformational changes, 15nm~20nm, observed by EM [42].

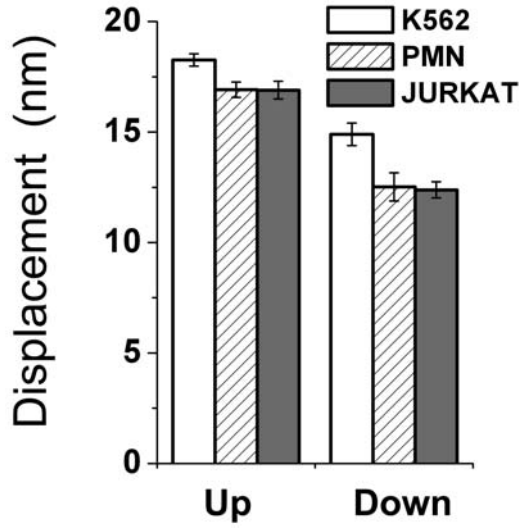

Figure 8-4. Comparison of the mean displacements of upward or downward movements of the BFP probe bead. The probe bead coated ICAM-1 were tested with three different types of cells (K562, PMN and Jurkat cells), and all of them expressed LFA-1, Error bars represent S.E.M..

If these upward and downward movements of probe beads were indeed caused by LFA-1's global conformational changes, the occurrence frequencies of these movements should be dependent on the stimulating conditions, which could cause LFA-1 integrins to switch to different conformations. To test this hypothesis, firstly, occurrence frequencies of upward and downward movements of the ICAM-1 coated probe bead were measured at 2mMMg^{2+}/EGTA or 1mM Mn^{2+} condition. Our data showed that the occurrence frequency of the downward movements of the probe beads at the Mn^{2+} condition was statistically greater than that at 2mMMg^{2+}/EGTA, while the occurrence frequency of upward movements was very similar (Figure 8-4A). Related to published data [39, 42] that Mn^{2+} could greatly shift inactive and bent integrins to extended conformations, our

data suggested that the differences of the occurrence frequencies of downward movements should be caused by changing cations, Mg^{2+}/EGTA to Mn^{2+}, and these differences clearly implied that the movements of the probe bead were very possibly resulted by LFA-1's global conformational changes.

Instead of using LFA-1's ligand, ICAM-1, to probe the probe bead movements, anti-LFA-1 mAb was next used to test with forces whether these antibodies could also induce LFA-1 conformational changes, which would then result in the probe bead's movements after the PZT stopped. Two antibodies were utilized, one was mAb MEM83, binding to LFA-1's αA domain[111, 121], and the other one was mAb KIM127, which binds to the genu region of LFA-1's β subunit only when LFA-1 adopts the extended conformation[111] (Figure 8-1B). Because the binding sites of these two mAbs on LFA-1 were different, we hypothesized that using MEM83 mAb coated beads to probe cells should result in similar upward and downward movements on probe beads as those movements observed by ICAM-1 coated probe beads, while KIM127 should not. As shown in Figure 8-5, our data clearly showed that with the MEM83 coated probe bead, not only were upward and downward movements of probe beads observed after the PZT stopped, but also the occurrence frequency of these movements depended on the cations in the solution. Figure 8-5A showed that Mn^{2+} raised the occurrence frequency of upward movements compared to that at the Mg^{2+} condition when the MEM83 coated bead was used. However, the occurrence frequencies of such movements dropped to almost zero and were not affected by changing metal ions when the KIM127 probe bead was used (Figure 8-5A). This was reasonable, because the KIM127's epitope is located on the genu region, so the global conformational changes should not affect its position. Unlike

KIM127's epitope, MEM83's is located on the αA domain so that the global conformational changes of LFA-1 could induce its upward or downward movements. Thus, the results of using mAbs MEM-83 or KIM127 probe beads strongly supported our hypotheses that the upward and downward movements of the probe bead was caused by the large scale, switchblade-like globe conformational changes of LFA-1.

More interestingly, the binding of the small allosteric molecule (XVA143) to LFA-1 suppressed the occurrence frequencies of probe bead's movements. It was believed that XVA143, binding to βA domain, could extend LFA-1 integrins to the straight conformation[14]. The same distance clamped experiments were run at different incubating conditions for Jurkat cells; that is, all Jurkat cells were incubated with 1mM Mn^{2+} and XVA143 at varied concentrations from 0 nM to the saturating condition of XVA143, 1000 nM. Our data showed that at the condition of 1000 nM XVA143, upward and downward movements of the probe bead did not occur at all (Figure 8-5 B). According to the XVA143's functions, this abolishment suggested that XVA143 not only extended the majority of LFA-1 integrins, but also locked them at extended conformation so that it abolished LFA-1's ability to bend back. However, when XV143's concentration was gradually reduced to 0 nM, the occurrence frequencies of upward and downward movements of probe beads gradually recovered to the level where no XVA143 was found but only 1mM Mn^{2+} (Figure 8-5B). This XVA143-dose-dependent occurrence frequency clearly showed that the reduction of the XVA143 caused upward and downward movements of the probe beads more frequently. It is reasonable to speculate that recovery of these movements were caused by the recovery of LFA-1's dynamic global conformation when XVA143 was reduced, since different doses of XVA143 could shift

different amounts of LFA-1s to extended conformation and could lock them to different extents. Therefore, combined with distances data and occurrence frequencies data, these observed movements of the probe beads were very likely caused by global conformational changes of LFA-1 integrins. Therefore, the upward movement of the probe might reflect LFA-1's extension from the bent state, while the downward movement might indicate LFA-1's contraction from the extended conformation.

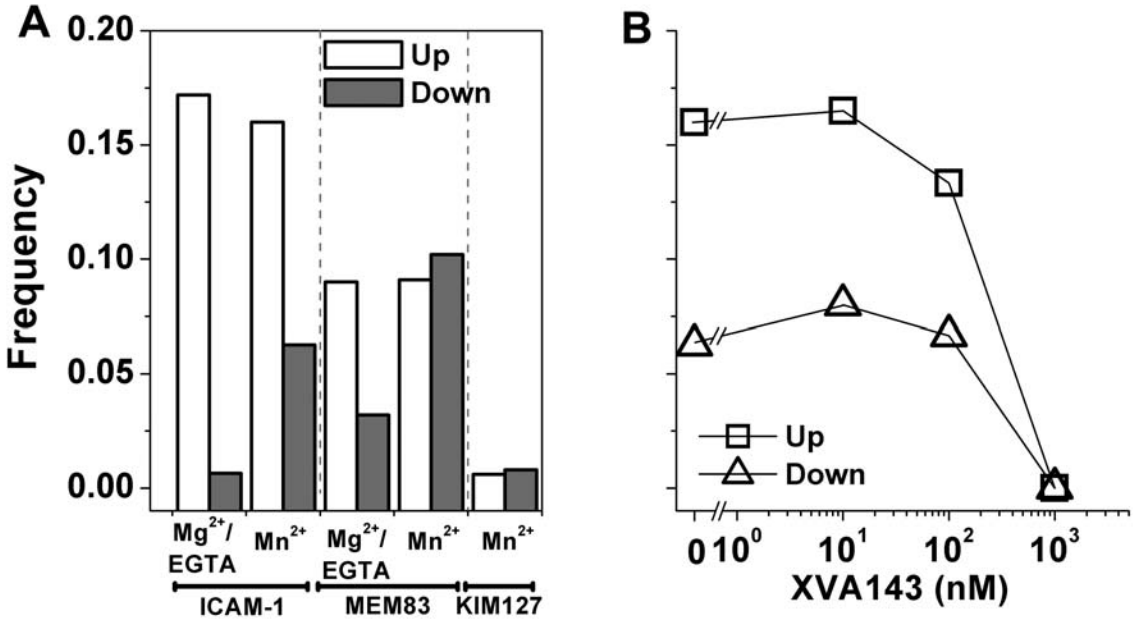

Figure 8-5. Comparison of occurrence frequencies of upward and downward movements of probe beads. A) Comparison of the occurrence frequencies of upward or downward movements of the BFP probe bead between LFA-1 integrin and its ligand (e.g., ICAM-1) at different conditions (2mM Mg^{2+}/EGTA, 1mM Mn^{2+}) or between LFA-1 and mAbs MEM83 (at 2mM Mg^{2+}/EGTA or 1mM Mn^{2+}) or KIM127 (at 1mM Mn^{2+} plus 100μg/ml sICAM-1). B) XVA143's dose-dependent occurrence frequencies of upward or downward movements of the BFP probe beads. XVA143's does ranges from 0 nM to 1000 nM.

8.2.3 Mechanical analysis further confirmed the observed conformational changes of LFA-1 integrin

The above analysis of the distances and occurrence frequencies of the probe beads' movements have strongly suggested the possible observations of dynamic and switchblade-like conformational changes of LFA-1. To further reinforce that these observations were dynamic switches of LFA-1, the mechanical stiffness of LFA-ICAM-1 complex different conditions was next analyzed, as bent and extended integrins may be of different stiffness. The method used to measure molecular spring constants was the stretching method [122], by which the slope of the ascending phase (Figure 8-6, blue or red dashed line) of force vs. molecular extension plot (Figure 8-6) was measured. Two segments were presented in the ascending phase, as shown in Figure 8-6. During the BFP's impingement, linear fitting on the slope of the ascending phase (red dashed line, Figure 8-6) provides the cellular stiffness, k_c. Our results showed that the average cellular compliance was around 0.25 pN/nm at the condition of 1mMMn^{2+} and 0.2 pN/nm at the condition of 2mM Mg^{2+}/EGTA. After binding force occurred, linear fitting in the ramping phase provided the effective compliance k_{eff}, the product of two springs in series. These two springs consisted of the spring (k_m) of the LFA-1-ICAM-1 complex and the spring (k_c) from the cell. Since these two springs were in series, they had the following relation,

$$1/k_{eff} = 1/k_m + 1/k_c \,, \qquad \text{Equation 8-1}$$

With Equation 8-1, k_c could be calculated, given k_m and k_{eff}.

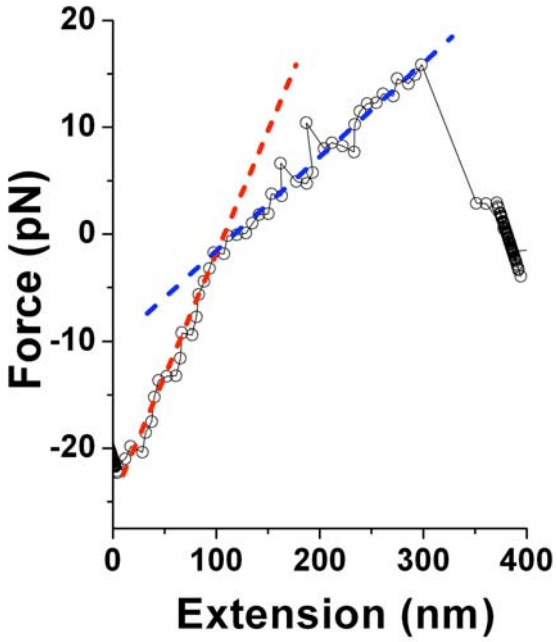

Figure 8-6. Plot of force vs. extension for measuring molecular compliance. The slope of red dashed line provides the cellular compliance k_c, while the slope of the blue dashed line provides the effective compliance (k_{eff}) which represents two springs in serial.

LFA-1-ICAM-1 complex's compliances were affected by the divalent cations. As shown in Figure 8-7, at the Mg^{2+} condition, the majority of the LFA-1-ICAM-1's spring constants tightly distributed below 0.5 pN/nm. While more than 70% of spring constants were smaller 0.25 pN/nm (Figure 8-7A, red solid fitting by Gaussian), and the rest were between 0.25 pN/nm and 0.5 pN/nm (Figure 8-7A, blue solid fitting by Gaussian). However, once the cations were switched to the 1mM Mn^{2+}, our data showed that both sub-populations of spring constants shifted rightwards to the stiffer side. The softer sub-population distributed around 0.25 pN/nm (Figure 8-7B, red dashed fitting by Gaussian), very close to that at Mg^{2+}/EGTA condition; while the stiffer one distributed around 1 pN/nm (Figure 8-7B, blue dashed fitting by Gaussian), becoming more pronounced than that in Mg^{2+}/EGTA condition. These shifts clearly corresponded to

metal ion changes and suggested that more LFA-1s adopting extended conformation at Mn^{2+} resulted the right shift of spring constant histogram. This data implied that extended integrin seemed much stiffer than a bent one.

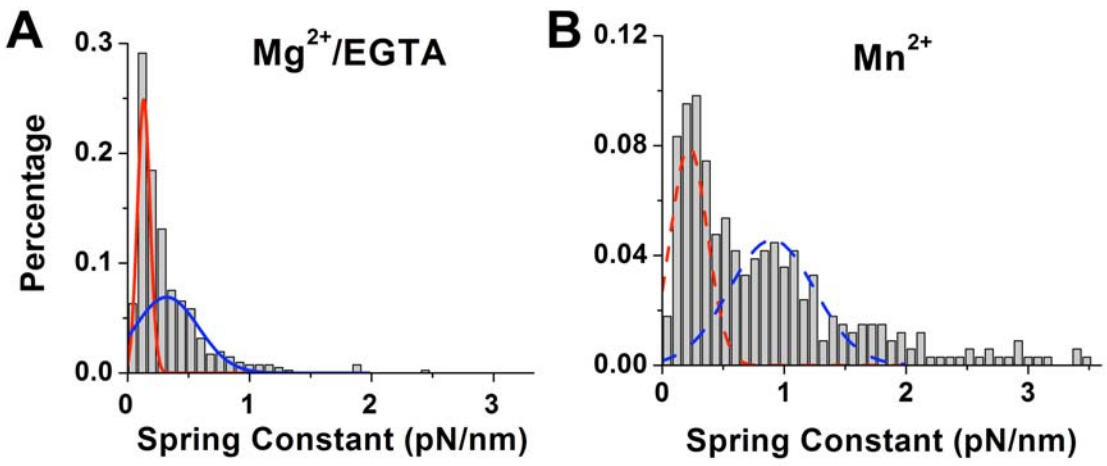

Figure 8-7. Histograms of molecular spring constants of LFA-1-ICAM-1 complex at the condition of 2mM Mg^{2+}/EGTA (A) or at the condition of 1mM Mn^{2+}. Two sub-populations of the histograms were fitted by Gaussian distribution (red and blue solid line in (A) and dashed line in (B) respectively.

If extensions of LFA-1 could cause stiffening of LFA-1-ICAM-1 complex, adding various concentrations of XVA143 should also augment the stiffness of the complex to different extent. To test this hypothesis, the spring constants of LFA-1-ICAM-1 complex at the different concentrations of XVA143 were also characterized. As shown in Figure 8-8, the spring constants of LFA-1-ICAM-1 complex increased as the concentration of XVA143 was increased, strongly suggesting that the extended LFA-1 was stiffer than bent one. As a control, the spring constants of KIM127-LFA-1 complex were also measured. The results showed that this complex was even stiffer than LFA-1-ICAM-1 complex at the condition of Mn^{2+} plus 1μM XVA143. It is reasonable because of two

reasons, 1) KIM127 was a more compact protein than ICAM-1 so that KIM127 should be stiffer than ICAM-1, and 2) KIM127 bound to the genu of β subunit of LFA-1 so that the effective spring constant from the leg regimes of LFA-1 was stiffer than the whole of LFA-1, as the number of domains contributing to the complex stiffness was much less than that of whole LFA-1[122]. Therefore, these stiffness data strongly suggest that an extended LFA-1 is much stiffer than the bent one.

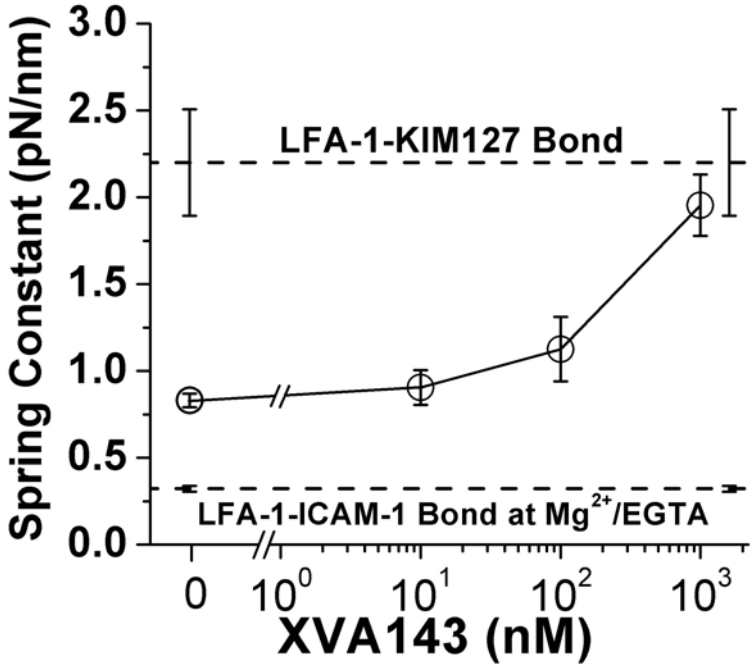

Figure 8-8. Plots of spring constants of LFA-1-ICAM-1 bonds versus XVA143's doses at the conditions of Mg^{2+}/EGTA (bottom dashed line), Mn^{2+} without or with different concentrations of small alloestric molecule, XVA143, and spring constants of LFA-1-KIM127 bonds at the conditions of 1mM $Mn^{2+}$and 100μg/ml soluble ICAM-1(upper dashed line). Error bars represent S.E.M..

Relating this stiffness data with previous data of probe bead's upward and downward movements, we thought that if bead's movements indeed were caused by LFA-1's global conformational changes, prior to the conformational changes, the stiffness of the LFA-1-ICAM-1 complex from the ramping phase should tell us whether the LFA-1 was bent or extended. Thus, two different groups of stiffness data were pooled together. One group of stiffness data was from the ramping phase prior to the probe bead's moving up, i.e., more likely extension of LFA-1, and the other ones were from the ramping phase right prior to the probe bead's moving down, more likely LFA-1's contraction. As shown in Figure 8-9, the majority of spring constants prior to upward movements of the probe beads were below 0.25 pN/nm and distributed around 0.16 pN/nm (gray histogram fitted by blue solid line), while those prior to downward movements of the probe beads were ~5 times stiffer and distributed around 1 pN/nm (yellow histogram fitted by red dashed line) (Figure 8-9). Since it has been known that an extended LFA-1 was stiffer than a bent one, these results strongly suggest that LFA-1 were bent prior to the probe bead's moving up which was caused by the extension of LFA-1, while LFA-1 was extended prior to the probe bead's moving down caused by the contraction of LFA-1. Thus, this stiffness analysis of the events of upward and downward movement of the probe bead further supported and strengthened our main hypothesis that these probe bead movements were indeed caused by LFA-1 global conformational changes.

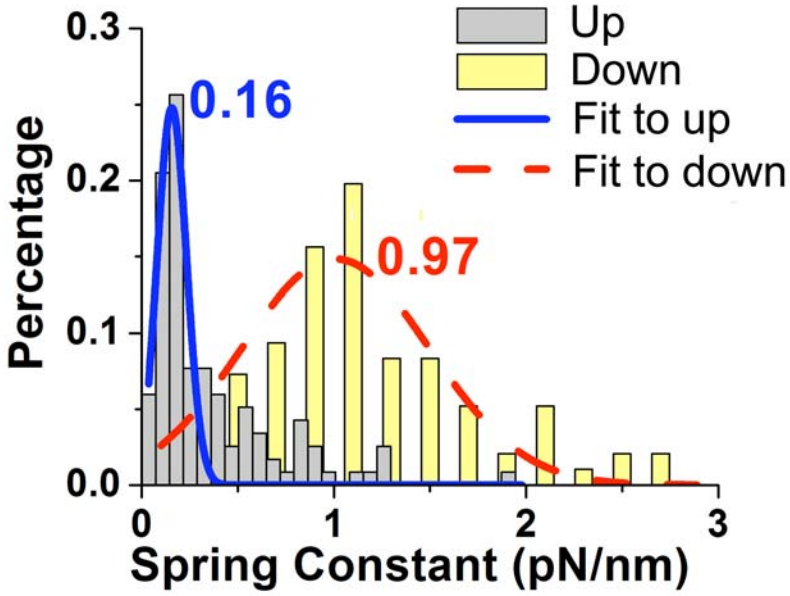

Figure 8-9. Histograms of molecular spring constants of LFA-1-1-ICAM-1 bonds of increased (gray) or decreased (yellow) displacements. Each histogram was fitted by different Gaussian distributions. The blue one (solid line) fits the histogram of increased displacements (gray), and the peak of this fitting is about 0.16 pN/nm. While the red one (dashed line) fits the histogram of decreased displacements (yellow), and the peak of this fitting is about 0.97 pN/nm.

8.2.4 Characterization of dynamic properties of global conformational changes of LFA-1

Having shown the *in-situ* observation of LFA-1 dynamic conformational changes, we next characterized the dynamic properties of LFA-1's transitions between different conformational states. Interestingly, our results showed that these dynamic transitions were dependent on the binding force exerted on the LFA-ICAM-1's bond but not on cell types. First of all, the average switching times of single LFA-1 from the bent state to the extended or from the extended to the bent were characterized. The switching time was defined as the time from the moment the extension change started to the moment the

extension change of the single LFA-1 ended, as shown in (Figure 8-2 A and C). As shown in Figure 8-10A, it was statistically significant that LFA-1 took much more time to contract back than to extend, and this difference was consistent on three different types of cells (K562, PMN and Jurkat cells). Similarly, a time to switch, defined as a time from the moment the PZT stopped to the moment the extension change of LFA-1 started, was also characterized. The results of times to switch suggested that LFA-1 took much more time to start contracting than to extend (Figure 8-10B). More interestingly, our results revealed that LFA-1 switching from the bent state to the extended state became faster as binding forces increased, while the contraction of LFA-1 from the extended conformation became slower as binding forces increased. Thus, these data strongly implied that switching times of conformational changes were strongly dependent on the binding forces exerted on LFA-1 integrin-ICAM-1 bond (Figure 8-10C). Especially over the threshold of 30 pN, the contractions events were rarely observed. This threshold implied that LFA-1 could overcome small external forces but not large forces to contract back, and that external forces could facilitate the LFA-1 switchblade-like extension and lock it in the extended conformation when forces are large enough..

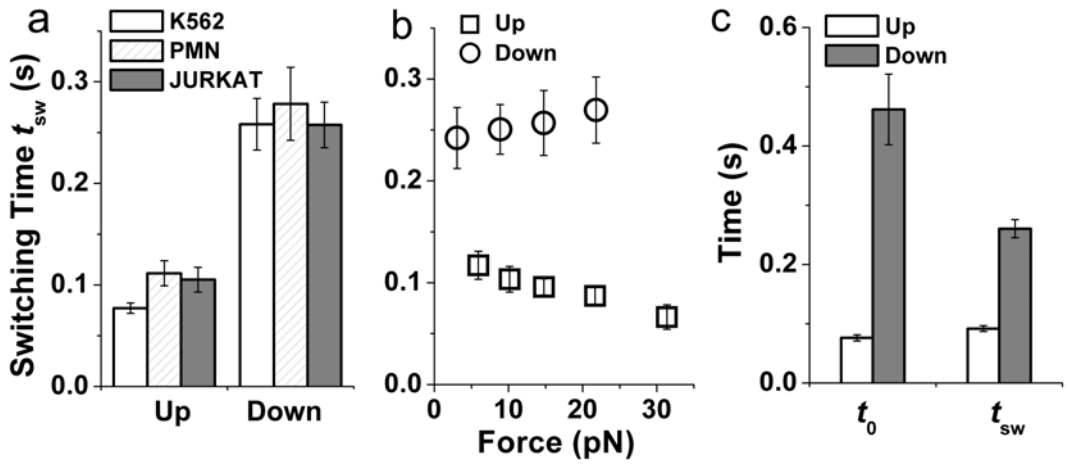

Figure 8-10. Characterization of the conformational changes of LFA-1 integrins. A) Plots of switching times of conformational changes of LFA-1 integrins as a function of binding force. B) Comparison of average switching times between extension or bent-back of LFA-1 integrins on K562, PMN and Jurkat Cells. Error bars represent S.E.M.. C) Comparison of t_0, time to conformational changes after the PZT stops between extensions or bent-back of LFA-1s on K562, PMN and Jurkat Cells. Error bars represent S.E.M..

8.3 Discussion

Dynamic switchblade-like conformational changes of integrins have been proposed for a few years[37]. But this model was only based on static EM images, crystal structures and antibody epitope's mapping under stress-free conditions. [15, 37, 39, 42, 123]. Our observation described previously was the first to provide a clear picture of how mechanical force regulates the dynamic process of integrin's conformational changes at the single molecular level on a living cell. Our findings greatly strengthen and extend the current framework of integrin's conformational changes.

Excluding possible cellular motions that may cause the probe bead's movements, to justify that our observations were indeed due to integrin's conformational changes was

very necessary, as a living cell is was a very complicated environment for studying receptor-ligand interactions at the single molecular level. Any motions on the cell surface, for example, tether extrusion by force or cell membrane polarization could bring tremendous noise into our system, which would greatly bias our judgments on the measurements. In order to ensure that our observations of upward and downward movement of the probe beads were essentially caused by LFA-1's conformational changes, we carried out a series of vigorous mechanical analyses on the molecular spring constants and statistical analysis on the distributions of probe beads' movements, on the mechanical force's effect, and on cations and XVA143's modulations on the probe bead's movements. Narrow distributions of distances changes of the probe bead's movements in 10~20nm ranges helped us to exclude cellular level motion. Force-independent displacements further ruled out the membrane tether extrusion.

In addition to the cellular motion, the dissociation of double LFA-1-ICAM-1 bond could also cause similar extension changes, especially force-down events. Because ICAM-1-Fc is a chimerical molecule, there was about 10% probability of forming two LFA-1-ICAM-1 bonds at the same time. In this case, the dissociation of one ICAM-1 from the target cell could cause the force-down events, which might be resulted from the 15nm molecular extension increment. This extension changes phenomenologically similar to LFA-1's unbending. However, our data can exclude this possibility. First of all, our force-up events do not favor the possibility of double bonds, since double LFA-1-ICAM-1 bonds could not be able to induce force-up event. Secondly, the occurrence frequencies of force-up and force-down events were really dependent on the metal ion conditions and XVA143's doses. This observation strongly does not favor the

double bond possibility. Moreover, the molecular stiffness analysis further weakens this possibility. Our data show that the LFA-1-ICAM-1 complex was much softer before force-drop events than before force-up events. If force-drop was caused by the dissociation of one arm of ICAM-1-Fc chimera from the target cell, there should be two bonds stretched in parallel. Thus, the molecular stiffness in this case should be stiffer than one bond case, such as force-up event. But our data exhibit an opposite scenario. Therefore, the double bond possibility is not supported by our data from multiple aspects.

Cations have been known for regulating LFA-1 integrin's conformations. They have been widely used in many experiments, such as EM studies for observing integrin's global conformational changes[39, 42] and flow chamber assays for studying integrin-mediated cell rolling and firm adhesion [113]. Mg^{2+}/EGTA and Mn^{2+} were well-known potent stimuli activating integrin's affinity. Mn^{2+} had also shown its strong ability to induce LFA-1's extension, while Mg^{2+}'s effect on that was still not very clear. According to our results, very few downward movements occurred at the Mg^{2+} condition, and this suggested that the majority of LFA-1 adopted the bent conformation, which was consistent with reported results[124] that exposure of KIM127's epitope at Mg^{2+} condition was very close to the basal level. However, LFA-1 still exhibited strong binding to its ligand ICAM-1, which suggested that at the Mg^{2+} condition LFA-1 adopted a bent conformation with open headpiece caused by the hybrid domain's swing out [36, 114] and open MIDAS caused by the downward movement of α7 helix in αA domain [12, 114]. While upon Mn^{2+} activation, our occurrence frequencies and mechanical analysis results strongly suggested that large sub-population of LFA-1 integrins shifted to the extended conformation. The contraction events of LFA-1 at this condition suggested that

even though Mn^{2+} could shift more LFA-1 to extended conformation, for individual integrin, it still kept dynamically switching between bent and extended states so that we were able to observe those contraction events. This dynamic switching was so called "breath" has already predicted a few years ago by Salas *et al.* [113].

Antibody epitope exposures have been widely used to determine the extension of integrins. So reporting mAb KIM127 was also utilized to probe LFA-1's extension changes. Since the epitope of KIM127 was not affected by the swing out of the headpieces of LFA-1, KIM127's probing could provide a very meaning clue to inspect the LFA-1 conformational changes. However, the binding of KIM127 to LFA-1 was detected only when LFA-1 inegrins were activated by 1mM Mn^{2+} and 100μg/ml sICAM-1 but very weakly by Mg^{2+}. This activation requirement suggested that outside-in signaling by Mn^{2+} and sICAM-1 were potent enough to extend LFA-1 integrins. Further, no upward or downward movements occurred when using KIM127 coated probe beads to probe LFA-1. This observation was exactly as we expected and was also very reasonable, as the epitope of KIM127 is in the genu region, and no large-scale displacement on this epitope could be caused by the global conformational changes of LFA-1. However, mAb MEM83's probe behaved differently from KIM127's. Since MEM83's epitope is located on the αA domain at the top of LFA-1, once LFA-1 changed its conformation, the epitope would move along with the headpiece. Our MEM83's data clearly supported this idea. Furthermore, since MEM83 was an activating antibody, it could activate integrins to a high affinity state accompanied by the extension of LFA-1[125]. That was why we observed some contraction events even at Mg^{2+} condition. While the occurrence frequencies of extending LFA-1 when using MEM83 beads were lower than those when

usingICAM-1 bead, this may imply that LFA-1 ligand, ICAM-1, was more potent on regulating LFA-1's conformations.

The binding of the small allosteric molecule, XVA143, to LFA-1 has been known for extending LFA-1 but for locking the αA domain in a close and low affinity state. In the proposed model of XVA143, the allosteric function was that its binding to the MIDAS in the βA domain resulted in extending LFA-1, opening the headpiece by swinging out the hybrid domain but locking the αA domain in a close conformation. This locking function was performed by preventing the downward movement of the α7 helix and blocking Glu127 at the end of the α7 helix to the βA MIDAS [14, 42]. Our spring constant data strongly suggested that the majority of LFA-1 extended upon 1μM XVA143's binding, and our occurrence frequencies data suggested that XVA143 could strongly lock LFA-1 in the extended conformation and almost abolish LFA-1's ability to dynamically switch between bent and extended states. The mean spring constant of LFA-1-ICAM-1 complex became softer, and the occurrence frequencies gradually recovered as XVA143's doses were reduced. This XVA143's dose dependent spring constant of LFA-1-ICAM-1 complex further indicated that the extended LFA-1 was stiffer than the bent ones. The possible reason for this was that the headpiece of LFA-1 was more flexible when LFA-1 was bent than when it was extended. With this observation, we further confirmed that LFA-1 was bent prior to the abrupt upward movement of the probe bead, while it was extended prior to downward movement of the probe bead.

Force facilitating LFA-1 conformational change has been proposed in other published papers, based on indirect observations[18, 41]. Our experiment was the first one to directly demonstrate this dynamic processes of LFA-1 conformational changes

in-situ and was the first one to clearly depict that how force regulated these dynamic processes. The contraction of LFA-1 only occurred more frequently in the low forces and became less frequent as binding force increased. As well, it was reasonable that the contraction process took much more time than the extension process, as LFA-1 needed to overcome the binding forces in the contraction process, unlike the extension process. The extension was actually facilitated by the binding forces. Furthermore, the observed switching times were very similar on three different cell types and also fell in the predicted sub-second range[18, 124]. This similarity further showed that these abrupt movements of probe beads were not caused by cellular movements but by molecular conformational changes.

However, the energy source that drives the bending of LFA-1 integrin is still not clear. The energy barrier for the LFA-1 to bend back is about 150 nm•pN (about 40 k_BT at RT), which is very large. Thermal energy in the environment could not be large enough to drive this bending process. Thus, there must be other energy source to drive this process. One possible energy source is from the non-muscle myosin II. It may somehow regulate the tail of LFA-1 integrins through a series adapter protein, such as talin. To test this hypothesis, we can treat cells with blebbistatin or myosin light chain kinase inhibitor, ML-7, to inhibit myosin's activity.

The *in-situ* probing of dynamic switches between different conformations of LFA-1 integrin is not only consistent with previous multiple static conformations of purified integrin observed by EM[39, 42], but also for the first time clearly depicted a dynamic process of how αA containing integrin switched between bent and extended states under external forces. These data also confirmed the prediction that force facilitates the integrin

extension but slows down the contraction process, and it accurately showed how fast these switches were under stress conditions. Force-dependent conformational changes of integrin may provide molecular mechanisms to explain the catch bonds in integrin/ligand interactions. Contraction of integrins under external or internal forces could provide some cues to understand how the immunological synapse forms and how LFA-1's contraction helps T-cell receptors to overcome the distance limit to interact MHC peptide on the antigen presenting cell[126]. As well, these force-dependent observations and contractions may provide a molecular mechanism to explain how integrins' conformational changes allow cells to sense the substrate stiffness, and therefore affect cell behaviors, such as migration, differentiation, and other cellular functions[18, 126, 127].

CHAPTER 9

RECOMMENDATIONS FOR FUTURE WORKS

The most exciting element of fundamental scientific research is that numerous interesting topics and questions always pop out during the exploration of current questions. In the preceding pages, a new thermal fluctuations assay was developed to estimate 2D on rates and off-rates of the interactions between surface-anchored molecules; experiments revealed the structural basis for force and force history dependent catch bonds in selectin/ligand and LFA-1/ICAM-1 bonds and depicted dynamical conformational changes of LFA-1 on a living cell.

However, using only force as a tool to probe biological interactions is not enough; we should combine other techniques, such as fluorescence, with the BFP to study cellular behavior inside the cell. It is said that fluorescence is the “King” in biological research. A few months ago, the 2008 Nobel Prize in chemistry was awarded to three major scientists for their contributions on green fluorescence protein (GFP). From this award, we can clearly see that how huge the impact of fluorescent techniques is on biological research. If fluorescent techniques, such as biosensor techniques and FRET, could be combined with the BFP, the new version of the BFP would be more powerful to directly *in-situ* observe how mechanical force regulates surface molecules’ clustering, molecular conformational changes and downstream signaling cascades. It would reveal a very intriguing movie of molecular interactions on membranes and inside of cell membranes. Furthermore, if the BFP could be combined with a single molecule tracking technique,

individual molecules' behavior under mechanical forces would be clearly viewed by high resolution single molecule tracking. Therefore, a combination of the BFP with fluorescent techniques would open a very challenging but extremely interesting area of mechano-biology, the curtain of which has started being raised up [128, 129].

The newly developed thermal fluctuation assay adds a new tool to scientist's toolbox for studying receptor-ligand interactions. But this new tool still can be improved for studying more complicated problems, such as better estimation of the 2D kinetics of receptor-ligand interactions. For example, since distances between two surfaces affect 2D on-rates measurement very much, adding one more edge tracking on the target pipette side would provide a more accurate estimation of these distances. Further, drifting of the BFP would cause tracking errors; thus, adding feedback control system to compensate for drifting would be very helpful for measuring receptor-ligand interactions with slow dissociation or association (i.e., waiting times or lifetimes > 2 minutes). One more important improvement is to limit the rotation of the probe bead, since this rotation could bias the 2D on-rate very much. For reference, a new laser trap [130] developed by Volkmar *et al.* used trap energy to limit the rotation of the tracked bead. Finally, it would be very useful study multi-receptors' cooperation (e.g., cooperation between selectin and integrins or T cell receptor and CD8/CD4) if we could improve the sensitivity of thermal fluctuation to discriminate different types of molecular bonds based on the reduction of thermal fluctuation.

Developments of new techniques always could greatly advance scientific research, but the central core of scientific research is to understand the essence of the unknown world. Biology is an old field, but the majority of this field remains unexplored. Related

with the biological questions studied in previous chapters, more research could be carried out to extend our understanding of selectins and integrins.

The structural basis of the on-rates and force, force history dependent off-rates of selectin-ligand interactions is still not very clear. The sliding rebinding model has already predicted that flexibility of lectin domain can enhance the intrinsic on-rate of a selectin to its ligands. This prediction has been partially supported by flow chamber data[53]. It would be more interesting to use the thermal fluctuation assay to directly measure the 2D on-rate at the single molecule level. If this model is correct, can mutating P-selectin hinge to L-selectin? Will this mutation greatly suppress P-selectin's on-rate and augment off-rates in low forces? Will this mutation affect P-selectin mediating leukocyte rolling on PSGL-1 coated surfaces? Another important question is about the mechanism of force history dependent off-rates of L-selectin/ligand interactions. Our results showed that only L-selectin/PSGL-1 but not L-selectin/6-sulfo-sLe^x interaction was affected by force-loading rates. What is the structural basis for this difference? The direct answer would be that PSLG-1's binding sites are different from 6-sulfo-sLe^x. PSGL-1's binding including both the peptide interactions and the sugar interactions that 6-sulfo-sLe^x only has. What if a mutation to the L-selectin binding pockets abolishes the PSGL-1's peptides binding? Will it abolish the force-history effects?

Compared to selectins, integrins' functions are more complicated and seem to present more interesting questions to be addressed by experimental works in future. First of all, LFA-1 has been known to be activated by E-selectin (Zhang *et al.* unpublished data) through an inside-out signaling pathway. But, how fast can the signals be transmitted from the moment of E-selectin's binding to the moment of activating LFA-1? It might be

possible to use improved thermal fluctuation assay (described at the beginning of this chapter) to discriminate the E-selectin binding and LFA-1 binding so that we could characterize dynamic process (i.e., waiting times measurements) between these two different bindings. These waiting times may provide useful dynamic information about E-selectin's activation on LFA-1. Other than this dynamic information, spatial activation of E-selectin on LFA-1 is another interesting topic. Whether E-selectin‘s activation on LFA-1 is global or local is still not clear. If we have the new techniques of combining the BFP with fluorescence detection and biosensors, we would be able to clearly view the dynamic process of LFA-‘s activation by E-selectin and to reveal whether this activation occurs globally or locally. Meanwhile, the same experiments can be applied to study chemokine's activation on LFA-1 to better understand the whole process of how fast and how spatially chemokine activates LFA-1 and communicates between these two receptors, and also to explore the force regulated cross-talk between LFA-1 and TCR or any two cooperating membrane molecules.

This thesis has studied how force regulates integrin/ligand interactions, but how force regulates integrin's clustering on cell membrane is still not clear. With fluorescence techniques and the BFP, it would be very possible to dissect this interesting issue. It would be very useful to view the dynamic process of the clustering of integrins under stress. This proposed force regulated integrin's clustering may provide a molecular mechanism to explain the force regulation on LFA-1 mediated leucocytes adhesiveness to substrates through avidity regulation.

Dynamic conformations of LFA-1, especially contractions of LFA-1, have been observed in this thesis work. The extension of LFA-1 is known to regulate LFA-1 to a

high affinity state, while the physiological significance of the contractions is still not very clear. One possible explanation of the contraction may be recovering LFA-1 to its resting state. But a more interesting hypothesis is that LFA-1's contraction can help cells to sense the substrate rigidity by transmitting mechanical forces inside the cell through the cytoskeleton, and also can shorten the distance between TCR and MHC molecules to facilitate their interactions during immunological synapse formation. To test these hypotheses, a simple experiment is to use XVA143 to lock LFA-1 in extended conformation and then to test the cell's responses to different substrates of varied stiffness and to examine whether this addition of XVA143 would slow down the immunological synapse formation. Or we could mutate LFA-1 on the region between headpiece and leg domains to lock LFA-1 in either bent or extended conformation, and we could then test this mutation's effect on cell's rigidity sensing and immunological synapse formations.

The last but not the least, in a broader context, involves the automation of biological research with the assistance of computer-related technologies and program-controlled machines. Automation is very necessary to advance bioscience exploration in a very highly efficient and high-yield manner. Microarrays and DNA and protein chips are very good examples. However, in the 21st century, too much labor is still wasted in bioscience research by repeating low level procedures which could be completely done by program-controlled "robotics". By doing so, researchers could be released from time-consuming and boring bench tasks, and they could pay more attentions to hard thinking of scientific problems and to designing smart experiments to investigate these problems.

The sooner this day comes, the sooner human beings may disclose the buried secrets of biology; the sooner this day comes, the sooner we may be able to conquer fatal diseases to save numerous precious lives; the sooner this day comes, the sooner we may benefit from these fundamental bio-scientific research to improve our life. I hope this day comes soon!!

REFERENCES

1. Springer, T., *Traffic signals for lymphocyte recirculation and leukocyte emigration: the multistep paradigm.* Cell(Cambridge), 1994. **76**(2): p. 301-314.
2. Ley, K., C. Laudanna, M. Cybulsky, and S. Nourshargh, *Getting to the site of inflammation: the leukocyte adhesion cascade updated.* NATURE REVIEWS IMMUNOLOGY, 2007. **7**(9): p. 678.
3. McEver, R., *Leukocyte interactions mediated by selectins.* Thromb Haemost, 1991. **66**(1): p. 80-7.
4. MCEVER, R., *SELECTINS.* Current opinion in immunology, 1994. **6**(1): p. 75-84.
5. McEver, R., *Selectins: lectins that initiate cell adhesion under flow.* Current Opinion in Cell Biology, 2002. **14**(5): p. 581-586.
6. McEver, R., J. Beckstead, K. Moore, L. Marshall-Carlson, and D. Bainton, *GMP-140, a platelet alpha-granule membrane protein, is also synthesized by vascular endothelial cells and is localized in Weibel-Palade bodies.* Journal of Clinical Investigation, 1989. **84**(1): p. 92.
7. Graves, B.J., R.L. Crowther, C. Chandran, J.M. Rumberger, S. Li, K.-S. Huang, D.H. Presky, P.C. Familletti, B.A. Wolitzky, and D.K. Burns, *Insight into E-selectin/ligand interaction from the crystal structure and mutagenesis of the lec/EGF domains.* Nature, 1994. **367**: p. 532-538.
8. Somers, W.S., J. Tang, G.D. Shaw, and R.T. Camphausen, *Insights into the molecular basis of leukocyte tethering and rolling revealed by structures of P- and E-selectin bound to SLe(X) and PSGL-1.* Cell, 2000. **103**(3): p. 467-479.
9. Leppänen, A., S.P. White, J. Helin, R.P. McEver, and R.D. Cummings, *Binding of glycosulfopeptides to P-selectin requires stereospecific contributions of individual tyrosine sulfate and sugar residues.* J Biol Chem, 2000. **275**(50): p. 39569-39578.
10. Leppänen, A., T. Yago, V.I. Otto, R.P. McEver, and R.D. Cummings, *Model glycosulfopeptides from P-selectin glycoprotein ligand-1 require tyrosine sulfation and a core 2-branched O-glycan to bind to L-selectin.* J Biol Chem, 2003. **278**(29): p. 26391-26400.
11. McEver, R.P., *A sulfated address for lymphocyte homing.* Nat Immunol, 2005. **6**(11): p. 1067-1069.
12. Luo, B., C. Carman, and T. Springer, *Structural basis of integrin regulation and signaling.* Annu Rev Immunol, 2007. **25**: p. 619-47.
13. Hynes, R.O., *Integrins: bidirectional, allosteric signaling machines.* Cell, 2002. **110**(6): p. 673-87.
14. Shimaoka, M. and T.A. Springer, *Therapeutic antagonists and conformational regulation of integrin function.* Nat Rev Drug Discov, 2003. **2**(9): p. 703-16.

15. Xiong, J.P., T. Stehle, B. Diefenbach, R. Zhang, R. Dunker, D.L. Scott, A. Joachimiak, S.L. Goodman, and M.A. Arnaout, *Crystal structure of the extracellular segment of integrin alpha Vbeta3.* Science, 2001. **294**(5541): p. 339-45.
16. Zhang, F., ***The regulation of conformation and binding kinetics of integrin alphaLbeta2***, in *Biomedical Department*. 2007, Georgia Institute of Technology: Atlanta.
17. Dustin, M., *Induction by IL 1 and interferon-gamma: tissue distribution, biochemistry, and function of a natural adherence molecule (ICAM-1).* The Journal of Immunology, 1986. **137**(1): p. 245-254.
18. Alon, R. and M. Dustin, *Force as a Facilitator of Integrin Conformational Changes during Leukocyte Arrest on Blood Vessels and Antigen-Presenting Cells.* Immunity, 2007. **26**(1): p. 17-27.
19. Shimaoka, M., A. Salas, W. Yang, G. Weitz-Schmidt, and T.A. Springer, *Small molecule integrin antagonists that bind to the beta2 subunit I-like domain and activate signals in one direction and block them in the other.* Immunity, 2003. **19**(3): p. 391-402.
20. Giancotti, F. and E. Ruoslahti, *Integrin Signaling.* Science, 1999. **285**(5430): p. 1028.
21. Kim, M., C.V. Carman, and T.A. Springer, *Bidirectional transmembrane signaling by cytoplasmic domain separation in integrins.* Science, 2003. **301**(5640): p. 1720-5.
22. Lee, J.O., P. Rieu, M.A. Arnaout, and R. Liddington, *Crystal structure of the A domain from the alpha subunit of integrin CR3 (CD11b/CD18).* Cell, 1995. **80**(4): p. 631-8.
23. Shimaoka, M., T. Xiao, J.H. Liu, Y. Yang, Y. Dong, C.D. Jun, A. McCormack, R. Zhang, A. Joachimiak, J. Takagi, J.H. Wang, and T.A. Springer, *Structures of the alpha L I domain and its complex with ICAM-1 reveal a shape-shifting pathway for integrin regulation.* Cell, 2003. **112**(1): p. 99-111.
24. Shimaoka, M., J. Takagi, and T.A. Springer, *Conformational regulation of integrin structure and function.* Annu Rev Biophys Biomol Struct, 2002. **31**: p. 485-516.
25. Emsley, J., C.G. Knight, R.W. Farndale, M.J. Barnes, and R.C. Liddington, *Structural basis of collagen recognition by integrin alpha2beta1*. Cell, 2000. **101**(1): p. 47-56.
26. Lee, J.O., L.A. Bankston, M.A. Arnaout, and R.C. Liddington, *Two conformations of the integrin A-domain (I-domain): a pathway for activation?* Structure, 1995. **3**(12): p. 1333-40.
27. Shimaoka, M., C. Lu, R.T. Palframan, U.H. von Andrian, A. McCormack, J. Takagi, and T.A. Springer, *Reversibly locking a protein fold in an active conformation with a disulfide bond: integrin alphaL I domains with high affinity*

and antagonist activity in vivo. Proc Natl Acad Sci U S A, 2001. **98**(11): p. 6009-14.

28. Lu, C., M. Shimaoka, M. Ferzly, C. Oxvig, J. Takagi, and T.A. Springer, *An isolated, surface-expressed I domain of the integrin αLβ2 is sufficient for strong adhesive function when locked in the open conformation with a disulfide bon.* PNAS, 2001. **98**(5): p. 2387-2392.
29. Carman, C.V. and T.A. Springer, *Integrin avidity regulation: are changes in affinity and conformation underemphasized?* Curr Opin Cell Biol, 2003. **15**(5): p. 547-56.
30. Lu, C., M. Shimaoka, M. Ferzly, C. Oxvig, J. Takagi, and T.A. Springer, *An isolated, surface-expressed I domain of the integrin alphaLbeta2 is sufficient for strong adhesive function when locked in the open conformation with a disulfide bond.* Proc Natl Acad Sci U S A, 2001. **98**(5): p. 2387-92.
31. Lu, C., M. Shimaoka, Q. Zang, J. Takagi, and T.A. Springer, *Locking in alternate conformations of the integrin alphaLbeta2 I domain with disulfide bonds reveals functional relationships among integrin domains.* Proc Natl Acad Sci U S A, 2001. **98**(5): p. 2393-8.
32. Astrof, N., A. Salas, M. Shimaoka, J. Chen, and T. Springer, *Importance of Force Linkage in Mechanochemistry of Adhesion Receptors.* Biochemistry, 2006. **45**(50): p. 15020.
33. Arnaout, M.A., B. Mahalingam, and J.P. Xiong, *Integrin Structure, Allostery, And Bidirectional Signaling.* Annu Rev Cell Dev Biol, 2005. **21**: p. 381-410.
34. Xiong, J.P., T. Stehle, R. Zhang, A. Joachimiak, M. Frech, S.L. Goodman, and M.A. Arnaout, *Crystal structure of the extracellular segment of integrin alpha Vbeta3 in complex with an Arg-Gly-Asp ligand.* Science, 2002. **296**(5565): p. 151-5.
35. Takagi, J. and T.A. Springer, *Integrin activation and structural rearrangement.* Immunol Rev, 2002. **186**: p. 141-63.
36. Adair, B.D., J.P. Xiong, C. Maddock, S.L. Goodman, M.A. Arnaout, and M. Yeager, *Three-dimensional EM structure of the ectodomain of integrin {alpha}V{beta}3 in a complex with fibronectin.* J Cell Biol, 2005. **168**(7): p. 1109-18.
37. Beglova, N., S.C. Blacklow, J. Takagi, and T.A. Springer, *Cysteine-rich module structure reveals a fulcrum for integrin rearrangement upon activation.* Nat Struct Biol, 2002. **9**(4): p. 282-7.
38. Chigaev, A., T. Buranda, D.C. Dwyer, E.R. Prossnitz, and L.A. Sklar, *FRET detection of cellular alpha4-integrin conformational activation.* Biophys J, 2003. **85**(6): p. 3951-62.
39. Takagi, J., B.M. Petre, T. Walz, and T.A. Springer, *Global conformational rearrangements in integrin extracellular domains in outside-in and inside-out*

signaling. Cell, 2002. **110**(5): p. 599-11.

40. Larson, R.S., T. Davis, C. Bologa, G. Semenuk, S. Vijayan, Y. Li, T. Oprea, A. Chigaev, T. Buranda, C.R. Wagner, and L.A. Sklar, *Dissociation of I domain and global conformational changes in LFA-1: refinement of small molecule-I domain structure-activity relationships.* Biochemistry, 2005. **44**(11): p. 4322-31.
41. Woolf, E., I. Grigorova, A. Sagiv, V. Grabovsky, S. Feigelson, Z. Shulman, T. Hartmann, M. Sixt, J. Cyster, and R. Alon, *Lymph node chemokines promote sustained T lymphocyte motility without triggering stable integrin adhesiveness in the absence of shear forces.* Nature Immunology, 2007. **8**: p. 1076-1085.
42. Nishida, N., C. Xie, M. Shimaoka, Y. Cheng, T. Walz, and T. Springer, *Activation of Leukocyte ? Integrins by Conversion from Bent to Extended Conformations.* Immunity, 2006. **25**(4): p. 583-594.
43. Bell, G.I., *Models for the specific adhesion of cells to cells.* Science, 1978. **200**: p. 618-627.
44. Dembo, M., Tourney, D.C., Saxman, K., Hammer, D., *The reaction-limited kinetics of membrane-to-surface adhesion and detachment.* Pro.R.Sooc.Lond.B, 1988. **203**: p. 55-83.
45. Evans, E., *Probing the relation between force-lifetime-and chemistry in single molecular bonds.* Annu. Rev. Biophys. Biomol. Struct., 2001. **30**: p. 105-128.
46. Merkel, R., P. Nassoy, A. Leung, K. Ritchie, and E. Evans, *Energy landscapes of receptor-ligand bonds explored with dynamic force spectroscopy.* Nature, 1999. **397**(6714): p. 50-53.
47. Marshall, B.T., M. Long, J.W. Piper, T. Yago, R.P. McEver, and C. Zhu, *Direct observation of catch bonds involving cell-adhesion molecules.* Nature, 2003. **423**(6936): p. 190-3.
48. Sarangapani, K.K., T. Yago, A.G. Klopocki, M.B. Lawrence, C.B. Fieger, S.D. Rosen, R.P. McEver, and C. Zhu, *Low force decelerates L-selectin dissociation from P-selectin glycoprotein ligand-1 and endoglycan.* J Biol Chem, 2004. **279**(3): p. 2291-8.
49. Yago, T., J. Lou, T. Wu, J. Yang, J.J. Miner, L. Coburn, J.A. Lopez, M.A. Cruz, J.F. Dong, L.V. McIntire, R.P. McEver, and C. Zhu, *Platelet glycoprotein Ibα forms catch bonds with human WT vWF but not with type 2B von Willebrand disease vWF.* J Clin Invest, 2008. **118**(9): p. 3195-207.
50. Guo, B. and W.H. Guilford, *Mechanics of actomyosin bonds in different nucleotide states are tuned to muscle contraction.* Proc Natl Acad Sci USA, 2006. **103**(26): p. 9844-9849.
51. Yakovenko, O., S. Sharma, M. Forero, V. Tchesnokova, P. Aprikian, B. Kidd, A. Mach, V. Vogel, E. Sokurenko, and W.-E. Thomas, *FimH forms catch bonds that are enhanced by mechanical force due to allosteric regulation.* J Biol Chem, 2008. **283**(17): p. 11596-11605.

52. Lou, J. and C. Zhu, *A structure-based sliding-rebinding mechanism for catch bonds.* Biophys J, 2006.
53. Lou, J., T. Yago, A.G. Klopocki, P. Mehta, W. Chen, V.I. Zarnitsyna, N.V. Bovin, C. Zhu, and R.P. McEver, *Flow-enhanced adhesion regulated by a selectin interdomain hinge.* J Cell Biol, 2006. **174**(7): p. 1107-17.
54. Yakovenko, O., S. Sharma, M. Forero, V. Tchesnokova, P. Aprikian, B. Kidd, A. Mach, V. Vogel, E. Sokurenko, and W. Thomas, *FimH Forms Catch Bonds That Are Enhanced by Mechanical Force Due to Allosteric Regulation.* Journal of Biological Chemistry, 2008. **283**(17): p. 11596.
55. Evans, E., A. Leung, V. Heinrich, and C. Zhu, *Mechanical switching and coupling between two dissociation pathways in a P-selectin adhesion bond.* Proc. Natl. Acad. Sci. USA, 2004. **101**(31): p. 11281-6.
56. Chesla, S.E., P. Selvaraj, and C. Zhu, *Measuring two-dimensional receptor-ligand binding kinetics by micropipette.* Biophys. J, 1998. **75**(3): p. 1553-72.
57. Yago, T., V.I. Zarnitsyna, A.G. Klopocki, R.P. McEver, and C. Zhu, *Transport Governs Flow-Enhanced Cell Tethering through L-Selectin at Threshold Shear.* Biophys. J, 2007. **92**(1): p. 330-42.
58. Pierres, A., A.M. Benoliel, and P. Bongrand, *Use of a laminar flow chamber to study the rate of bond formation and dissociation between surface-bound adhesion molecules: effect of applied force and distance between surfaces.* Faraday Discuss, 1998(111): p. 321-30; discussion 331-43.
59. Binning, G., C. Quate, and C. Gerber, *Atomic force microscope.* Phys. Rev. Lett, 1986. **56**(9): p. 930-933.
60. Evans, E., V. Heinrich, A. Leung, and K. Kinoshita, *Nano- to microscale dynamics of P-selectin detachment from leukocyte interfaces. I. Membrane separation from the cytoskeleton.* Biophys. J., 2005. **88**(3): p. 2288-98.
61. Evans, E., K. Ritchie, and R. Merkel, *Sensitive force technique to probe molecular adhesion and structural linkages at biological interfaces.* Biophys J, 1995. **68**(6): p. 2580-7.
62. Evans, E., K. Ritchie, and R. Merkel, *Sensitive force technique to probe molecular adhesion and structural linkages at biological interfaces.* Biophysical Journal, 1995. **68**(6): p. 2580-2587.
63. Ashkin, A., *Optical trapping and manipulation of neutral particles using lasers.* 1997, National Acad Sciences. p. 4853-4860.
64. Ashkin, A., *Forces of a single-beam gradient laser trap on a dielectric sphere in the ray optics regime.* Biophysical Journal, 1992. **61**(2): p. 569.
65. Evans, E. and K. Ritchie, *Dynamic strength of molecular adhesion bonds.* Biophys J, 1997. **72**(4): p. 1541-55.
66. Evans, E., *Looking inside molecular bonds at biological interfaces with dynamic force spectroscopy.* Biophys Chem, 1999. **82**(2-3): p. 83-97.
67. Evans, E., *Probing the Relation Between Force-Lifetime-and Chemistry in Single*

Molecular Bonds. Ann. Rev. Biophys. & Biomol. Structure, 2001. **30**: p. 105-128.

68. Tees, D.F., R.E. Waugh, and D.A. Hammer, *A microcantilever device to assess the effect of force on the lifetime of selectin-carbohydrate bonds.* Biophys J, 2001. **80**(2): p. 668-82.
69. Chen, S. and T.A. Springer, *An automatic braking system that stabilizes leukocyte rolling by an increase in selectin bond number with shear.* J Cell Biol, 1999. **144**(1): p. 185-200.
70. Alon, R., D.A. Hammer, and T.A. Springer, *Lifetime of the P-selectin-carbohydrate bond and its response to tensile force in hydrodynamic flow.* Nature, 1995. **374**(6522): p. 539-42.
71. Shimaoka, M., C. Lu, R. Palframan, U. von Andrian, A. McCormack, J. Takagi, and T. Springer, *Reversibly locking a protein fold in an active conformation with a disulfide bond: Integrin alpha LI domains with high affinity and antagonist activity in vivo.* Proceedings of the National Academy of Sciences, 2001. **98**(11): p. 6009.
72. Schneider, U., H. Schwenk, and G. Bornkamm, *Characterization of EBV-genome negative" null" and" T" cell lines derived from children with acute lymphoblastic leukemia and leukemic transformed non-Hodgkin lymphoma.* Int J Cancer, 1977. **19**(5): p. 621-6.
73. Lou, J., T. Yago, A. Klopocki, P. Mehta, W. Chen, V. Zarnitsyna, N. Bovin, C. Zhu, and R. McEver, *Flow-enhanced adhesion regulated by a selectin interdomain hinge.* The J. of Cell Bio., 2006. **174**(7): p. 1107.
74. Patel, K., *Comparison of tethering and rolling of eosinophils and neutrophils through selectins and P-selectin glycoprotein ligand-1.* The Journal of Immunology, 1997. **159**(9): p. 4555-4565.
75. Moore, K., *P-selectin glycoprotein ligand-1 mediates rolling of human neutrophils on P-selectin.* The J. of Cell Bio., 1995. **128**(4): p. 661-671.
76. Kishimoto, T., M. Jutila, and E. Butcher, *Identification of a human peripheral lymph node homing receptor: a rapidly down-regulated adhesion molecule.* Proc. Natl. Acad. Sci. USA, 1990. **87**(6): p. 2244-2248.
77. Petruzzelli, L., *Activation of lymphocyte function-associated molecule-1 (CD11a/CD18) and Mac-1 (CD11b/CD18) mimicked by an antibody directed against CD18.* The Journal of Immunology, 1995. **155**(2): p. 854-866.
78. Robinson, M., *Antibody against the Leu-CAM beta-chain (CD18) promotes both LFA-1-and CR3-dependent adhesion events.* The Journal of Immunology, 1992. **148**(4): p. 1080-1085.
79. Wong, W. and K. Halvorsen, *The effect of integration time on fluctuation measurements: calibrating an optical trap in the presence of motion blur.* Optics Express, 2006. **14**(25): p. 12517-12531.
80. Dustin, M.L., S.K. Bromley, M.M. Davis, and C. Zhu, *Identification of self through two-dimensional chemistry and synapses.* Annu. Rev. Cell. Dev. Biol.,

2001. **17**: p. 133-57.
81. Pierres, A., H. Feracci, V. Delmas, A.M. Benoliel, J.P. Thiery, and P. Bongrand, *Experimental study of the interaction range and association rate of surface-attached cadherin 11*. Proc. Natl. Acad. Sci. USA, 1998. **95**(16): p. 9256-61.
82. Chesla, S.E., P. Selvaraj, and C. Zhu, *Measuring two-dimensional receptor-ligand binding kinetics by micropipette*. Biophys J, 1998. **75**(3): p. 1553-1572.
83. McEver, R.P., *Selectins: lectins that initiate cell adhesion under flow.* Curr. Opin. Cell. Biol., 2002. **14**(5): p. 581-6.
84. Marshall, B.T., K.K. Sarangapani, J. Wu, M.B. Lawrence, R.P. McEver, and C. Zhu, *Measuring molecular elasticity by atomic force microscope cantilever fluctuations.* Biophys. J, 2006. **90**(2): p. 681-92.
85. Wu, J., Y. Fang, D. Yang, and C. Zhu, *Thermo-mechanical responses of a surface-coupled AFM cantilever.* J. Biomech. Eng, 2005. **127**(7): p. 1208-15.
86. Mehta, P., R.D. Cummings, and R.P. McEver, *Affinity and kinetic analysis of P-selectin binding to P-selectin glycoprotein ligand-1*. J Biol Chem, 1998. **273**: p. 32506-32513.
87. Nicholson, M.W., A.N. Barclay, M.S. Singer, S.D. Rosen, and P.A. Van der Merwe, *Affinity and kinetic analysis of L-selectin (CD62L) binding to glycosylation-dependent cell-adhesion molecule-1*. J Biol Chem, 1998. **273**: p. 763-770.
88. Kulin, S., R. Kishore, J.B. Hubbard, and K. Helmerson, *Real-time measurement of spontaneous antigen-antibody dissociation.* Biophys J, 2002. **83**(4): p. 1965-73.
89. Vestweber, D. and J.E. Blanks, *Mechanisms that regulate the function of the selectins and their ligands.* Physiol Rev, 1999. **79**(1): p. 181-213.
90. McEver, R.P., *Selectins: lectins that initiate cell adhesion under flow.* Curr Opin Cell Biol, 2002. **14**(5): p. 581-586.
91. Finger, E.B., K.D. Puri, R. Alon, M.B. Lawrence, U.H. Von Andrian, and T.A. Springer, *Adhesion through L-selectin requires a threshold hydrodynamic shear.* Nature, 1996. **379**: p. 266-269.
92. Alon, R., S.Q. Chen, K.D. Puri, E.B. Finger, and T.A. Springer, *The kinetics of L-selectin tethers and the mechanics of selectin-mediated rolling.* J Cell Biol, 1997. **138**: p. 1169-1180.
93. Yago, T., V. Zarnitsyna, A. Klopocki, R. McEver, and C. Zhu, *Transport Governs Flow-Enhanced Cell Tethering through L-Selectin at Threshold Shear.* Biophysical Journal, 2007. **92**(1): p. 330.
94. Bell, G.I., *Models for the specific adhesion of cells to cells: A theoretical framework for adhesion mediated by reversible bonds between cell surface molecules.* Science, 1978. **200**: p. 618-627.
95. Marshall, B.T., M. Long, J.W. Piper, T. Yago, R.P. McEver, and C. Zhu, *Direct observation of catch bonds involving cell-adhesion molecules.* Nature, 2003.

423(6936): p. 190-193.
96. Sarangapani, K.K., T. Yago, A.G. Klopocki, M.B. Lawrence, C.B. Fieger, S.D. Rosen, R.P. McEver, and C. Zhu, *Low force decelerates L-selectin dissociation from P-selectin glycoprotein ligand-1 and endoglycan.* J Biol Chem, 2004. **279**: p. 2291-2298.
97. Yago, T., J. Wu, C.D. Wey, A.G. Klopocki, C. Zhu, and R.P. McEver, *Catch bonds govern adhesion through L-selectin at threshold shear.* J Cell Biol, 2004. **166**: p. 913-923.
98. Zhu, C., J. Lou, and R.P. McEver, *Catch bonds: physical models, structural bases, biological function and rheological relevance.* Biorheology, 2005. **42**(6): p. 443-462.
99. Marshall, B.T., K.K. Sarangapani, J. Lou, R.P. McEver, and C. Zhu, *Force history dependence of receptor-ligand dissociation.* Biophys J, 2005. **88**(2): p. 1458-66.
100. Mehta, P., R.D. Cummings, and R.P. McEver, *Affinity and kinetic analysis of P-selectin binding to P-selectin glycoprotein ligand-1*. J Biol Chem, 1998. **273**(49): p. 32506-13.
101. Nicholson, M., A. Barclay, M. Singer, S. Rosen, and P. van der Merwe, *Affinity and Kinetic Analysis of L-selectin (CD62L) Binding to Glycosylation-dependent Cell-adhesion Molecule-1*. Journal of Biological Chemistry, 1998. **273**(2): p. 763-770.
102. Astrof, N.S., A. Salas, M. Shimaoka, J. Chen, and T.A. Springer, *Importance of force linkage in mechanochemistry of adhesion receptors.* Biochemistry, 2006. **45**(50): p. 15020-15028.
103. Woolf, E., I. Grigorova, A. Sagiv, V. Grabovsky, S.-W. Feigelson, Z. Shulman, T. Hartmann, M. Sixt, J.-G. Cyster, and R. Alon, *Lymph node chemokines promote sustained T lymphocyte motility without triggering stable integrin adhesiveness in the absence of shear forces.* Nat Immunol, 2007. **8**(10): p. 1076-1085.
104. Jin, M., l. Andricioaei, and T.A. Springer, *Conversion between three conformational states of integrin I domains with a C-terminal pull spring studied with molecular dynamics.* Structure, 2004. **12**(12): p. 2137-2147.
105. Puklin-Faucher, E., M. Gao, K. Schulten, and V. Vogel, *How the headpiece hinge angle is opened: new insights into the dynamics of integrin activation.* J Cell Biol, 2006. **175**(2): p. 349-360.
106. Sarangapani, K.K., T. Yago, A.G. Klopocki, M.B. Lawrence, C.B. Fieger, S.D. Rosen, R.P. McEver, and C. Zhu, *Low force decelerates L-selectin dissociation from P-selectin glycoprotein ligand-1 and endoglycan.* J Biol Chem, 2004. **279**(3): p. 2291-2298.
107. Li, F., S.D. Redick, H.P. Erickson, and V.T. Moy, *Force measurements of the α5β1 integrin-fibronectin interaction.* Biophys J, 2003. **84**(2): p. 1252-1262.
108. Zhang, X., E. Wojcikiewicz, and V.T. Moy, *Force spectroscopy of the leukocyte*

function-associated antigen-1/Intercellular adhesion molecule-1 interaction. Biophys J, 2002. **83**(4): p. 2270-2279.

109. Zhang, X., S.E. Craig, H. Kirby, M.J. Humphries, and V.T. Moy, *Molecular basis for the dynamic strength of the integrin $\alpha_4\beta_1$/VCAM-1 interaction.* Biophys J, 2004. **87**(5): p. 3470-3478.
110. Vitte, J., A. Pierres, A.-M. Benoliel, and P. Bongrand, *Direct quantification of the modulation of interaction between cell- or surface-bound LFA-1 and ICAM-1.* J Leukocyte Biol, 2004. **76**(3): p. 594-602.
111. Lu, C., M. Ferzly, J. Takagi, and T. Springer, *Epitope Mapping of Antibodies to the C-Terminal Region of the Integrin ? Subunit Reveals Regions that Become Exposed Upon Receptor Activation 1.* The Journal of Immunology, 2001. **166**(9): p. 5629-5637.
112. Lou, J. and C. Zhu, *A structure-based sliding-rebinding mechanism for catch bonds.* Biophys J, 2007. **92**(5): p. 1471-85.
113. Salas, A., M. Shimaoka, A. Kogan, C. Harwood, U. von Andrian, and T. Springer, *Rolling Adhesion through an Extended Conformation of Integrin aL? and Relation to a I and ?I-like Domain Interaction.* Immunity, 2004. **20**(4): p. 393-406.
114. Xiao, T., J. Takagi, B.S. Coller, J.H. Wang, and T.A. Springer, *Structural basis for allostery in integrins and binding to fibrinogen-mimetic therapeutics.* Nature, 2004. **432**(7013): p. 59-67.
115. Takagi, J., H.P. Erickson, and T.A. Springer, *C-terminal opening mimics 'inside-out' activation of integrin alpha5beta1.* Nat Struct Biol, 2001. **8**(5): p. 412-6.
116. Nermut, M., N. Green, P. Eason, S. Yamada, and K. Yamada, *Electron microscopy and structural model of human fibronectin receptor.* The EMBO Journal, 1988. **7**(13): p. 4093.
117. DU, X., M. GU, J. WEISEL, C. NAGASWAMI, J. BENNETT, R. BOWDITCH, and M. GINSBERG, *Long range propagation of conformation changes in integrin a?IIb?? 3 ?* The Journal of biological chemistry(Print), 1993. **268**(31): p. 23087-23092.
118. Chigaev, A., T. Buranda, D. Dwyer, E. Prossnitz, and L. Sklar, *FRET Detection of Cellular a 4-Integrin Conformational Activation.* Biophysical Journal, 2003. **85**(6): p. 3951-3962.
119. Chigaev, A., G. Zwartz, T. Buranda, B. Edwards, E. Prossnitz, and L. Sklar, *Conformational Regulation of {alpha} 4 {beta} 1-Integrin Affinity by Reducing Agents:" INSIDE-OUT" SIGNALING IS INDEPENDENT OF AND ADDITIVE TO REDUCTION-REGULATED INTEGRIN ACTIVATION.* Journal of Biological Chemistry, 2004. **279**(31): p. 32435.
120. Shao, J., H. Ting-Beall, and R. Hochmuth, *Static and dynamic lengths of*

neutrophil microvilli. 1998, National Acad Sciences. p. 6797-6802.

121. Lu, C., M. Shimaoka, A. Salas, and T. Springer, *The Binding Sites for Competitive Antagonistic, Allosteric Antagonistic, and Agonistic Antibodies to the I Domain of Integrin LFA-1.* JOURNAL OF IMMUNOLOGY-BETHESDA-, 2004. **173**(6): p. 3972-3978.
122. Marshall, B.T., K.K. Sarangapani, J. Wu, M.B. Lawrence, R.P. McEver, and C. Zhu, *Measuring Molecular Elasticity by Atomic Force Microscope Cantilever Fluctuations.* Biophys J, 2005.
123. Xiong, J.P., T. Stehle, S.L. Goodman, and M.A. Arnaout, *New insights into the structural basis of integrin activation.* Blood, 2003. **102**(4): p. 1155-9.
124. Shamri, R., V. Grabovsky, J. Gauguet, S. Feigelson, E. Manevich, W. Kolanus, M. Robinson, D. Staunton, U. von Andrian, and R. Alon, *Lymphocyte arrest requires instantaneous induction of an extended LFA-1 conformation mediated by endothelium-bound chemokines.* Nature Immunology, 2005. **6**: p. 497-506.
125. Carreno, R., D. Li, M. Sen, I. Nira, T. Yamakawa, Q. Ma, and G. Legge, *A Mechanism for Antibody-mediated Outside-in Activation of LFA-1.* Journal of Biological Chemistry, 2008. **283**(16): p. 10642.
126. Davis, M., M. Krogsgaard, M. Huse, J. Huppa, B. Lillemeier, and Q. Li, *T Cells as a Self-Referential, Sensory Organ.* ANNUAL REVIEW OF IMMUNOLOGY, 2007. **25**: p. 681.
127. Giannone, G. and M. Sheetz, *Substrate rigidity and force define form through tyrosine phosphatase and kinase pathways.* Trends in Cell Biology, 2006. **16**(4): p. 213-223.
128. WANG, Y., E. BOTVINICK, Y. ZHAO, M. BERNS, S. USAML, R. TSLEN, and S. CHLEN, *Visualizing the mechanical activation of Src.* Nature(London), 2005. **434**(7036): p. 1040-1045.
129. Na, S., O. Collin, F. Chowdhury, B. Tay, M. Ouyang, Y. Wang, and N. Wang, *Rapid signal transduction in living cells is a unique feature of mechanotransduction.* Proceedings of the National Academy of Sciences, 2008. **105**(18): p. 6626.
130. Heinrich, V., W. Wong, K. Halvorsen, and E. Evans, *Imaging Biomolecular Interactions by Fast Three-Dimensional Tracking of Laser-Confined Carrier Particles.* Langmuir, 2008. **24**(4): p. 1194-1203.